# Multiscale modeling of carbon nanotube materials with distinct element method

A Dissertation

SUBMITTED TO THE FACULTY OF

UNIVERSITY OF MINNESOTA

BY

Igor Aleksandrovich Ostanin

IN PARTIAL FULFILLMENT OF THE REQUIREMENTS

FOR THE DEGREE OF

DOCTOR OF PHILOSOPHY

Advisers: Roberto Ballarini, Traian Dumitrica

May 2014

# Acknowledgements

I would like to thank my academic advisers - Roberto Ballarini and Traian Dumitrica - for their help and motivating comments and questions. I want to thank all my teachers, professors and instructors who guided me through the years of my academic career, in particular, Vladimir Synakh, Vladislav Dubrovsky, Aleksey Tribendis, Ivan Koop, Dmitry Berkaev, Sofia Mogilevskaya, Joseph Labuz, Henryk Stolarsky, Roger Fosdick and Ellad Tadmor. I thank my parents and family for their support and encouragement.

I want to express my gratitude to Itasca Consulting Group, who provided me the financial and technical support, and the access to their commercial codes and software development tools, without which this work could not come to fruition. Personally, I would like to thank William Pettitt, David Potyondy, David Russel, Matthew Purvance and Sacha Emam.

I would like to acknowledge Erik Hobbie, Evgeniya Dontsova, Ilia Nikiforov, Tyler Anderson, Ludong Sun, Cristian Gaidau and Yuezhou Wang for their efforts that facilitated some developments presented in this work.

I express deep gratitude to the National Science Foundation, the University of Minnesota Doctoral Dissertation Fellowship program, and the James L. Record Chair for funding me during my PhD studies.

# Abstract

Mesoscale simulation techniques are becoming increasingly important due to the interest in complex mechanical problems involving nanoscale structures and materials. This work is devoted to the development of a novel mesoscopic modeling technique based on an extension of the distinct element method and its application to the problem of mechanical modeling of carbon nanotube (CNT) materials. Starting from an atomistic description, the important interactions between segments of the tubes are encapsulated into two types of contact models. The nanomechanics of intratube bonds is characterized by the parallel bond contact model. Intertube interactions are accounted for by an anisotropic vdW contact model. Energy dissipation is formulated in a top-down manner, based on the macroscopic mechanical properties of carbon nanotube materials. The developed model is applied to the analysis of various mesoscopic structures and materials - self-folded nanotube configurations, nanotube bundles and ropes, nanotube papers and films. The results of mesoscopic simulations not only are in good agreement with experimental observations, but they also provide interesting insights on the roles of effects of morphology, vdW adhesion and registry, cross-linking and energy dissipation on the nanomechanics of carbon nanotube based materials.

# Table of Contents

# List of Tables

# List of Figures

# Nomenclature

The following notations are used globally throughout the text.

| | |
|---|---|
| $\zeta$ | CNT persistence length |
| $R_{CNT}$ | Radius of a CNT segment |
| $T$ | Length of a CNT segment |
| $t_o$ | Equilibrium vdW spacing (assumed wall thickness of a CNT) |
| $r_o$ | Equilibrium distance between axes of parallel CNTs |
| $E_{CNT}, G_{CNT}$ | Young's modulus and shear modulus of a CNT |
| $\xi$ | vdW adhesion energy per unit length of two parallel CNTs (equilibrium separation) |
| $EI$ | Bending stiffness of a CNT |
| $\chi$ | Local damping coefficient |
| $\psi$ | Viscous damping coefficient |
| $E, G$ | Elastic moduli of homogenized CNT material |
| $\sigma_{uts}, \varepsilon_c$ | Uniaxial tensile strength of a bundle and corresponding strain |
| $M$ | Length factor of the bundle |
| $N$ | Thickness factor of the bundle |
| $\alpha_c$ | Relative strength of a cross-link |
| $\beta_c$ | Relative stiffness of a cross-link |
| $\gamma_c$ | Relative cross-link density |

# Chapter 1

# Introduction

## 1.1 Background

Carbon nanotubes [1] (CNTs), one-dimensional needlelike structures (macromolecules), are allotropes of $sp^2$ carbon. They can be viewed as single-atom-thick layers of graphite, seamlessly folded into cylinders. Periodicity of the atomic lattice implies certain limitations on possible ways of such folding - a circumference vector of a single wall CNT is required to be a linear combination of eigenvectors of the CNT lattice with integer coefficients (Fig. 1(A)).

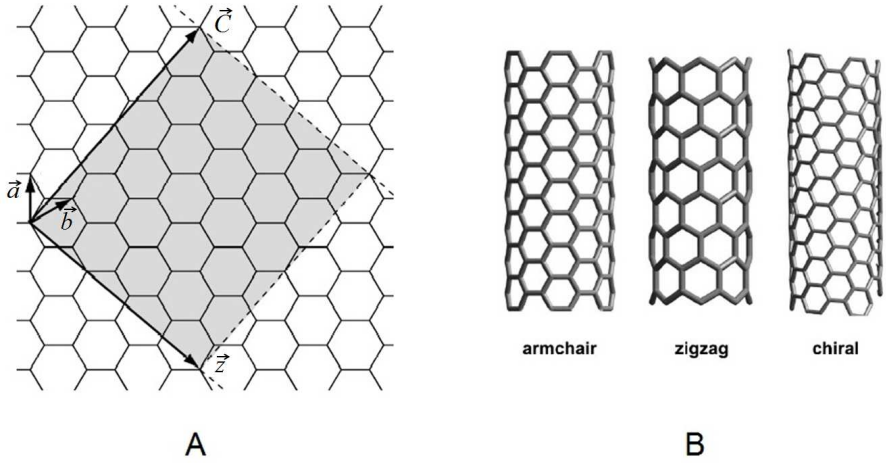


Figure 1: (A) Unfolded (4,2) CNT. $\vec{a}$ and $\vec{b}$ are lattice eigenvectors, $\vec{C}$ is the circumference vector of the tube, $\vec{z}$ defines axial direction of a CNT. Sides of hexagons denote covalent bonds between *C* atoms. (B) Different kinds of CNTs.

These coefficients define the type of a single wall CNT (SWCNT), *e.g.* $(n, m)$ CNT. Two particular subclasses of SWCNTs are usually distinguished - "armchair" $(n, n)$ CNTs and "zigzag" $(n, 0)$ CNTs (Fig. 1(B)). In a general case CNT is referred to as "chiral". Along with SWCNTs there also exist multi-walled CNTs (MWCNTs) - coaxial structures of multiple SWCNTs folded one into another. CNTs are produced by condensation of carbon atoms on nanoparticles of a catalyst metal at very low pressure, high carbon concentration and temperature. Numerous technologies have been developed to produce high yields of CNTs – arc discharge, laser ablation, chemical vapor deposition (see review papers [2-4] and references in there).

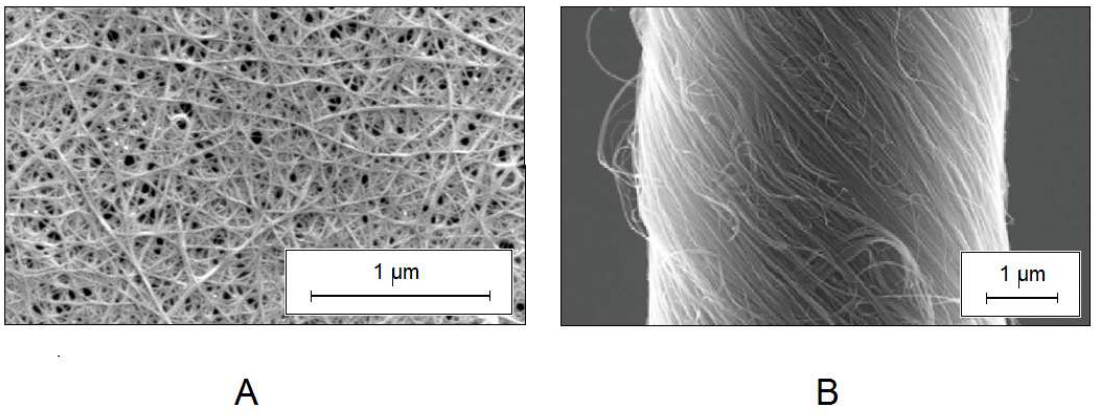


Figure 2: Scanning electron microscopy pictures of CNT materials. (A) CNT paper. (B) CNT rope (image from [6]).

CNTs possess exceptional physical and mechanical properties. Very high tensile strength of individual CNTs (~100 GPa) makes them extremely attractive as reinforcement fibers in composites. The promise offered by CNTs in this particular area

was not, however, fully realized due to relatively weak cohesion of CNTs with metallic or ceramic matrices [5].

The focus of the present work is pristine (pure) CNT materials. Different synthesis and processing procedures allow the production of materials and structures with different organizations: CNT foams, coils, forests, films, fibers [6-16]. The most common and easiest to produce CNT-based material is the CNT film, also referred to as buckypaper (Fig. 2 (A), [9, 10]). Mechanical properties of buckypapers vary depending on the particular type of CNTs, and in particular their length and the morphology of the film on the microscale. Another important class of CNT materials is CNT ropes (Fig. 2 (B)) - highly aligned and closely packed CNTs, forming long twisted fibers [12-16].

Different technical applications utilize different properties of CNT materials - combination of strength and lightness [17], viscoelastic and damping properties [18, 19] and exceptional thermal conductivity [20]. Combination of mechanical durability, transparency and electrical conductivity (CNTs exhibit metallic or semiconducting electrical properties, depending on their type) make thin CNT films ideal for coating applications in stretchable electronic devices [9].

The mechanics of individual CNTs and CNT materials has and continues to be extensively studied both experimentally and theoretically. The experimental research is mostly focused on the mechanics of macroscopic, homogenized CNT materials. Among the most important experimental studies are associated with self-organization of CNTs in complex systems of bundles [9, 10], temperature-independent viscoelasticity of

supported CNT films, buckypapers, and CNT-based composites [18, 19], gradual rate-dependent plastic failure of supported thin films [9], viscous creep of CNT films and aligned CNT massives [21, 22], auxetic behavior of buckypapers and CNT foams [23, 24]. Due to limited possibilities of direct experimental research, CNT mechanics on the nanoscale has been extensively studied using theoretical apparatus of quantum and classical mechanics, combined with modern computational methods. Quantum mechanics (QM) approaches, such as density functional theory (DFT) [25] and tight binding (TB) approximations [26] are used on the finest scale to assess the mechanics of $10^1 \div 10^2$ carbon atoms. The results of QM are used to obtain empirical potentials for interacting particles (for covalent systems these are Tersoff [27] and Stillinger-Weber [28] potentials describing bonding of atoms and Lennard-Jones [29] potential describing non-bonding long range vdW interactions). These classical potentials are used in many body dynamic simulations, where carbon atoms are described as neutral particles. Symplectic (energy conserving) algorithms, such as the velocity Verlet algorithm [30] are used to evolve the system in time. Such molecular dynamic (MD) simulations, which can be utilized to study the dynamics of $10^4 \div 10^8$ atoms, have been used successfully to study linear regimes of CNT deformation, as well as buckling of single wall CNTs (SWCNT) and rippling of multi wall CNTs (MWCNT) under bending and torsion [31-33].

Although the mechanics of both CNTs on a microscale and CNT materials on a macroscale have been studied extensively, there still exists a gap in length and time scales between the models and the reality that prevents the application of the results of QM and MD simulations directly to the interpretation of macroscopic mechanical

behavior of CNT materials. In order to fill this gap, mesoscopic models are used [34-50], that are typically based on the idea of static or adaptive reduction of the number of degrees of freedom of the dynamic system considered. Mesoscopic modeling appears to be an efficient tool in various applications, including i) dynamic behavior of single CNTs and simple CNT-based nanomechanical devices, ii) self-folding and self-assembly processes in single CNTs and their large collections, iii) Modeling the mechanical response of CNT materials.

### 1.2 The researched problem

This doctoral dissertation is concerned with the development of a computationally efficient technique of mesoscopic modeling of carbon nanotube systems, and its applications to timely problems involving the nanomechanics of CNT assemblies. The paradigm is based on the formalism of the distinct element method (DEM), and is presented in our recent works [46-50]. DEM was developed for simulating the mechanical properties and response of macroscopic geological materials and structures by representing them as large numbers of interacting rigid particles. With DEM, a CNT is represented as a chain of rigid particles interacting with each other via prescribed contact models, informed by the results obtained from simulations on the atomistic scale.

The mesoscopic model presented in this doctoral dissertation is perhaps the most robust model for simulating CNT materials. It has been successfully applied to modeling of individual isolated CNTs and their self-folded configurations; quasi - one dimensional assemblies of CNTs (CNT ropes and fibers); two-dimensional CNT structures – such as

unsupported CNT films and CNT-polymer composites. Many results discussed in the next chapters of this thesis are supported by experimental observations.

### 1.3 Current developments in the field

Mesoscopic modeling of CNTs has received lots of attention during the past decade [34-50]. Two types of mesoscopic models have gained popularity - the bead and spring (BS) model [34-39] and the mesoscopic force field (MFF) model [40-45]. Nevertheless, in spite of such developments, simulations of collective CNT behavior have not kept pace with the demand from many urgent areas of nanoscience and engineering.

The BS model was appropriated from the coarse-grained modeling of organic polymers [51-53]. As the name suggests, a CNT is represented by a collection of point masses connected by linear springs. Simulations based on BS were carried out to study the behavior of hundreds of CNTs on a timescale approaching microseconds [34].

The MFF model describes the motion of CNT in terms of the dynamics of nodal point masses, connected by flexible and stretchable cylinders, interacting via vdW contacts. The advanced features of the model are the adaptive meshing technique that allows reduction in the number of degrees of freedom, and the physically realistic approximate potential of van der Waals (vdW) dispersive interactions.

It is important to recognize that any coarse graining procedure should agree with the microscopic description in the features deemed important for the problem at hand. Nevertheless, it was observed [41] that the simulations of CNT collective behavior based on the two models don't lead to similar outcomes. For example, while the configurations

that evolved using the BS model remain randomly oriented individual CNTs or small bundles, the MFF predicts the formation of large bundles that are agreement with experimental observation. This qualitatively different behavior was attributed to the way in which the long-range vdW interaction between CNTs is handled by the two mesoscopic models. While in the BS model the intertube interaction is captured by a spherically-symmetric potential associated with pairs of beads, the same interaction is described more realistically in MFF by considering the vdW coupling of cylindrical elements of arbitrary lengths and orientations [42].

Both BS and MFF models are based on the dynamics of point masses, interacting via relatively simple potentials. In our model we have taken a major step forward, by representing CNT segments with rigid bodies. At cost of moderate decrease of computational performance, such an approach dramatically widens the area of the model's applicability. Our formalism allows incorporation of perfect potential interactions between rigid segments, which allows us to model complex intertube/intratube interactions in 3D, providing a wide avenue for possible model extensions with such complex features as nonlinear bending/twisting regimes (rippling, buckling), complex CNT failure mechanisms, forward and inverse coarse-graining [54].

Another important issue that is widely ignored in works on mesoscopic modeling of CNT materials is energy dissipation. The influence of intertube sliding dissipation was first analyzed in my work [42].

The DEM mesoscopic model enabled me to explore several important problems of CNT

mechanics at the nano- and microscales. These include self-folding of CNT with relative sliding, modeling the behavior of CNT rope under torsional load, analysis of representative element (RVE) size in CNT ropes and CNT films. Determining whether an RVE is achieved in CNT structures was investigated for the first time. On the other hand, new insights have been gained on the role of the energy structure that evolves during the mechanical response of self-assembled morphologies of CNT materials.

### 1.4 Organization of the thesis

The thesis consists of two major parts - the development and validation of the mesoscopic model, and the simulations of various CNT systems. The first part (Chapter 2) is focused on methodology of mesoscale modeling and underlying physical and mechanical theory. This includes the molecular physics responsible for the covalent bonds and van der Waals (vdW) interactions, numerical methods of integration of interacting rigid bodies, and the physical mechanisms of the energy dissipation. The second part (Chapter 3) demonstrates the usefulness of the developed model for the relevant problems for mesoscale CNT mechanics. The range of analyzed problems includes self-folding and self-assembly of CNT structures, and the mechanics of different types of CNT materials under mechanical loading. Finally, Chapter 4 summarizes the contributions presented in this work and explores possible directions of future work.

An interdisciplinary character of the project makes it problematic to present all the material using the same notation style. Therefore, although most of the notations are preserved throughout the text, some of them (usually ones used in local derivations) are

redefined in new sections. The most important definitions that are used globally are collected in the nomenclature page at the beginning of the thesis. Although most of the definitions follow usual notations accepted by the mechanics community, some are changed in order to ensure non-contradictory nomenclature.

The following convention is used for notation of mathematical objects: scalars are denoted with regular cursive - $x$, vectors are marked with an upper arrow - $\vec{x}$; vector Cartesian components are denoted as $x_i$, $i$ = 1..3 ($x$,$y$,$z$); orthogonal sets of unit vectors (bases) are denoted as $\hat{e}_i (i = 1..3)$; matrices are marked with an upper bar - $\bar{M}$; matrix components (and Cartesian components of a second order tensor) are denoted as $M_{ij}$, $i$ = 1..3 ($x$,$y$,$z$); quaternions used in section 2.4 are denoted as $< q_0, q >$.

# Chapter 2

# Model

## 2.1 Theoretical foundations of the multiscale modeling of CNTs

As stated in the Introduction, full-scale molecular dynamics is an efficient and universal modeling tool, which, however, faces computational limitations when dealing with mesoscale systems, involving ~$10^8 \div 10^{10}$ atoms. Nevertheless, the full-atomistic description may often be excessive. For example, neglecting thermal fluctuations, small deformations of crystalline regions of solid bodies can be described with solutions of corresponding boundary value problems of anisotropic elastic continuum. Similarly, in many problems of mesoscale mechanics the full-atomistic description can be replaced with a simplified (coarse-grained) structure that is capable of capturing the desired phenomena.

The central idea of coarse-graining is reduction of the number of degrees of freedom (DOF) via certain static or adaptive procedures. The reduced DOF model should exhibit the same static and dynamic response as the full-atomistic model, in addition to sufficiently equivalent energies of these models [55]. On the other hand, the energy exchange between the remaining DOFs and ones eliminated in coarse-graining process should be adequately represented.

One can distinguish hierarchical and concurrent approaches in coarse-grained modeling

[56]. The hierarchical approach is based on the idea of representation of the whole problem domain with a coarse-grained model, whose constitutive laws are informed by finer-scale MD simulations. Within such an approach a coarse-graining can be viewed as the necessary intermediate step in homogenization, *i.e.* mapping of the full-atomistic model into a homogenized continuum model. Oppositely, the concurrent multiscale approach is a common way to deal with mechanical problems involving localized failure. The idea is the representation of the system with "coarse" and "fine" model regions. "Fine" model (atomistic region) can resolve various forms of localized damage, whereas "coarse" model is used to handle elastic deformation. Again, the coarse-graining scheme should ensure correct processes of energy transfer, as well as seamless forward and inverse coarse-graining. This transition can be performed adaptively in a course of a simulation, *e.g.* based on the maximum value of local strain energy.

CNTs present an attractive object for mesoscale modeling. First of all, the tensile/shear and bending/twisting responses of CNTs are well described by simple beam theory assumptions [57]. Second, the carbon nanotubes are large enough to be considered as macroscopic bodies, *i.e.* the heat motion of CNT atoms does not lead to significant CNT oscillations. Adopting the terminology from polymer physics [58], one can define the persistence length of a CNT as

$$\zeta = \frac{EI}{k_b T} \tag{2.1}$$

Here $EI$ is the bending stiffness of a CNT, and $k_b T$ is the energy of thermal fluctuations.

The persistence length describes the molecular length at which the thermal energy becomes sufficient to induce significant bending (and self-folding) in the CNT. For $(10,10)$ CNTs with bending stiffness $EI = 2.235\ \mathrm{eV}\cdot\mu\mathrm{m}$ at temperature of 300 $K$ ($k_b T = 0.026\,eV$) $\zeta$ =86 $\mu$m. However, in all the simulations described in this work the CNT lengths are two orders of magnitude smaller than the persistence length. Thus, the mechanics of CNT materials is unaffected by thermally-induced motion and deformations.

Therefore, the problem of the mechanics of a CNT material can be considered as a problem of mechanical analysis of an assembly of elastic rods/beams. However, the mechanics of CNT materials arises not only from the properties of individual CNTs, but also from the interactions between them. The model for non-bonding adhesion between CNTs is one of the central parts of the present work. The model is discussed in section 2.6. Another important issue that poses a serious problem is quantitatively correct energy dissipation. This topic is explored in section 2.7.

**2.2 Distinct element method**

DEM, the numerical method introduced by Cundall and Strack [59-61] more than 30 years ago, was developed for simulating the mechanical properties and response of macroscopic geological materials [62] and structures by representing them as a large numbers of interacting particles. Although generalized DEM computes the dynamics of deformable polygonal-shaped particles, conventional DEM packages (*e.g.* [63]) are based on the simplified formulation describing dynamics of rigid spherical particles.

The DEM calculation cycle is shown in Fig. 3. It alternates between the dynamic laws of

particle motion, and force-displacement laws at contacts. After incrementing particles translations and rotations (and corresponding velocities and accelerations) by applying motion laws (dynamic equations and time integration schemes), the special algorithm of contact search updates the set of contacts. The forces acting on particles are then updated with regard to their mutual positions and velocities, according to prescribed contact and damping laws.

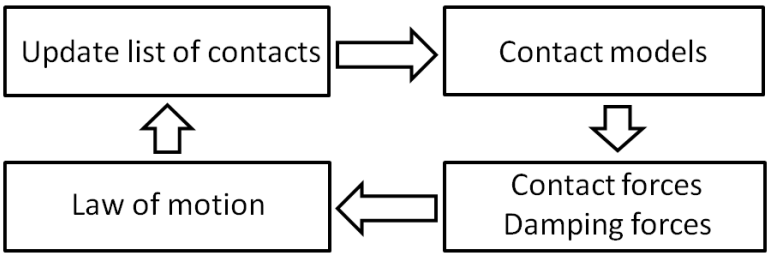


Figure 3: Calculation cycle in DEM.

There are three different ways to use DEM. First, it can be used in dynamic problems and can provide information on vibrational modes of complex systems of interacting bonded particles. Second, it can be employed in quasi-static problems, when dynamic forces are negligible compared to potential and dissipative forces, in order to study rate-dependent transitional processes in complex systems. The third possible application is finding an equilibrium state of complex systems.

The following sections elaborate the implementation of our mesoscopic model within DEM: the time integration schemes, the force-displacement laws (contact models) and the channels of energy dissipation in the model are reviewed.

### 2.3 DEM model for CNT assemblies

This section provides an overview of the key features of a coarse-graining scheme used in our mesoscopic model. Subsequent discussion is limited to $(10,10)$ CNTs, that were studied in all of my works [47-50].

Within DEM, a CNT is represented by a chain of rigid hollow cylindrical segments (distinct elements), linked with elastic parallel bonds (see section 2.5). Each segment has unit aspect ratio, *i.e.* its length $T$ is twice the radius of a CNT $R_{CNT}$ (Fig. 4). For $(10,10)$ CNTs the segment lumps approximately 220 carbon atoms. A segment of this size is considered a representative element both in terms of its mass/moment of inertia and its stiffness.

A CNT segment is characterized by mass $m$ and inertia tensor $I_{ij}$ . Cartesian components of tensor of inertia of a hollow cylindrical segment with an axis parallel to $Z$ coordinate axis are:

$$I_{11} = I_{22} = \frac{m}{12}\left(6{R_{CNT}}^2 + T^2\right), \quad I_{33} = m{R_{CNT}}^2 \quad I_{ij}^{(i\neq j)} = 0 \tag{2.2}$$

The parameterization of CNT segment geometry and inertial properties for $(10,10)$ CNTs is provided in Table 1.

Table 1. Geometry, mass and moment of inertia of a segment of (10,10) CNT.

| $R_{CNT}$ , Å | $T$ , Å | $m$ , amu | $I_{11}$, amu × Å$^2$ | $I_{22}$, amu × Å$^2$ | $I_{33}$, amu × Å$^2$ |
|---|---|---|---|---|---|
| 6.78 | 13.56 | 2,649 | 101,475 | 101,475 | 121,770 |

Each segment (with exception of the first few neighbors in the same CNT) interacts with another via long range vdW interaction (see section 2.6), if the distance between the segments centroids is smaller than a prescribed interaction cutoff radius.

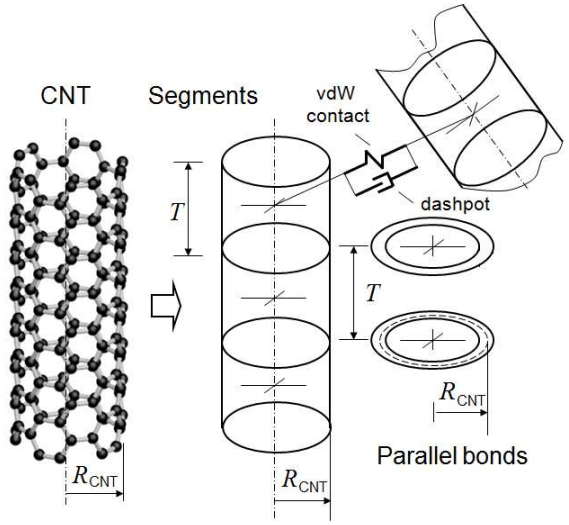


Figure 4: Coarse graining of a CNT into a chain of cylindrical segments, representing inertial properties of a CNT. Segments are linked with parallel bond interfaces, representing elastic properties of a CNT surface, arising from covalent bonds between C atoms within the CNT surface. Segments of neighboring CNTs interact via mesoscopic vdW contact model, acting in parallel with viscous forces that damp relative translational motion of CNT segments.

The DEM computes translational and rotational dynamics of interacting rigid CNT

segments. Time integration schemes employed are described in section 2.4.

There are two channels of energy dissipation in the DEM model – local damping and viscous damping, characterized by the parameters $\chi$ and $\psi$, defined in [63]. Local damping is introduced as a component of the time integration scheme with the sole goal to ensure time integration stability in otherwise undamped system. The viscous damping acts in parallel with vdW contact model and is used to represent the energy losses in CNT sliding (Fig. 4). Calibration of the dissipation is a topic of sections 2.7 and 3.2.

**2.4 Time integration schemes employed in the analysis of the dynamics of CNT segments**

As previously mentioned, one of the essential features of the model is idealization of coarse-grained segments of CNTs as rigid bodies. Such an approach allows using complex interaction models, that resolve not only normal forces between CNT segments, but shear forces and contact moments as well. Therefore, the equations of motion involve not only translational, but also rotational degrees of freedom.

The conventional DEM is based on the time evolution of spherical particles [63]. In this case the system is governed by similar equations for both translational and rotational motion:

$$\vec{F} = m\dot{\vec{v}} \quad \vec{M} = I\dot{\vec{\omega}} \tag{2.3}$$

Here $\vec{F}$ and $\vec{M}$ are external forces and moments, that are calculated from interaction potentials and mutual positions of particles, $\vec{v}$ and $\vec{\omega}$ are translational and angular

velocities of a segment, $m$ and $I$ are mass and moment of inertia of a spherical particle.

These equations can be integrated using similar time integration schemes, such as leapfrog [63] or velocity Verlet [30]. Within this scheme no information is required about the rotational position of a spherical particle, and thus it has advantages in memory usage and performance. The first implementation of the mesoscopic model [47] was based on the coarse-graining of CNT segments into spherical particles. However, such an approach has significant limitations. First, it is impossible to match both principal moments of inertia of a CNT segment. This limitation affects the dynamic properties of a model, *e.g.* free vibration frequencies of a CNT. Second, absence of information on the rotational position of a segment in space leads to impossibility of forward and inverse coarse-graining in concurrent multiscale modeling. Third, this formulation allows only relatively simple incremental models of bonding [64] and does not allow straightforward use of complex contact models with interaction depending on mutual orientation of particles.

An alternative approach that was employed in my recent works [48-50] is to compute full 3D dynamics of cylindrical segments. Here I present the description of time integration schemes used in our simulations. These are standard schemes currently employed in DEM simulations of macroscopic materials and structures, used here for the first time for simulating the CNT mesoscale mechanics.

The translational dynamics of the CNT segments of mass $m$ is described in terms of position $x_i$, translational velocity $v_i$ and acceleration $a_i$. Integration of translational

motion is based on conventional velocity Verlet scheme, involving timestep $\Delta t$.

Calculation of the new position, translational velocity and acceleration is done in a following way. First, the velocity is calculated at a half-step as

$$v_i(t+0.5\Delta t) = v_i(t) + 0.5a_i(t)\Delta t \tag{2.4}$$

Then the position is calculated at a full step as

$$x_i(t+\Delta t) = x_i(t) + v_i(t+0.5\Delta t)\Delta t \tag{2.5}$$

Next, from the interaction potentials, derive $a_i(t+\Delta t)$, using $x_i(t+\Delta t)$:

$$a_i(t+\Delta t) = \frac{1}{m}\sum_{k=1}^{N} F_i^k\left[x_i(t+\Delta t)\right] \tag{2.6}$$

Here $N$ is the number of segments that interact with a given segment.

Finally, $v_i(t+\Delta t)$ is found as

$$v_i(t+\Delta t) = v_i(t+0.5\Delta t) + 0.5a_i(t+\Delta t)\Delta t \tag{2.7}$$

Computing rotational dynamics of cylindrical segments requires more advanced time integration approaches. In this work I utilize 4-th order Runge-Kutta method, combined with quaternion representation of rotations. Its full derivation is presented in [65-67]. This method is a part of PFC$^{3D}$5.0 software, used in our simulations. A brief overview of this time integration approach follows.

The following notation is used: $\hat{e}_i$ is the inertial frame of reference ($i = 1..3$), $\hat{\hat{E}}_i$ is convective (rotating with the rigid body) frame of reference. One transforms to another with rotation matrix:

$$\hat{e} = \bar{R}\hat{\hat{E}} \tag{2.8}$$

Conventional time integration algorithms for 3D rigid body rotation [65] are based on discrete timesteps of time $\Delta t$, evolving the matrix $\bar{R}$, by multiplying it by the rotation increment matrix $\bar{Q}$. Calculation of the matrix $\bar{Q}$ is based on Euler equations. Such an approach has certain drawbacks: successive matrix multiplications can lead to error accumulation. Error accumulation, in turn, can lead to a loss of the orthonormality property of the rotation matrix ( $\bar{R} : \bar{R}^T = \bar{R}^{-1}$ ). In the molecular dynamics [68] and computer graphics [69] communities, these issues are overcome through the use of Hamilton quaternions. Such an approach have the following advantages: i) non-singularity under rotation, ii) ease of renormalization between time steps to avoid the loss of orthonormality, and iii) because of 4 degrees of freedom, instead of the 9 in the rotation matrix, there are fewer operations required to update the rotation of a body.

Within this approach to time integration, angular velocity $\vec{\omega}$, distinct element rotation axial vector $\vec{r}$ and its increment $\vec{q}$ are represented as quaternions $\langle \omega_0 \quad \vec{\omega} \rangle, \langle r_0 \quad \vec{r} \rangle$, $\langle q_0 \quad \vec{q} \rangle$. Axial vector to quaternion operator is defined as

$$\hat{E}(\vec{\vartheta}) = \left\langle \cos\left(\frac{1}{2}\left|\vec{\vartheta}\right|\right) \quad \frac{1}{2}\frac{\sin\left(\frac{1}{2}\left|\vec{\vartheta}\right|\right)}{\frac{1}{2}\left|\vec{\vartheta}\right|}\vec{\vartheta} \right\rangle \tag{2.9}$$

Quaternion to rotation matrix operator is:

$$\bar{R}(\langle q_0 \quad \vec{q}\rangle) = \begin{pmatrix} q_0{}^2 + q_1{}^2 - 0.5 & q_1q_2 - q_3q_0 & q_1q_3 + q_2q_0 \\ q_1q_2 + q_3q_0 & q_0{}^2 + q_2{}^2 - 0.5 & q_2q_3 - q_1q_0 \\ q_1q_3 + q_2q_0 & q_2q_3 - q_1q_0 & q_0{}^2 + q_2{}^2 - 0.5 \end{pmatrix} \tag{2.10}$$

Within quaternion formalism the incremental rotation of a rigid body is represented by a consequent multiplication of the current rotation quaternion $\langle r_0 \quad \vec{r}\rangle$ and rotation increment quaternion $\langle q_0 \quad \vec{q}\rangle$. The operation of quaternion multiplication is defined as:

$$\begin{aligned} &\langle q_0 \quad \vec{q}\rangle \circ \langle r_0 \quad \vec{r}\rangle = \langle p_0 \quad \vec{p}\rangle \\ &p_0 = r_0q_0 - \vec{r}\vec{q} \\ &p = r_0\vec{q} + q_0\vec{r} + \vec{r}\times\vec{q} \end{aligned} \tag{2.11}$$

The algorithm of calculation of the rotation quaternion and angular velocity on a next timestep $\langle r_0 \quad \vec{r}\rangle_{t+\Delta t}$, $\langle \omega_0 \quad \vec{\omega}\rangle_{t+\Delta t}$ based on the values of $\langle r_0 \quad \vec{r}\rangle_t$, $\langle \omega_0 \quad \vec{\omega}\rangle_t$ is as follows.

For the first approximation we have:

$${}_{(1)}\langle q_0 \quad \vec{q}\rangle = \frac{\Delta t}{2}\langle \omega_0 \quad \vec{\omega}\rangle_t \tag{2.12}$$

Approximation for the angular velocity is updated as

$$
{}_{(2)}\langle \omega_0 \quad \vec{\omega} \rangle = \hat{E}\left\{ \left[ \bar{R}\left( {}_{(1)}\langle q_0 \quad \vec{q} \rangle \circ \langle r_0 \quad \vec{r} \rangle_t \right) I^{-1} \bar{R}\left( {}_{(1)}\langle q_0 \quad \vec{q} \rangle \circ \langle r_0 \quad \vec{r} \rangle_t \right)^T \right] \right.
$$
$$
\left. \left[ \bar{R}\left( \langle r_0 \quad \vec{r} \rangle_t \right) I \bar{R}\left( \langle r_0 \quad \vec{r} \rangle_t \right)^T \vec{\omega} + \vec{M} \Delta t \right] \right\} \tag{2.13}
$$

Here $\vec{M}$ is external moment acting on an element. This relation follows from Euler equations of rotational motion (for the detailed derivation see [65, 66]). The second approximation becomes

$$
{}_{(2)}\langle q_0 \quad \vec{q} \rangle = \frac{\Delta t}{2} \quad {}_{(2)}\langle \omega_0 \quad \vec{\omega} \rangle \tag{2.14}
$$

Similarly,

$$
{}_{(3)}\langle \omega_0 \quad \vec{\omega} \rangle = \hat{E}\left\{ \left[ \bar{R}\left( {}_{(2)}\langle q_0 \quad \vec{q} \rangle \circ \langle r_0 \quad \vec{r} \rangle_t \right) I^{-1} \bar{R}\left( {}_{(2)}\langle q_0 \quad \vec{q} \rangle \circ \langle r_0 \quad \vec{r} \rangle_t \right)^T \right] \right.
$$
$$
\left. \left[ \bar{R}\left( \langle r_0 \quad \vec{r} \rangle_t \right) I \bar{R}\left( \langle r_0 \quad \vec{r} \rangle_t \right)^T \vec{\omega} + \vec{M} \Delta t \right] \right\}
$$
$$
{}_{(3)}\langle q_0 \quad \vec{q} \rangle = \frac{\Delta t}{2} \quad {}_{(3)}\langle \omega_0 \quad \vec{\omega} \rangle \tag{2.15-2.18}
$$
$$
{}_{(4)}\langle \omega_0 \quad \vec{\omega} \rangle = \hat{E}\left\{ \left[ \bar{R}\left( {}_{(3)}\langle q_0 \quad \vec{q} \rangle \circ \langle r_0 \quad \vec{r} \rangle_t \right) I^{-1} \bar{R}\left( {}_{(3)}\langle q_0 \quad \vec{q} \rangle \circ \langle r_0 \quad \vec{r} \rangle_t \right)^T \right] \right.
$$
$$
\left. \left[ \bar{R}\left( \langle r_0 \quad \vec{r} \rangle_t \right) I \bar{R}\left( \langle r_0 \quad \vec{r} \rangle_t \right)^T \vec{\omega} + \vec{M} \Delta t \right] \right\}
$$
$$
{}_{(4)}\langle q_0 \quad \vec{q} \rangle = \Delta t \quad {}_{(4)}\langle \omega_0 \quad \vec{\omega} \rangle
$$

Using these four approximations the resulting rotational quaternion increment is calculated based on 4-th order Runge-Kutta formula:

$$\langle q_0 \quad \vec{q} \rangle = \frac{1}{6}\Big( {}_{(1)}\langle q_0 \quad \vec{q} \rangle + 2_{(2)} \langle q_0 \quad \vec{q} \rangle + 2_{(3)} \langle q_0 \quad \vec{q} \rangle + {}_{(4)} \langle q_0 \quad \vec{q} \rangle \Big)$$
$$\langle r_0 \quad \vec{r} \rangle_{t+\Delta t} = \langle q_0 \quad \vec{q} \rangle \circ \langle r_0 \quad \vec{r} \rangle_t \tag{2.19}$$

Although this time integration scheme is non-symplectic, it provides stable time integration. Small energy drift is compensated by damping (see section 2.7).

### 2.5 Representation of intratube interactions

A CNT surface is formed by a regular arrangement of covalently bonded atoms of carbon. As was demonstrated in [46, 57], in terms of effective mechanical behavior the CNT surface can be viewed as an elastic continuum shell. Small strain deformations of this shell, in turn, can be predicted with beam theory assumptions. Therefore, in order to reproduce realistic behavior of CNTs in a linear regime of deformation, it is sufficient to ensure that the chain of coarse-grained elements behaves as an elastic beam under tension, twisting, shear and torsional loads.

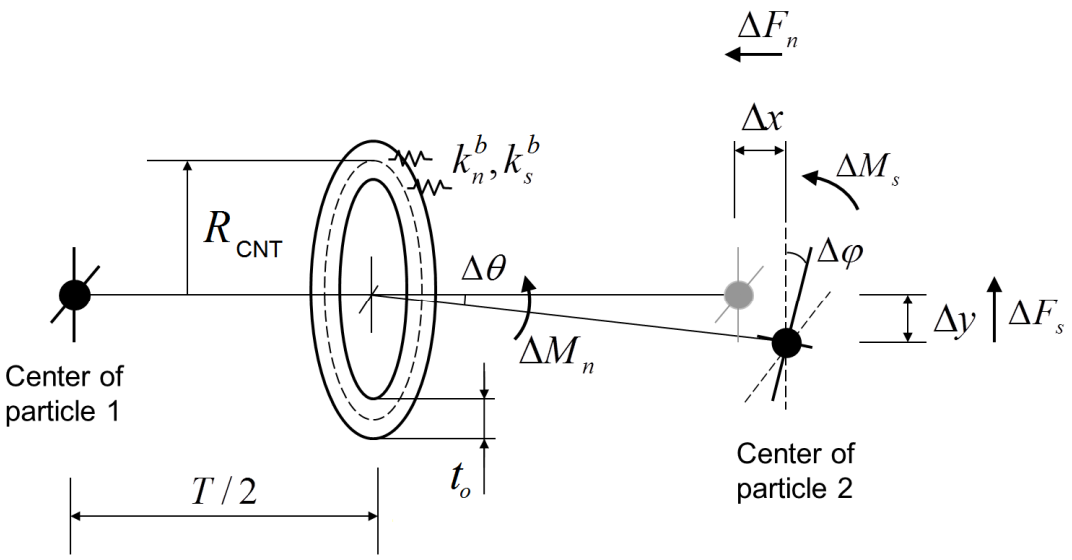


Figure 5: Parallel bond model for elasticity of a CNT segment.

In order to capture the elastic behavior of CNTs we employ and parameterize the standard DEM parallel bond contact model, presented in [64]. Parallel bond provides an interface of distributed springs (Fig. 5), resisting to stretching, shearing, bending and torsional deformations, according to the following incremental laws:

$$\Delta x = -k_n{}^b A^b \Delta F_n, \quad \Delta y = -k_s{}^b A^b \Delta F_s, \quad \Delta\theta = -k_n{}^b I^b \Delta M_n, \quad \Delta\varphi = -k_s{}^b J^b \Delta M_s \tag{2.20}$$

where $A^b$ , $I^b$ , $J^b$ are area, moment of inertia and polar moment of inertia of a cylindrical cross section:

$$A^b = 2\pi R_{CNT} t_0, \quad I^b = \pi R_{CNT} t_0 (R_{CNT}{}^2 + 0.25 t_0{}^2), \quad J^b = 2I^b. \tag{2.21}$$

$k_n{}^b = E_{CNT}/T$ , $k_s{}^b = G_{CNT}/T$ - distributed normal and shear stiffnesses of a CNT bond

contact; $t_0 = 3.35\,\text{Å}$ is thickness of CNT wall, accepted to be equal to interlayer vdW spacing; $E_{CNT} = 1029$ GPa, $G_{CNT} = 459$ GPa - values of CNTs Young's and shear moduli respectively, which are determined from the results of atomic-scale simulations [70]. Variables $\Delta x, \Delta y, \Delta\theta, \Delta\varphi$ denote increments of normal and shear displacement components, and bending and twisting angles; $\Delta F_n, \Delta F_s, \Delta M_n, \Delta M_s$ are increments of projections of normal force, shear force, bending moment and twisting moment (Fig. 5). Chain of parallel bonded segments behaves as an elastic beam with corresponding cross section and elastic moduli. Appendix A elaborates on this statement with an analytical illustration of the small-slope deformation of a cantilever beam.

Table 2 gives parameters of parallel bond interface for $(10,10)$ CNTs.

Table 2. Parallel bond parameters for $(10,10)$ CNTs.

| $k_n^b$, eV/Å$^4$ | $k_s^b$, eV/Å$^4$ | $A^b$, Å$^2$ | $I^b$, Å$^4$ | $J^b$, Å$^4$ |
|---|---|---|---|---|
| 0.474 | 0.211 | 142.7 | 3,480 | 6,960 |

Normal and shear components of total force and moment are monitored during the simulation. Local radius of curvature ($r_{curv}$), normal ($\varepsilon_t$) and shear ($\varepsilon_s$) tensile strain, as well as maximum strain associated with bending ($\varepsilon_b^{\max}$) and twisting ($\varepsilon_{tw}^{\max}$) deformations of a CNT are calculated as:

$$\varepsilon_t = \frac{F_n}{k_n A^b T} \quad \varepsilon_s = \frac{|F_s|}{k_s A^b T} \quad \varepsilon_b{}^{\max} = \frac{|M_n|}{2k_n I^b} \quad \varepsilon_{tw}{}^{\max} = \frac{|M_s|}{2k_s J^b} \quad r_{curv} = \frac{T}{k_n I^b}|M_n| \tag{2.22}$$

We note that tensile/compressive strain is monitored with sign, whereas only magnitude is monitored for shear, bending and twisting strains.

The total elastic strain energy is expressed as a sum of tension, shear, bending and torsion terms:

$$E_{tot} = E_{ten} + E_{she} + E_{ben} + E_{twi}$$
$$E_{ten} = \frac{F_n{}^2}{2k_n A^b} \quad E_{she} = \frac{F_s{}^2}{2k_s A^b} \quad E_{ben} = \frac{M_n{}^2}{2k_n I^b} \quad E_{twi} = \frac{M_s{}^2}{2k_s J^b} \tag{2.23}$$

It worth noting here that according to recent findings [71] the continuum model fails to predict the bending stiffness of a monolayer of graphite. Graphene appears to be more compliant than what is predicted by the model of continuum plate with thickness $t = 3.35$ Å. However, this does not significantly affect the bending stiffness of a SWCNT in our model. Indeed, the bending stiffness of a segment of length $T$ with normal stiffness $K_n{}^b = k_n{}^b A^b$ is given as:

$$EI^b = k^b T I^b = \frac{K_n{}^b T}{A^b} I^b = \frac{K_n{}^b T}{2\pi R_{CNT} t_0} \pi R_{CNT} t_0 (R_{CNT}{}^2 + 0.25 t_0{}^2) = \frac{K_n{}^b T}{2} (R_{CNT}{}^2 + 0.25 t_0{}^2) \tag{2.24}$$

One can see that the bending stiffness of a SWCNT is determined by a leading term $R_{CNT}{}^2$ in (2.24) and only weakly depends on the assumed thickness $t_0$ .

It is also important to note that the suggested formalism is valid only for small strains, due to inherent limitations of parallel bond model, *i.e.* coupling between bending and twisting that occurs when large-angle bending and twisting coexist [72]. This question is further discussed in section 2.9.

Initially deposited CNTs should not necessarily be created as unstrained straight beams. Relations (2.19) allow creation of strained or initially curved configurations as well. Correct initial contact forces and moments should be specified in accordance with initial geometry of a chain of segments.

### 2.6 The treatment of vdW interactions between CNT segments

In most applications CNTs are present in the form of ropes, cables, and papers. Their collective mechanical behavior originates not only on the covalent but also weak van der Waals (vdW) C-C interactions that build up over extended contacts. One of the central parts of this work is the derivation of a contact model that can efficiently capture these non-bonding vdW interactions between CNTs.

Broadly speaking, physical theories of van der Waals forces can be separated into two camps: microscopic and macroscopic. The microscopic theory is a bottom-up approach based on the atom-atom dispersion interaction of London [73], in which the total interaction is thought of as a sum of contributing parts of the microscopic constituents. Under the assumption of pairwise additivity, the microscopic dispersive interactions sum to describe the total interaction between macroscopic bodies. In an opposite top-down fashion, macroscopic theories of Hamaker and Lifshitz [74, 75] start with the dispersive

energy between macroscopic bodies.

In my work I develop a contact model for two interacting cylinders by expanding on a previous model resulted from the microscopic integration [46] of Lennard-Jones potential for carbon [46]. The resulting model can be parameterized to capture the known differences in vdW adhesion strength between metallic and semiconducting CNTs that follow from macroscopic analysis [76, 77].

For a general atomistic system the non-bonding interactions between two neutral atoms (1 and 2) are well described by the conventional Lennard-Jones (LJ) pair potential:

$$u_{12}(r_{12}) = 4\varepsilon\left(\left(\frac{\sigma}{r_{12}}\right)^{12} - \left(\frac{\sigma}{r_{12}}\right)^{6}\right)$$
$$\vec{f}(\vec{r}_{12}) = -\frac{du}{d\vec{r}_{12}} = -\vec{f}(\vec{r}_{21}) \qquad (2.25)$$

Here $\vec{r}_{12}$ is the radius-vector between two atoms, $\varepsilon$ the bond energy between two atoms at the equilibrium distance and $\sqrt[6]{2}\sigma$ the equilibrium distance. Consider two bodies $V_1$ and $V_2$, consisting of particles interacting with pair potential $u(r_{12})$. Particles are uniformly distributed over the volumes of bodies with volume density $\rho_v$ (volume element $dV$ contains $\rho_v dV$ particles). The radius vector $\vec{r}_{12}$ connects two arbitrary volume elements $dV_1$ and $dV_2$, and vector $\vec{R}_{12}$ connects centers of masses of body 1 and body 2. Denote $\vec{n}_{R12} = \vec{R}_{12} / \left|\vec{R}_{12}\right|$. The normal component of force acting between two bodies is:

$$(\vec{F}_{12})_{n_{R12}} = \rho_v^{\,2} \iint\limits_{V_1V_2} (\vec{f}_{12})_{n_{R12}}\, dV_1 dV_2 = \rho_v^{\,2} \iint\limits_{V_1V_2} \frac{du_{12}}{d\vec{r}_{12}} \vec{n}_{R12} dV_1 dV_2 =$$
$$\rho_v^{\,2} \iint\limits_{V_1V_2} \frac{du_{12}}{dR_{12}} dV_1 dV_2 = \frac{d}{dR_{12}} \left( \rho_v^{\,2} \iint\limits_{V_1V_2} u_{12} dV_1 dV_2 \right) \qquad (2.26)$$

Therefore, the problem of finding the total interaction force between two bodies yields to integration of vdW potential. It is easy to demonstrate that the resulting integral potential would be a pair potential only for particular case of spherical coarse-grained particles. General shapes of interacting bodies lead to non-zero shear component of total contact force, as well as contact moments, that tend to change mutual orientation of the bodies. In most existing coarse-grained procedures, these additional forces and moments are neglected, and the coarse-grained particles representing assemblies of atoms are idealized as spheres (one notable exception is Gay-Berne potential, that is often used in modeling ordering phenomena in liquid crystals [78]).

If one neglects atomic discreteness and assumes that carbon atoms are distributed over CNT surfaces with constant area density, the problem of description of vdW interaction between CNTs is reduced to the problem of finding the integral potential of two identical cylindrical surfaces, interacting via LJ potential. The mutual position of two cylindrical segments can be described with four independent variables (6 degrees of freedom of one rigid body w/r to another are reduced by 2 due to axial symmetries of cylinders). Therefore, the potential sought will be a function of four variables. An analytical integration of LJ potential for arbitrarily oriented cylinders is technically difficult. On the other hand, simple tabulation of the potential is inefficient in terms of practical

applications. In my work I employ the observation [46] that the interaction between cylinders of unit aspect ratios can be well approximated by pair potentials in the far field limit. I corrected for the near-field anisotropy by introducing an adjustment to this effective pair potential [46].

Consider now the derivation of the basic pair potential [46, 47, 79][1]. A continuum approximation is employed, assuming carbon atoms uniformly distributed over cylindrical surfaces with area density $\rho_a = (3\sqrt{3})/4a_{c-c}{}^2$ ($a_{c-c}$ = 1.42 Å is the equilibrium bond length for carbon) such that the number of atom in $dA$ is equal to $\rho_a dA$. Van der Waals energy can be computed in the following way (here and below indexes "12" are omitted):

$$U = \rho_a{}^2 \int_{A_1}\int_{A_2} u(r) dA_1 dA_2 \tag{2.27}$$

For two parallel tubes, presented in Fig. 6(A) (in cylindrical coordinates $dA_1 = R_{CNT}\, d\theta_1 dz_1$, $dA_2 = R_{CNT}\, d\theta_2 dz_2$) the potential energy per unit length can be calculated as

$$U/T = 4\varepsilon\rho_a{}^2 R_{CNT}{}^2 \int_0^{2\pi}\int_0^{2\pi}\int_{-\infty}^{\infty}\left(\left(\frac{\sigma}{r}\right)^{12} - \left(\frac{\sigma}{r}\right)^{6}\right) dz_2 d\theta_1 d\theta_2, \tag{2.28}$$

where $r = \sqrt{R_{CNT}{}^2 + l^2 - 2R_{CNT} l\cos\theta_2 + z_2{}^2} = \sqrt{\tilde{T}^2(\theta_1,\theta_2) + z_2{}^2}$,

[1] The derivation (2.27 – 2.35) presented here mostly follows the one performed by E. Akatyeva (Dontsova)[79] and partly published in [46].

$l = \sqrt{R_{CNT}{}^2 + d^2 - 2R_{CNT}\, d \cos\theta_1}$ , $d$ is the distance between tube centers (Fig. 6(B))

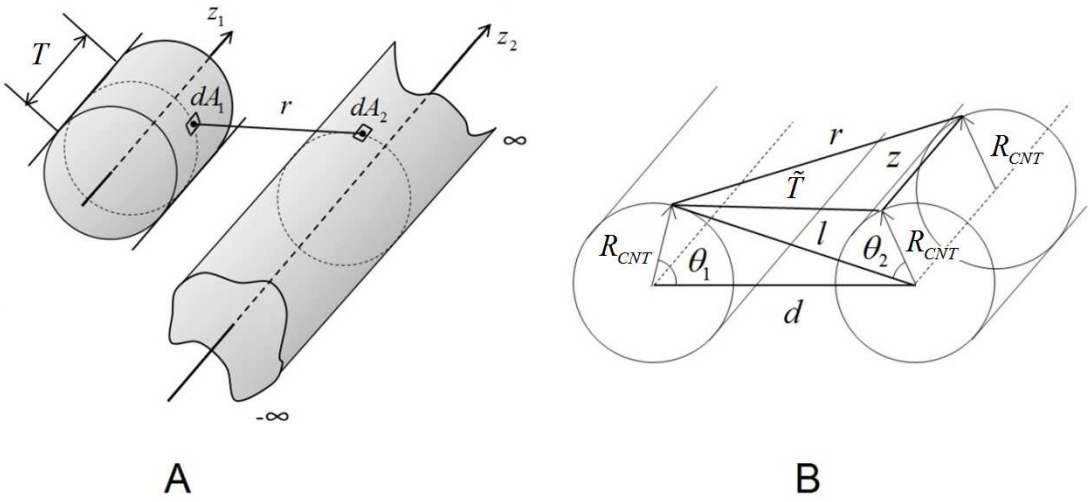


Figure 6. (A) Integration of pairwise Lennard-Jones interactions resulting in interaction energy per unit length. (B) Schematic detailing the geometry of the problem.

Integrate over $z_2$ by changing the variable $\varsigma = z_2 / \tilde{T}$ :

$$\int_{-\infty}^{\infty} r^{-6} dz_2 = \int_{-\infty}^{\infty} (\tilde{T}^2 + z_2{}^2)^{-3} dz_2 = \frac{1}{\tilde{T}^5} \int_{-\infty}^{\infty} (1+\varsigma^2)^{-3} d\varsigma = \frac{3\pi}{8} \frac{1}{\tilde{T}^5}$$
$$\int_{-\infty}^{\infty} r^{-12} dz_2 = \int_{-\infty}^{\infty} (\tilde{T}^2 + z_2{}^2)^{-6} dz_2 = \frac{1}{\tilde{T}^{11}} \int_{-\infty}^{\infty} (1+\varsigma^2)^{-6} d\varsigma = \frac{63\pi}{256} \frac{1}{\tilde{T}^{11}} \quad (2.29)$$

Introduce

$$\tilde{r} = \tilde{T}^2 / R_{CNT}{}^2 = 2 + (d / R_{CNT})^2 - 2(d / R_{CNT}) \cos\theta_1 - 2\sqrt{1 + (d / R_{CNT})^2 - 2(d / R_{CNT}) \cos\theta_1}\, \cos\theta_2 .$$

Then the potential energy per unit length is:

$$U/T = 4\varepsilon\rho_a{}^2 \frac{3\pi\sigma^6}{8R_{CNT}{}^3}\left(\frac{21\sigma^6}{32R_{CNT}{}^6}\int_0^{2\pi}\int_0^{2\pi}\frac{d\theta_1 d\theta_2}{\tilde{r}^{11/2}} - \int_0^{2\pi}\int_0^{2\pi}\frac{d\theta_1 d\theta_2}{\tilde{r}^{5/2}}\right) \tag{2.30}$$

Consider near field limit ($d/R_{CNT} = 2+\tau$ , $\tau << 1$). Applying Taylor series expansions for sine, cosine and square root functions and taking into account leading terms w/r to $\theta_1, \theta_2$ and $\tau$ :

$$\begin{aligned}
&\tilde{r} = 2+(d/R_{CNT})^2 - 2(d/R_{CNT})\cos\theta_1 - 2\sqrt{1+(d/R_{CNT})^2 - 2(d/R_{CNT})\cos\theta_1}\cos\theta_2 = \\
&2+(2+\tau)^2 - 2(2+\tau)\cos\theta_1 - 2\sqrt{1+(2+\tau)^2 - 2(2+\tau)\cos\theta_1}\cos\theta_2 = \\
&\theta_2{}^2 + \theta_1{}^4 + o\left(\max\left\{\theta_2{}^2, \theta_1{}^4\right\}\right) + \left[\theta_2{}^2 + 2\theta_1{}^2 + o\left(\max\left\{\theta_2{}^2, \theta_1{}^2\right\}\right)\right]\tau + \\
&+(1-\theta_1{}^2 + o(\theta_1{}^2))\tau^2 + o(\tau^2) = \theta_2{}^2 + (\tau+\theta_1{}^2)^2 + o(\max(\theta_2{}^2, \theta_1{}^4, \tau\theta_1{}^2, \tau^2))
\end{aligned} \tag{2.31}$$

By changing the variables in the integral ($t_1 = \theta_1/\sqrt{\tau}$ $t_2 = \theta_2/\tau$) one can find:

$$\begin{aligned}
&\int_{-\delta_2}^{\delta_2}\int_{-\delta_1}^{\delta_1}\frac{d\theta_1 d\theta_2}{(\theta_2{}^2 + (\tau+\theta_1{}^2)^2)^{n/2}} = \frac{1}{\tau^n}\int_{-\delta_2}^{\delta_2}\int_{-\delta_1}^{\delta_1}\frac{d\theta_1 d\theta_2}{\left[\frac{\theta_2{}^2}{\tau^2} + \left(1+\frac{\theta_1{}^2}{\tau}\right)^2\right]^{n/2}} \approx \\
&\approx \frac{1}{\tau^{n-3/2}}\int_{-\infty}^{\infty}\int_{-\infty}^{\infty}\frac{dt_1 dt_2}{(t_2{}^2 + (1+t_1{}^2)^2)^{n/2}}
\end{aligned} \tag{2.32}$$

($n=5, n=11$). Therefore, the energy per unit length is:

$$U/T = 4\varepsilon\rho_a{}^2 \frac{3\pi\sigma^6}{8R_{CNT}{}^3}\left(\frac{21\sigma^6}{32R_{CNT}{}^6}\frac{a}{(d/R_{CNT}-2)^{19/2}} - \frac{B}{(d/R_{CNT}-2)^{7/2}}\right) \tag{2.33}$$

where

$$a = \int_{-\infty}^{\infty}\int_{-\infty}^{\infty} \frac{dt_1 dt_2}{(t_2{}^2 + (1+t_1{}^2)^2)^{11/2}} \approx 0.4735$$
$$B = \int_{-\infty}^{\infty}\int_{-\infty}^{\infty} \frac{dt_1 dt_2}{(t_2{}^2 + (1+t_1{}^2)^2)^{5/2}} \approx 1.3090 \quad (2.34)$$

Therefore, the vdW energy of the segment of CNT of length $T$, parallel to an infinite second CNT, is given by:

$$V(D) = 4\varepsilon'\left(\frac{A'}{D^{\alpha'}} - \frac{B'}{D^{\beta'}}\right) \quad (2.35)$$

with parameters $\varepsilon'$ , $A'$ , $B'$ , $\alpha'$ , $\beta'$ following from equations (2.33-2.34), and $D = d / R_{CNT} - 2$.

It follows that this potential has an optimal vdW sepatation:

$$r_0 = R_{CNT}\left[\left(\frac{\alpha' A'}{\beta' B'}\right)^{1/(\alpha'-\beta')} + 2\right] \quad (2.36)$$

In spite of the rough asymptotic assumptions, the pair potential (2.35) serves as a good approximation and agrees well with numerically calculated integral (2.27). We utilize the expression (2.35) as a reference for designing our vdW contact model. As $V(D)$ captures the interaction energy between one segment of length $T$ located on first CNT and the second infinitely long CNT, the total vdW interaction energy can be regained by summing the pair interaction between face-to-face segments of length $T$ located on different CNTs. Thus, Eq. (2.35) suggests a naïve contact model in which each two

aligned segments of length $T$ located on different CNTs interact via the spherical symmetric vdW contact model $V(R)$, where $R$ represents the distance between the centers of the spherical particles. It is evident that because the underlying integration has been performed with the CNTs being parallel, this model will be inappropriate for describing the interaction of the crossed CNTs.

Furthermore, this contact model introduces significant artifacts even when the tubes are parallel. The later deficiency is illustrated with an example consisting of two infinite interacting $(10,10)$ CNTs of the length $L_{CNT} = 20.3$ nm represented by 15 identical particles, confined into a volume with periodic boundary conditions applied along CNTs axial direction. Let $V_{DEM}$ be the DEM model intertube potential energy defined as the superposition of all $V(R)f_c(R)$ pairwise contact interactions between the segments of first and second CNT. The polynomial cutoff function $f_c(R)$ is given as:

$$f_c(R) = \sum_{i=0}^{3} Q_i (R/8R_{CNT})^i \tag{2.37}$$

It ensures the absence of energy jumps in the tube-tube potential, associated with cutoff radii of pair interactions (see appendix B). Coefficients $Q_i$ are given in Table 3.

Table 3. Parameters of smooth polynomial cutoff function $f_c(R)$

| $Q_1$ | $Q_2$ | $Q_3$ | $Q_4$ |
|---|---|---|---|
| -80.0 | 288.0 | -336.0 | 128.0 |

Consider first the perfectly aligned case (two CNTs represented by parallel and face-to face positioned segments). The radius of the vdW distinct element was chosen $4R_{CNT}$ = 2.71 nm, which means that one segment located on one CNT interacts with few segments on the second CNT. Although the face-to-face first-neighbor contacts will bring the major contribution to $V_{DEM}$, there are non-negligible contributions from the second- and third-neighbor interactions.

Table 4. Parameterization of the isotropic contact vdW model for the interaction between two (10,10) CNTs. The first line lists the value of the parameters as obtained by direct integration. The second line lists adjusted parameters to correct the next-nearest contacts. The radius of the vdW distinct element is 2.71 nm.

| $\varepsilon'$, *meV* | $A'$ | $B'$ | $\alpha'$ | $\beta'$ |
|---|---|---|---|---|
| 97.45 | 0.0104 | 1.31 | 9.5 | 3.5 |
| 71.24 | 0.0223 | 1.31 | 9.5 | 4 |

There is a quick remedy for this issue facilitated by the transparent form of $V(R)$. To restore $V_{DEM}(L)$ to the desired shape, we still used the functional form of $V(R)$ but the with parameters slightly adjusted to match equilibrium separation $r_0$, $V(r_0)$, and the far field scaling. The original and adjusted parameters of pair potential of interaction between segments of (10,10) tubes with length $T = 2R_{CNT}$ are listed in the first and second line of Table 4, respectively.

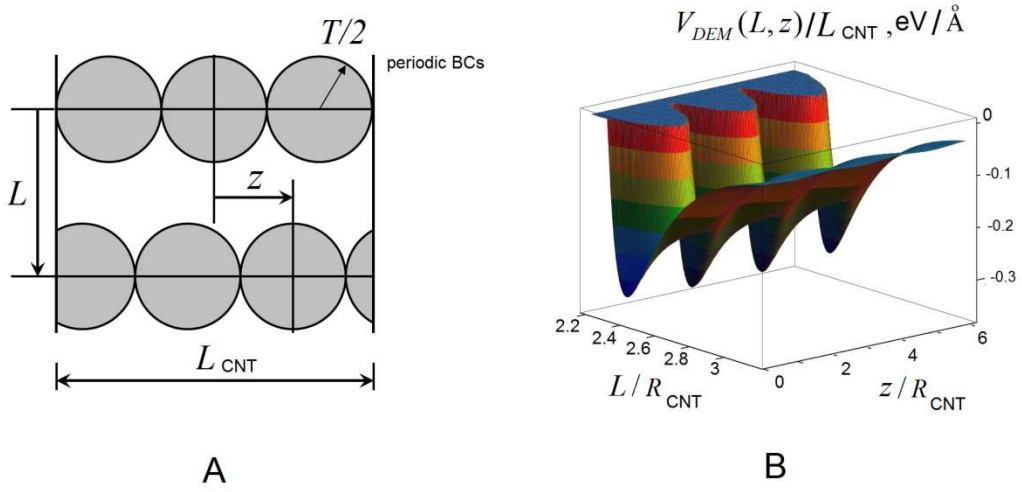


Figure 7. (A) Intertube coordinate system. Distinct elements are visualized as spheres with the radius $R_{CNT} = T/2$. (B) Surface plot of the interaction potential of two parallel infinite (10,10) CNTs as a function of intertube distance $L$ and misalignment $z$.

Next, consider the interaction of misaligned CNTs. The coordinate $z$ describes the misalignment of these adjacent CNTs, Fig. 7(A). The $V_{DEM}(L,z)$ plotted in Fig. 7(B), displays correct intertube spacing and binding energy at $z = 0$. However, for misaligned configurations we note a corrugated relief with periodicity $T$. Of course, this periodic structure of the potential is an artifact of the model. Physically, it introduces unwanted high adhesive shear strength between two parallel CNTs and a preference for staggered ($z = T/2 + nT$ , $n$ - integer) alignments. At this point, it is important to note that the unwanted corrugation artifact is an attribute of the spherical symmetry of the potential used in the contact model.

It should be mentioned that at the microscopic level, there is a real corrugation effect

associated with the graphitic lattice structure of the tube walls and their registry. This effect was discarded in our vdW integration procedure in which atoms were uniformly distributed over cylindrical surfaces. This is significantly weaker effect - the difference in energy between the maximum and minimum energies associated with this corrugation is small compared to the amount of vdW energy associated with bringing two tubes close to their optimal vdW separation [80]. Unfortunately the staggering-induced corrugation becomes large for segments with large $T$, and it can significantly influence the outcome of a coarse grained simulation. For example, these large artificial barriers prevent the long-range rearrangements of CNTs into continuous networks of bundles [41].

The isotropic model (2.35) with parameters given in Table 3 provides the basis for developing a vdW contact model with the following attributes: (i) It has a simple analytical expression and (ii) captures short-range anisotropy to convey the form factors of cylinders and thus to correctly describe the shear interactions between parallel CNTs. (iii) Along with normal and shear forces, it includes moments that tend to align nanotube segments. More specifically, the new model incorporates two adjustments. Firstly, we consider interacting parallel segments and introduce an axial anisotropy of the contact that ensures the smoothness of the potential. Secondly, we introduce the adjustment related to aligning moments that are present in the case of non-parallel axes of the cylindrical segments. For both adjustments, we ensure correct far field behavior by introducing decay and smooth cutoff multipliers.

To restore the smoothness of the interaction we propose to introduce axial anisotropy of the contact model, which now takes a functional form depending on both the center to

center distance $R$ between the segments and the misalignment angle $\theta$, Fig. 8(A).

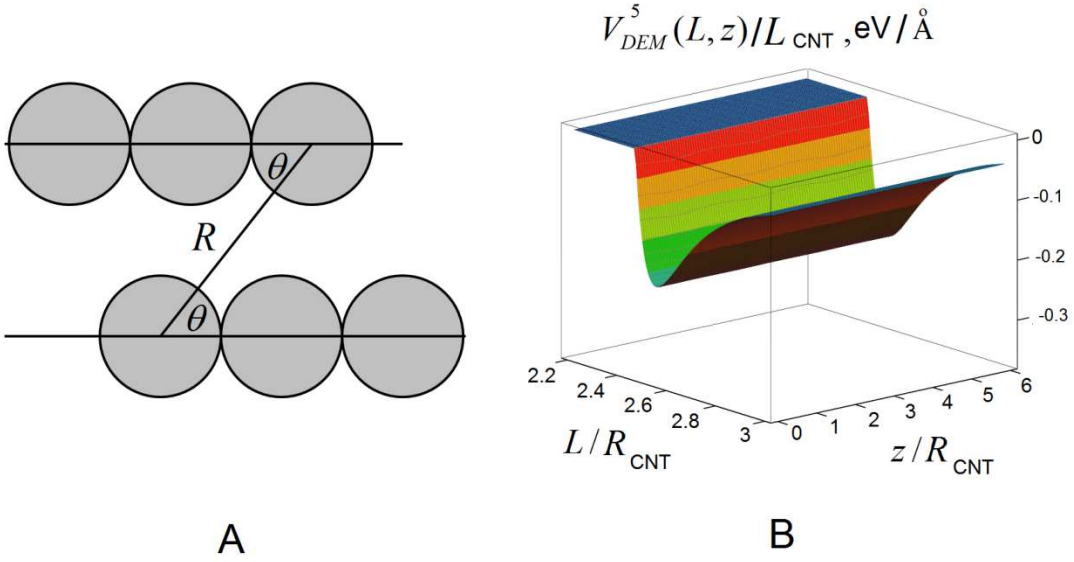


Figure 8. (A) Polar coordinate system associated with pairs of segments located on parallel CNTs.(B) Surface plot of the corrected intertube potential for the interaction of two parallel and finite $(10,10)$ CNTs.

We adjust the axial dependence of the potential using Fourier series with fitted coefficients to counter the energetic preference for staggered orientation. After the adjustment, expression $V(R)$ of the vdW contact model remains unchanged, but the normalized distance $D$ takes the form

$$D^{k}(R,\theta)=\frac{R}{R_{CNT}\Theta^{k}(\theta)}-2 \tag{2.38}$$

The angular function $\Theta^{k}(\theta)$ of the order $k$ writes

$$\Theta^k(\theta) = 1 + \sum_{i=1}^{k} C_i((-1)^{i-1} + \cos(2i\theta)) \tag{2.39}$$

I will refer to the contact model $V(R)$ with the adjustments (2.38) and (2.39) as $V^k(R,\theta)$. The resulted DEM intertube potential is labeled as $V_{DEM}{}^k(R,\theta)$. The set of $k$ constants $C_i$ can be determined via nonlinear fitting, by requiring equal values of the inter-tube potential for $k+1$ misaligned states evaluated at the equilibrium intertube distance $L_0$:

$$V_{DEM}{}^k(\mathrm{r}_0, z_i = iT/2k) = V_{DEM}{}^k(\mathrm{r}_0, 0), \quad i = 1..k \tag{2.40}$$

Note that the expression (2.39) is equal to $1$ for $\theta = \pi/2$. However, because the next-nearest contacts are altered by the angular adjustment, the resulting intertube potential $V_{DEM}{}^k$ will be affected even in the case of aligned CNTs ($z = 0$).

Therefore, the obtained potential should be renormalized so that it would give the correct value of adhesion energy for aligned configuration. This can be easily achieved by rescaling $\varepsilon'$ to an appropriate $K\varepsilon' = \varepsilon''$ value. The parameterization of anisotropic adjustment of vdW contact model for $(10,10)$ CNT is given in Table 4 below (the correction function used 5 harmonics). The resulting interaction between two (10,10) CNTs with aspect ratio of 15 is shown in Fig. 8(B).

My procedure of the potential "ironing" appears to be very effective. As one can see from the comparison of Figs. 7(B), and 8(B), the corrected pair potential gives more realistic potential, with suppressed periodic structure associated with spherically symmetric

interactions. Note that for corrected potential the adhesion energy per unit length ( $\xi = V_{DEM}{}^{k}(\mathrm{r}_0) = 0.21$ eV/Å for $(10,10)$ CNTs) is constant and does not depend on relative translation $z$.

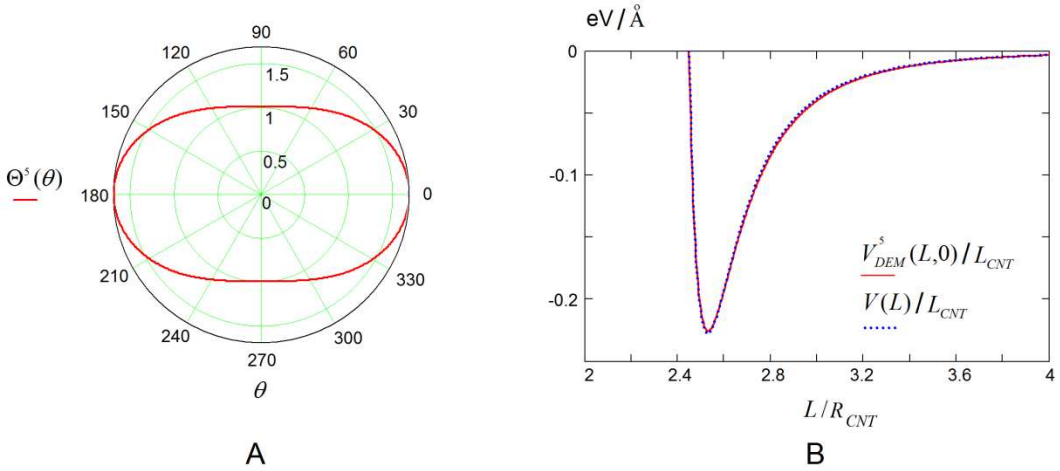


Figure 9. Details on the anisotropic vdW contact model for $(10,10)$ CNTs. (A) Polar plot of $\Theta^5(\theta)$. $\theta = \pi/2$ corresponds to face-to-face interaction between segments. (B) Corrected total potential as a function of normalized intertube spacing in comparison with the analytical intertube potential (2.35).

Fig. 9(A) gives a polar plot of the obtained $\Theta_5(\theta)$ from which it becomes apparent that the potential $V^5{}_{DEM}$ flattening via angular adjustment is due to shrinking of the real distance between misaligned segments ( $\theta \neq \pi/2$ ). We emphasize that all these adjustments do not affect the intertube interaction of the perfectly aligned CNTs. This can be seen in Fig 6(B), which compares $V^5(L,0)$ with the intertube potential obtained by the microscopic integration.

Having solved the problem of formation of deep potential wells, I now focus on the case when two CNTs are crossed, with a crossing angle $\gamma$. This extension is done in such a way, that the crossing angle $\gamma$ and anisotropy correction angle $\theta$ are orthogonal coordinates. One possible solution is presented in Fig. 10(A). Within this approach the angle $\theta$ in the case of crossed CNTs is defined as an angle between the contact unit vector $\vec{n}_R$ (directed from element 1 to element 2 ) and vector sum of first ( $\vec{n}_{b1}$ ) and second ( $\vec{n}_{b2}$ ) axial directions.

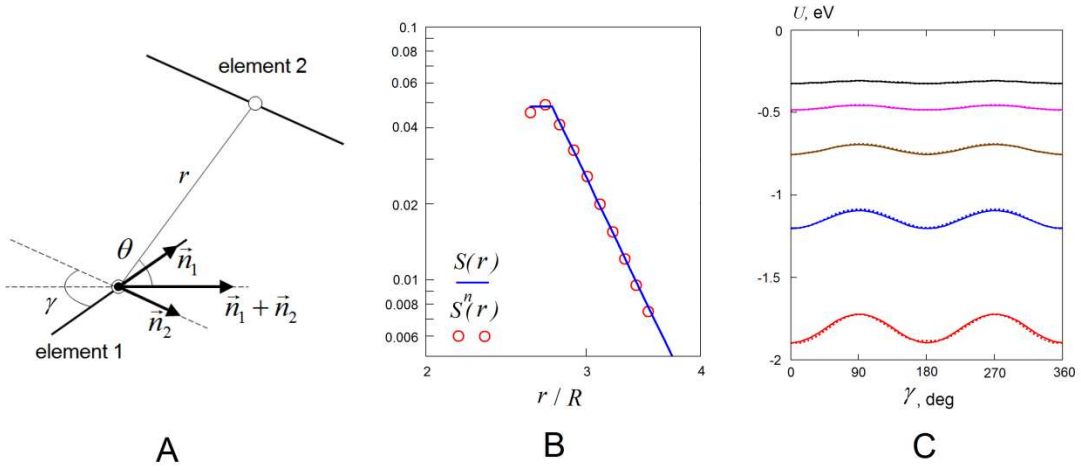


Figure 10. (A) Definition of the angles $\theta$ and $\gamma$. (B) Numerically integrated anisotropy function, fitted with analytical expression (2.43). (C) Numerically integrated potential of interaction as the function of the crossing angle $\gamma$ for few separation distances $R$ (solid line) as compared to the analytical potential described by expressions (2.41-2.43).

This definition incorporates the limit case of parallel nanotubes and preserves kinematical independence between $\theta$ and $\gamma$, which allows to treat them as independent

variables. The normal ( $F_R$ ) and shear ( $F_\theta$ ) contact forces lay in uniquely defined "neutral" plane, which does not depend on permutation of first and second CNTs. An aligning moment ( $M_\gamma$ ), acting between two misaligned CNT segments may be introduced as discussed below.

The integrated LJ potential of two cylindrical segments depends on the angle $\gamma$ between their axes. This leads to the presence of contact moments that tend to align cylindrical segments. In the case of aspect ratios of the segments close to 1, angular dependence of the potential can be neglected, what is typically done in BS models. However, correct aligning moments are important for self-assembly processes. If we would like to consider an anisotropic nature of vdW interaction that is predicted by macroscopic theories [77] it is important to have the technical possibility of incorporation of the aligning moments. In this case the potential given by expressions (2.35, 2.38, 2.39) has to be enriched with an additional multiplier that favors certain orientations:

$$U(R,\theta,\gamma) = V_k(R,\theta)\Gamma(R,\gamma) \tag{2.41}$$

Similarly to adjustment (2.38, 2.39), such multiplier may be obtained as a Fourier series with respect to the angle $\gamma$ . We find that anisotropy of the numerically integrated potential of two interacting cylinders is well described by a single harmonic adjustment

$$\Gamma(R,\gamma) = 1 + W_\gamma(R)(1-\cos(2\gamma)) \tag{2.42}$$

Here, the function $W_\gamma(R)$ determines the strength of anisotropy and the correct power

of its decay with distance. Note that $\Gamma(R,\gamma) \le 1$, $(\Gamma(R,0) = 1)$.

Consider the approximation of anisotropy of LJ potential $U_n$, numerically integrated over the cylindrical segments with $T = 2R_{CNT}$ (Fig 8(A)). We assume that

$$W_\gamma(R) = C_\gamma (R/R_{CNT})^\delta \tag{2.43}$$

We introduce the anisotropy function of the potential *U* as

$$S(R) = \frac{1}{2}\left|\frac{U(R,\theta,\gamma=0) - U(R,\theta,\gamma=\pi/2)}{U(R,\theta,\gamma=0)}\right| \tag{2.44}$$

and the same function for numerically integrated potential,

$$S^n(R) = \frac{1}{2}\left|\frac{U^n(R,\gamma=0) - U^n(R,\gamma=\pi/2)}{U^n(R,\gamma=0)}\right| \tag{2.45}$$

In the case of the potential given by expressions (2.35, 2.38, 2.39) with the adjustment (2.41-2.43) we have $S(R) = W_\gamma(R)$. In the case of numerically integrated potential this function can be found directly. We assume that it depends only on the intercenter distance $R$. Fig. 10(B) gives the numerical solution for $S_n(R)$, plotted for few different distances $R$, presented in logarithmic coordinates.

The numerical solution is fitted with the function $C_\gamma (R/R_{CNT})^\delta$. The parameters $C_\gamma$ and $\delta$ found by numerical fitting are given in Table 5. Fig. 10(C) presents the comparison between analytical potential (2.41) and numerically integrated one, given as functions of

the crossing angle $\gamma$ for selected values of normalized separation distances $R/R_{CNT}$. It is observed that the analytical expressions (2.41-2.43) provide good representation of the angular dependence of the potential of two aligned ($\theta=\pi/2$) cylinders.

Table 5. Parameterization of anisotropic adjustments of the vdW contact between two (10,10) CNTs.

| $C_1$ | $C_2$ | $C_3$ | $C_4$ | $C_5$ | $C_\gamma$ | $\delta$ |
|---|---|---|---|---|---|---|
| 0.35819 | 0.03263 | -0.00138 | -0.00017 | 0.00024 | 90 | -7.5 |

For the values of $R$ smaller than $R_m = 2.75R_{CNT}$ CNT we assume that the anisotropy function is constant and equal to $S(R_m)=W(R_m)$. It is important to note that our adjustment (2.41-2.43) captures the angular dependence of the potential only for the attractive part of the potential, which is of practical importance for self-assembly problems. We do not consider the dependence associated with the repulsive part ($2R_{CNT} < R < R_m$), which may favor misaligned states.

Summarizing, we can write down the vdW contact of distinct elements as:

$$
\begin{aligned}
&U(R,\theta,\gamma) = f_c(R)V^k(R,\theta)\Gamma(R,\gamma)\\
&V^k(R,\theta) = \varepsilon'\left(\frac{A'}{D^k(R,\theta)^{\alpha'}} - \frac{B'}{D^k(R,\theta)^{\beta'}}\right)\\
&D^k(R,\theta) = \frac{R}{R'_{CNT}\Theta^k(\theta)} - 2\\
&\Gamma(R,\gamma) = 1 + W_\gamma(R)(1-\cos(2\gamma))\\
&\Theta^k(\theta) = 1 + \sum_{i=1}^{k} C_i((-1)^{i-1} + \cos(2i\theta))\\
&W_\gamma(R) = C_\gamma(R / R_{CNT})^{\delta'}\\
&f_c(R) = \sum_{i=0}^{3} Q_i(R / 8R_{CNT})^i
\end{aligned}
\tag{2.46}
$$

The parameters for vdW contact model are presented in Tables 3 and 4. Normal force, shear force and aligning moment acting between two distinct elements can be found as

$$
F_R = -\frac{\partial U}{\partial R} \quad F_\theta = -\frac{1}{R}\frac{\partial U}{\partial \theta} \quad M_\gamma = -\frac{\partial U}{\partial \gamma} \tag{2.47}
$$

The corresponding stiffnesses are

$$
k_R = \left|\frac{\partial^2 U}{\partial R^2}\right| \quad k_\theta = \left|\frac{1}{R^2}\frac{\partial^2 U}{\partial \theta^2}\right| \quad k_\gamma = \left|\frac{1}{R^2}\frac{\partial^2 U}{\partial \gamma^2}\right| \tag{2.48}
$$

The potential (2.46) has been implemented into an existing code and used for vdW adhesion energy computations. Forces and moments (2.47) are used in dynamics computations; stiffnesses (2.48) are used to estimate the stable time step for time integration algorithms [63] and the admissible magnitude of dissipative (viscous) forces. Full set of analytical expressions for components of force and stiffnesses is given in the

Appendix B.

As we noted, some artificial corrugation of the potential can be introduced by the multiplication of constants $C_1 \ldots C_5$ by some additional factor with simultaneous rescaling the energy $\varepsilon''$. This approach can be used to introduce some small static friction between CNTs. However, in many cases this method leads to significant artifacts in model's behavior and should be used with caution in every particular problem.

**2.7 Energy dissipation**

As has been emphasized in the beginning of Chapter 2, a mesoscopic model should provide correct representation of the energy exchange between DOFs that are explicitly present in the model and the ones eliminated in the coarse-graining procedure. As has already been discussed, the energy of thermal fluctuations does not lead to significant deformations of carbon nanotubes, and therefore CNTs (unlike polymer molecules) should be viewed as macroscopic bodies, *i.e.* the energy exchange between explicit and implicit DOFs is represented only with dissipation.

From a physics viewpoint, one can distinguish two channels of energy dissipation in CNT systems – intratube dissipation, related to inelastic deformations of CNTs, and intertube dissipation associated with relative CNT sliding.

The first type of dissipation was considered in the literature [45]. It was found that the intratube dissipation is mostly associated with nonlinear regimes of CNT deformations (buckling of single wall CNTs and rippling of MWCNTs.) In linear regimes intratube

dissipation can be neglected.

The role of intertube dissipation was also studied in the literature [81]. Qualitative explanation of the energy dissipation micromechanisms was given based on the idea of forced vibrations of carbon atoms that are pulled from their vdW registry. This idea is illustrated with simple single degree of freedom system shown in Fig 11(A).

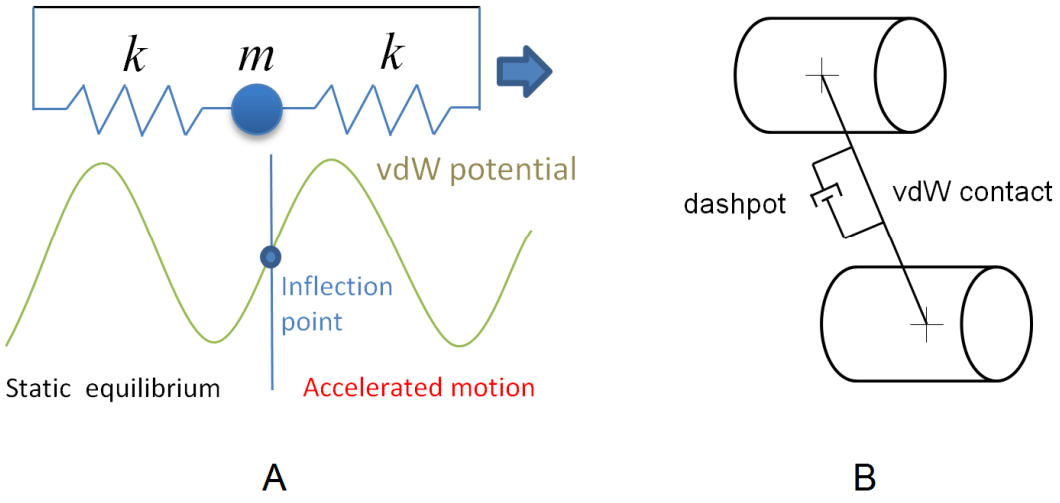


Figure 11. (A) Simple model illustrating the mechanism of energy dissipation in CNT sliding (B) Representation of energy dissipation in CNT sliding with viscous dampers, acting in parallel with vdW contacts.

A spring-mass system is moved in a periodic potential. If the motion starts from the potential minimum, the system remains in static equilibrium until it reaches the inflection point. After inflection point is passed, the potential force (decreasing as a second power of displacement of $m$ ) does not compensate spring force (decreasing linearly with displacement of $m$ ), and $m$ starts to move with acceleration. This mechanism

dominates energy transfer from relative sliding of CNTs to the energy of atomic oscillations, *i.e.* heat energy. Here we restrict ourselves with this simple qualitative illustration. Quantitative analysis of the behavior of similar models (which are known as generalized Prandtl-Tomlinson models of friction) is presented in [82]. Both theoretical considerations [82] and experimental results [83] indicate rate dependence of energy losses in CNT sliding.

Hierarchical calibration of intertube sliding dissipation poses a significant problem. First, due to huge gap in a time scales, it is impossible to reliably extrapolate the results of MD simulations to macroscopic time scales and strain rates of interest in real applications. Second, at long enough times ($\mu s$ and longer) heat radiation exchange processes (that are usually neglected in MD at $ps$ time scales) become important part of total energy balance.

Introducing intertube dissipation into the DEM mesoscopic model was one focus of my work [49]. Two types of damping are present – local damping and viscous damping. Local damping, introduced to stabilize non-symplectic time integration, acts at each segment and applies components of damping force $F_i^{\chi}$ (moment $M_i^{\chi}$) proportional to the corresponding components of unbalanced force $F_i$ (moment $M_i$) acting on a segment, according to the following relations:

$$F_i^{\chi} = -\chi F_i sign(v_i), \quad M_i^{\chi} = -\chi M_i sign(\omega_i), \quad i = 1...3. \tag{2.49}$$

Here $v_i$ and $\omega_i$ are components of the translational and rotational velocity of a segment,

$sign\,(x)$ the sign function. Coefficient $\chi$ is chosen between 0 and 0.7.

Viscous damping is introduced to represent energy dissipation during CNT sliding. Since direct, bottom-up calibration of damping is problematic, a top-down approach is used, where viscous damping coefficient is a free parameter, chosen to reproduce the mechanical behavior observed experimentally (see the discussion in Chapter 3).

The viscous force can be envisioned as a dashpot (Fig. 11(B)), acting in parallel with potential forces, prescribed by a vdW contact model. Normal $F_n^{\psi}$ and tangential $F_s^{\psi}$ force developed by a dashpot is proportional to normal $v_n$ and tangential $v_s$ relative velocity of elements in contact:

$$F_n^{\psi} = c_n v_n, \quad F_s^{\psi} = c_s v_s. \tag{2.50}$$

viscosities $c_n, c_t$ are related to the viscous damping coefficient as follows:

$$c_n = 2\psi\sqrt{m k_n}, \quad c_t = 2\psi\sqrt{m k_t}, \tag{2.51}$$

here $k_n, k_s$ are stiffnesses of contact model. In case of constant stiffness model coefficient $\psi$ has the meaning of critical damping ratio. Since our vdW contact model has complex reactive stiffnesses (see appendix B), nominal values $k_n = 1\,\mathrm{eV/Å^2}$, $k_s = 1\,\mathrm{eV/Å^2}$ are used to calculate $\psi$ .

## 2.8 Additional features and future extensions

The model components described above constitute the basis of the of the DEM mesoscopic model for carbon nanotubes. The model allows studying self-folding and self-assembly of CNTs, as well as the mechanics of CNT materials. In this section we consider few straightforward extensions of the model, and some possible future developments.

Many possible applications of the model in a field of processing of CNT materials and structures require modeling the substrate. The simplest approach to model a substrate is to prescribe an external potential, describing the vdW interactions between CNTs and the substrate [35]. Within PFC$^{3D}$ toolkit the substrate can be easily modeled with wall facets [63]. This approach is sufficient for problems of self-assembly of supported CNT films, as well as problems involving percolation threshold analysis in such films. For the problems involving CNTs on a deformable substrate, one can use coupling with explicit dynamics continuum solvers like FLAC [84].

In most of the applications involving high-performance CNT materials, CNTs are cross-linked with chemical bonds. From the mechanical point of view a cross-link molecule can be viewed as a breakable spring with significant normal stiffness, but negligible shear, bending and torsional stiffnesses. Calibration of the stiffness and strength of a cross-link is based on the effective radial potential for a covalent bond. Within PFC$^{3D}$ this kind of bonds can be successfully modeled with breakable parallel bonds [63]. Calibration and parameterization of some kinds of such bond is discussed in section 3.3.

Parallel bond formalism is inefficient in modeling large deformations and failure of CNTs themselves, because the assumption of smallness of relative deflections is violated. Therefore, more advanced models are needed for accurate representations of large strain deformations and failure of CNTs. One model that is appropriate for generalization on the case of large deformations is presented in [85].

An alternative approach to modeling CNT failure can be based on concurrent multiscale modeling [54], when the elements subjected to a critically large strain are replaced with full-atomistic model, seamlessly bridged with the coarse-grained region. Current PFC3D implementation with tracing of elements orientations is suitable for such modeling.

# Chapter 3

# Applications

In the previous Chapter we have considered all important steps in development of the DEM mesoscopic model. Starting from a full-scale microscopic description, we have introduced necessary coarse-graining procedures and came up with an efficient description of large-scale collections of CNTs with the reduced-order dynamic model.

In this chapter I describe illustrative applications of the developed model that not only validate it, but also provide valuable insights on the self-assembly and mechanics of individual CNTs and their collections with different morphologies.

Trivial validation examples of CNT free vibrations, static deformations and adhesion are left aside of this description - all those demonstrate the validity of the model for small-strain local deformations.

The Chapter starts with examples demonstrating stability of certain self-folded configurations of CNTs. This set of examples validates the model in application to real CNT structures observed experimentally.

Next, we consider the mechanical behavior of aligned 1D CNT structures, linked either by solely vdW adhesion or both vdW forces and chemical bonds (cross-links). This consideration demonstrates good agreement with existing experimental data and previous full-atomistic numerical experiments. The last section of the Chapter 3 is

focused at two-dimensional CNT structures - free-standing CNT films. Self-assembly and mechanics of a 2D specimen of a CNT film are studied.

All considered examples demonstrate the usefulness of the developed model and contribute to understanding of the nanoscale mechanics of CNT materials. However, these examples also reveal natural limitations of the DEM model. A critical summary of these limitations is one of the topics of Chapter 4.

### 3.1 Modeling self-folded CNT systems

Self-folded CNT configurations are often encountered in experiment. These nanostructures are prospective in a number of areas of nanotechnology; in particular, they can be useful in energy storage applications [48]. Geometry and energy balance of stable CNT structures are good validation of our mesoscopic model. In this chapter we will consider two types of self-folded CNT structures – single- and multiple-coil CNT rings and CNT rackets.

Unclosed CNT rings [7] are CNTs folded into rings that are stabilized by vdW adhesion forces. In experiment these structures can be produced with high yields in a process of ultra-sonic radiation of a CNT liquid suspension: CNTs stick to a multiple bubbles that are formed in the suspension in a cavitation process, and then fold into rings when bubbles collapse [7]. Consider here the DEM modeling of CNT ring assembly. The $(10,10)$ CNT of length $L_{CNT}$ = $271.2$ nm was represented by 200 elements. The initial and final configuration of the CNT ring is given in Fig. 12(A). The simulation of the relaxation required $24{,}000$ time steps or $0.6$ ns. Fig 12 (B) shows the evolution of the different

energy terms. As can be seen from the plots, the final equilibrium state is characterized by the balance of elastic strain energy and vdW potential energy. The equilibrium parameters of a CNT ring can be assessed with a simple analytical model. Consider the CNT ring shown in Fig 12 (C), with radius $R_r$, length $L_{CNT}$, and overlap length $\Delta l$. We assume for simplicity the ideal circular shape of an equilibrium ring configuration. The vdW adhesion energy of a ring with overlap $\Delta l$ may be well approximated as $-\xi\Delta l$. Assume also that the strain energy of a deformed CNT is the energy of an elastic beam in pure bending state under the bending moment $M$:

$$U_{str} = \frac{M^2}{2EI} L_{CNT} = \left(\frac{EI}{R_r}\right)^2 \frac{L_{CNT}}{2EI} = \frac{EIL_{CNT}}{2R_r^2} = \frac{EIL_{CNT}}{2} \frac{4\pi^2}{(L_{CNT} - \Delta l)^2} \tag{3.1}$$

Here $EI$ is a CNT bending stiffness of a CNT. The total potential energy of the ring (Fig. 12(D))

$$U_r = -\xi\Delta l + \frac{2\pi^2 EIL_{CNT}}{(L_{CNT} - \Delta l)^2} \tag{3.2}$$

has a minimum for

$$\Delta l = L_{CNT} - \sqrt[3]{\frac{4\pi^2 EIL_{CNT}}{\xi}} \tag{3.3}$$

Therefore, the minimum length of a CNT allowing stable CNT ring is

$$L_{CNT}^{\min} = 2\pi\sqrt{\frac{EI}{\xi}} \tag{3.4}$$

The equilibrium configuration reached in the DEM simulation is characterized by $\Delta l = 51.5\,\text{nm}$, which is in close agreement with the $\Delta l = 49.7\,\text{nm}$ value assessed with equation (3.3).

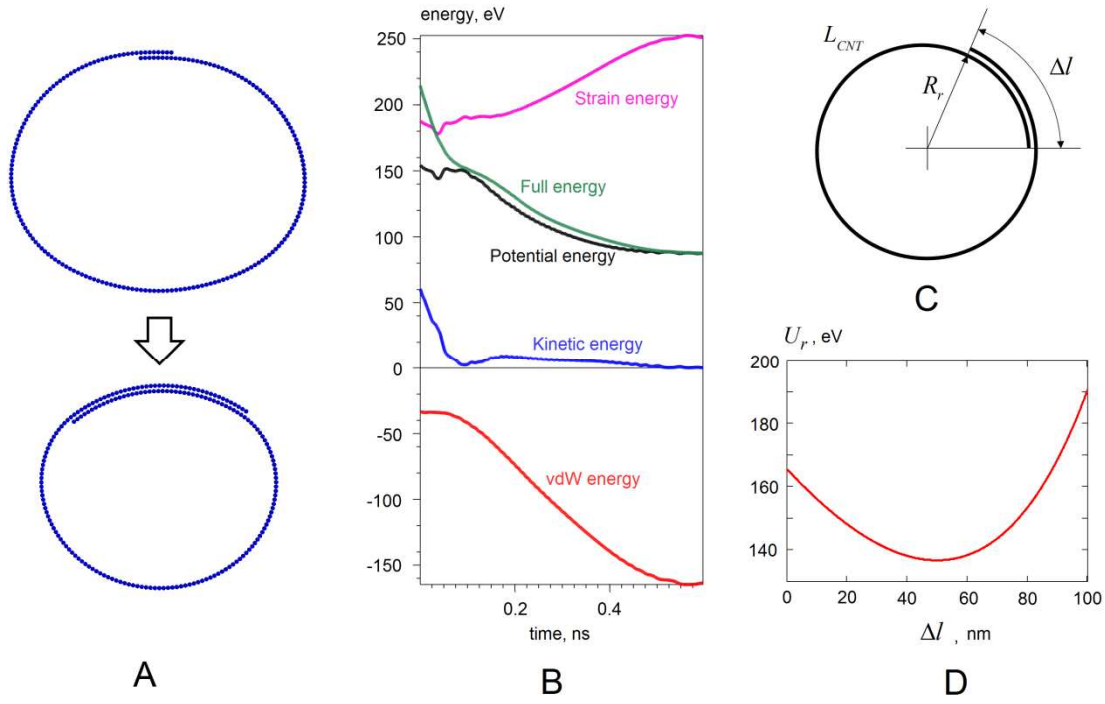


Figure 12. CNT ring relaxation. (A) Evolution of the CNT ring shape during the DEM simulation. (B) Evolution of energy terms during the simulation. (C) Schematics for the simplified analytical model. (D) Potential energy as a function of the overlap segment length for the analytical model.

We also investigated how the CNT ring morphology obtained by DEM compares with direct microscopic modeling. The same $(10,10)$ CNT ring was simulated using the

molecular dynamic code Trocadero [86] using a classical Tersoff potential [27] to describe the covalent bonding between carbon atoms, and a Lennard-Jones potential with the parameters given in Chapter 2 to capture the long-ranged bonding. We started the microscopic simulations from the state with the equilibrium overlap distance predicted by the mesoscopic model. The system containing $132{,}900$ atomic degrees of freedom was evolved in time from a “cold" start for $7.4$ ps with a velocity Verlet algorithm. The full atomistic simulations demonstrated good agreement in the most important details. During the MD simulation time, the overlap length and the ring radius didn’t change significantly (Fig 13(A)). There were however certain details, such as nonlinear deformation (buckling) of a CNT surface at the point of contact with the internal edge (Fig 13(B))

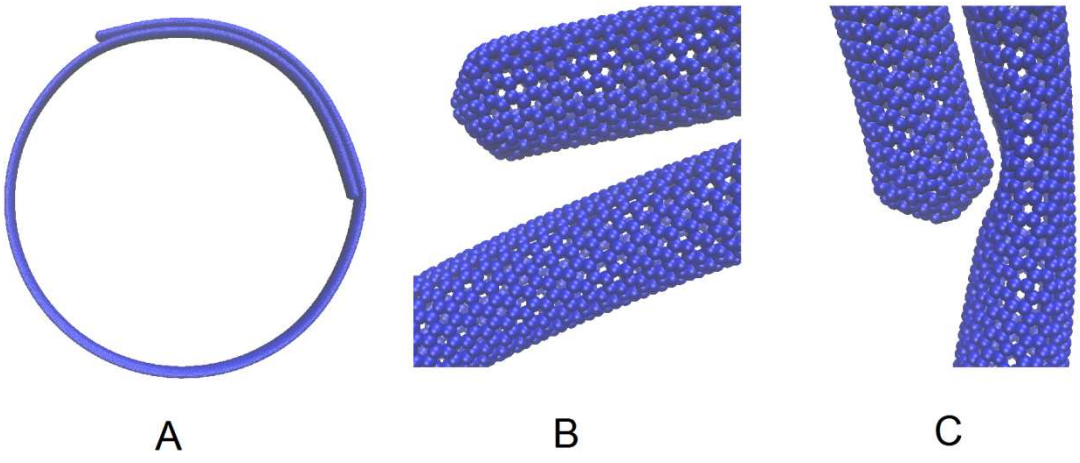


Figure 13. Molecular dynamic simulation of a $(10,10)$ CNT ring. (A) Ring shape after $7.4$ ps of time evolution. (B) Buckling of a CNT at the point of contact with its edge. (C) Separation of the free edge of a CNT. Visualization was carried out using VMD [87].

and the small separation of an external edge of a folded CNT (Fig 13(C)), that could not be captured by the DEM mesoscopic model. It is worth to note that the microscopic simulation took $150$ hours on one core of a computational cluster, which was approximately $6\cdot 10^6$ times slower than the DEM simulation for the whole ring formation.

For a $(10,10)$ CNT the minimal stable length predicted by (3.5) is equal to $200$ nm, which agrees well with the numerical modeling, which predicts the stability of a $160$ nm long CNT.

Analysis (3.1)-(3.3) was later generalized for CNT rings with multiple turns [48]. The expression for elastic energy remains the same, whereas adhesive energy is expressed with piecewise linear function:

$$U=\begin{cases} -\xi_1\Delta l & 0<\Delta l<L_{CNT}/2 \\ -\xi_2\Delta l & L_{CNT}/2<\Delta l<L_{CNT}/3 \\ -\xi_3\Delta l & L_{CNT}/3<\Delta l<L_{CNT}/4 \\ & \dots \end{cases} \tag{3.5}$$

Here $-\xi_i$ are adhesive energies per unit length that correspond to close-packed crystals of $i+1$ CNTs. For the first few CNTs in a crystal adhesive energies are roughly proportional to the number of nearest neighbors in a crystal, as shown in Fig. 14(B) (for $i>2$ more accurate analysis require taking into account next-nearest neighbors interactions).

This simple model predicts the stability of multiple-coiled CNT rings, which is justified by the DEM simulations Fig. 14(C).

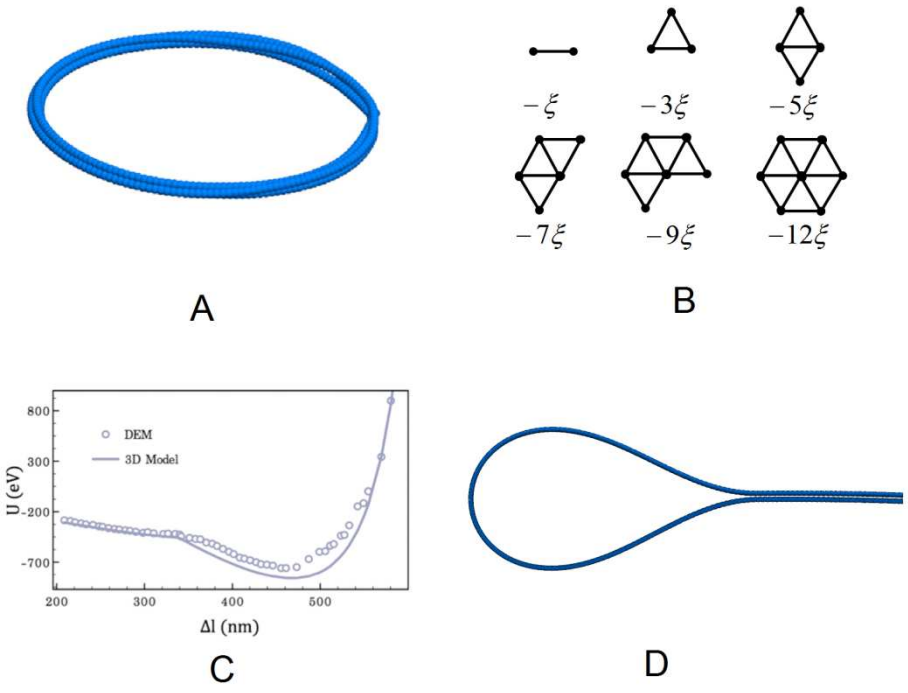


Figure 14. (A) Multiple-coil CNT ring. (B) Adhesive energies of first few close-packed CNT configurations (only nearest-neighbor interactions are taken into account). (C) Potential energy of the (10, 10) CNT ring of the length $L_{CNT} = 680\ nm$. (solid line gives analytical expression, points are DEM results). (D) CNT racket.

Another type of a CNT self-folded configuration is a CNT racket (Fig. 14(D). An exact analysis of geometry and energy balance of a CNT racket is presented in [88]. In particular, the minimal stable length is found to be

$$L_{CNT}^{\min} \approx 12\sqrt{\frac{EI}{\xi}} \tag{3.6}$$

For $(10,10)$ CNTs this expression gives $L_{CNT}{}^{\min} = 380$ nm, which is in qualitative agreement with the length of stable rackets of $200$ nm, observed in DEM simulation.

Our recent experimental-numerical study [89] explicitly demonstrated the agreement in sizes and stiffnesses of self-assembled structures observed experimentally and in DEM model.

### 3.2 Tensile tests on aligned CNT structures

CNT bundles and CNT ropes [12-16, 90-92] are promising structures for many technological applications. Twisted CNT yarns are candidate structures for electromechanical torsional actuators and artificial muscles [12]. Crystalline CNT bundles and CNT ropes, consisting of micrometer-long CNTs, are of great interest as wires and cables with high tensile load bearing capacity [13-15, 92] and thin and flexible conductors that can be embedded onto polymer composites [91]. In the next few sections we consider the mechanical behavior of aligned CNT structures under various types of mechanical loading. We start with simple tension tests, revealing a number of interesting properties of CNT materials.

#### *3.2.1 Assembly of a test specimen*

We will be using a particular kind of close-packed structure in our subsequent mechanical tests. Fig. 15(A) presents our model of a close-packed bundle of CNTs. Positions and displacements of distinct elements are described in a Cartesian coordinate system with $X$ axis parallel to the axis of a bundle. The bundle has regular hexagon

cross section. The side of a hexagon is $(N-1)r_0$, where $N$ is number of tubes along the side (which will also be referred to as *thickness factor* of a bundle), and $r_0$ is equilibrium distance between CNT axes in a bundle, conditioned by the minimum of integral tube-tube vdW potential. For $(10,10)$ CNTs $r_0 = 17.1\,\text{Å}$. The number of CNTs on a bundle cross section and its effective area are given by

$$N_{CNT} = 1 + 3N(N-1),$$
$$S = \frac{3\sqrt{3}}{4}\left[1 + 3N(N-1)\right]r_0^{\,2}. \tag{3.7}$$

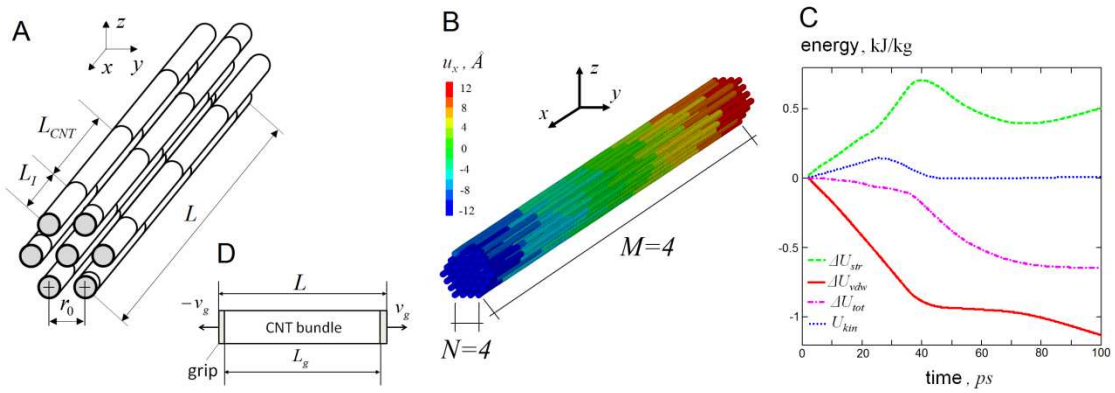


Figure 15. (A) Schematics of a crystalline CNT bundle ($N = 2$). (B) Geometry of the pre-relaxed bundle ($N = 4$, $M = 4$). Color (grayscale) legend gives $x$ - component of displacements developing during the relaxation. (C) Changes in different terms of CNT bundle energy during pre-relaxation. The change in strain energy $\Delta U_{str}$, vdW adhesion energy $\Delta U_{vdw}$, total energy $\Delta U_{tot}$, and kinetic energy $U_{kin}$ are presented. (D) Gage and grip regions of a CNT bundle specimen.

The bundle of length $L$ consists of hexagonal arrangement of rows of CNTs with the same length $L_{CNT}$, such that $L_{CNT} < L$. The ratio $M = L / L_{CNT}$ will be referred to as *length factor* of a CNT bundle.

CNTs in a row initially do not have any spacing between their edges (Fig. 15(A)); vdW interaction between the edges is not prescribed. For each row, positions of CNT joints are defined by the distance $L_I$ between one of the edges of a bundle and the nearest CNT edge (Fig. 15(A)); $L_I$ is random with uniform distribution on the interval $(0, L_{CNT})$. We will denote the number of elements along the bundle as $P = L / T$, and aspect ratio of a single CNT as $p = L_{CNT} / T$.

The specimen is assembled in the following way: hexagonal CNT bundle, described above, is generated at the initial moment and allowed to relax for 10000 cycles, or $0.1$ ns (it worth noting here that the time of this evolution is affected by the damping present in mesoscale model and does not directly correspond to the time of evolution in full atomistic model). During that time it contracts in $X$ - direction due to vdW adhesion (Fig. 15(B)), leading to approximately $0.3\%$ decrease in length, and elastic strain energy of approximately $0.5$ kJ/kg (Fig. 15(C)). In a process of initial relaxation bundles may also develop lateral deformations, and store part of elastic energy in bending. It happens due to inherent asymmetry of random positions of joints. As one can see from Fig. 15(C), initial relaxation does not bring the bundle to a global equilibrium, however, the relaxation time is sufficient to exclude the influence of relaxation processes on the stress response during the test. After the initial relaxation two layers of distinct elements at both

edges of a bundle are designated as grips, the elements between grips represent the gage of length $L_g = L - 2T$ (Fig. 15(D)).

After pre-relaxation $x$ positions of grip elements are fixed, while other DOF remained free. Having these constraints introduced, the bundle is equilibrated for additional 1000 cycles ($0.01$ ns), in order to make sure that the initial force acting on a grip is zero.

Next, both grips are gradually accelerated from $0$ to the given velocity $v_g(-v_g)$ (angular velocity $\omega_g(-\omega_g)$) during $5000$ cycles ($0.05$ ns), providing displacement-controlled tension/torsion test. Gradual acceleration is used to reduce the dynamic response, which is significant in case of instantaneous acceleration of the grips.

*3.2.2 Tensile tests – size-dependence of stress-strain curves*

The behavior of CNT bundles subjected to simple tension loading is investigated aiming to establish if a representative volume element (RVE) can be achieved. Systematic tensile tests have been carried out for a collection of CNT bundles with different values of the $L$, $L_{CNT}$, $N$, and $M$ bundle parameters, as given in Table 6. Stress-strain curves (SSCs) were plotted during each test, see Fig. 16 (A) and (B), and Fig. 16 (D) and (E). The tensile stress is defined as $\sigma_{xx} = F_x / S$, where $F_x$ is $x$- component of force acting on the grip. The nominal strain is defined as $\varepsilon_{xx} = 2u_x^g / L$, where $u_x^g$ is $x$- component of the grip displacement. Indexes of stress and strain (strain rate) are omitted below. In the described series of simulations, the bundles were elongated up to 2% strain at the strain

rate $\dot{\varepsilon} = 2\times10^{7}$ s$^{-1}$. Unless otherwise noted, damping coefficients $\chi = 0.7,\ \psi = 0.03$ are used.

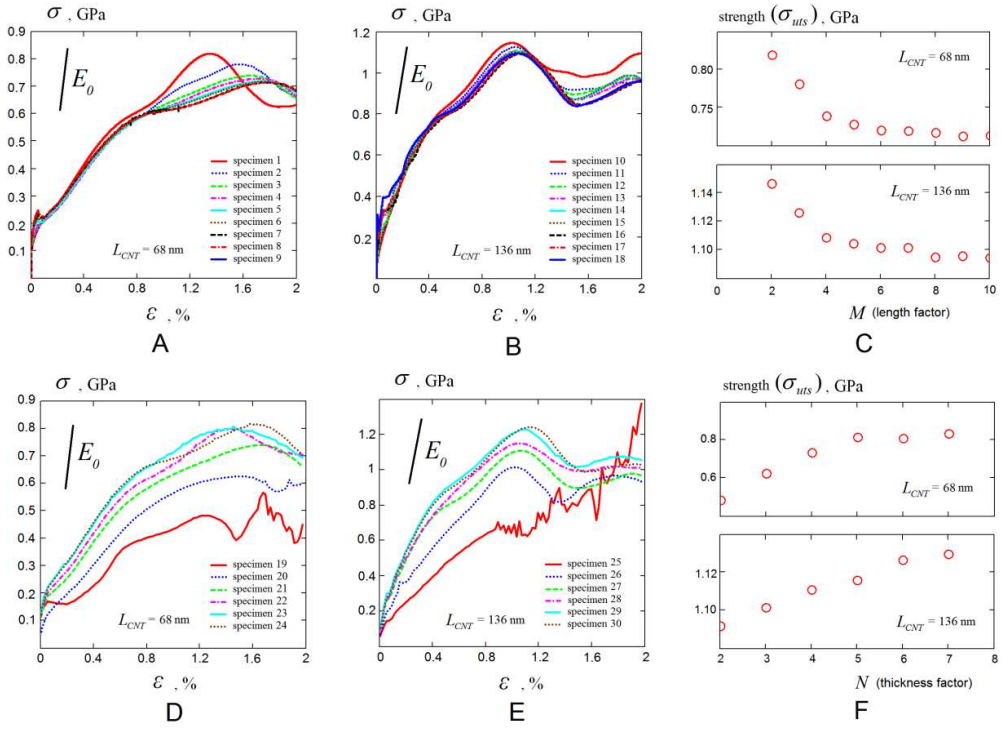


Figure 16. (A, B) SSCs of bundles of different length, containing 37 tubes on a cross section ( $N = 4$ ), for $L_{CNT} = 0.068\,\mu\text{m}$ (specimens 1-9, (A)) and $L_{CNT} = 0.136\ \mu\text{m}$ (specimens 10-18, (B)). (C) Uniaxial tensile strength of a bundle $\sigma_{uts}$ as a function of the length factor $M$ for $L_{CNT} = 0.068\ \mu\text{m}$ and $L_{CNT} = 0.136\ \mu\text{m}$. (D, E) SSCs of bundles of different thickness, with length factor $M = 4$ , and $L_{CNT} = 0.068\ \mu\text{m}$ (specimens 19-24, (D)) and $L_{CNT} = 0.136\ \mu\text{m}$ (specimens 25-30, (E)). (F) Uniaxial tensile strength of a bundle $\sigma_{uts}$ as a function of the thickness factor $N$ for $L_{CNT} = 0.068\ \mu\text{m}$ and $L_{CNT} = 0.136\,\mu\text{m}$. The slope of reference lines given in figures (A,B,D,E) corresponds to Young's modulus $E_0$ estimated for hexagonal arrangement of stretched non-interacting CNTs.

Table 6. Parameters of the tested specimens of CNT bundles.

| **Specimen** | $L$ , μm | $M$ | $L_{CNT}$ , μm | $N$ | $N_{CNT}$ | $v_g$ , m/s |
|---|---|---|---|---|---|---|
| **1** | 0.133 | 2 | 0.068 | 4 | 37 | 1.33 |
| **2** | 0.2 | 3 | | | | 2 |
| **3** | 0.267 | 4 | | | | 2.67 |
| **4** | 0.333 | 5 | | | | 3.33 |
| **5** | 0.4 | 6 | | | | 4 |
| **6** | 0.467 | 7 | | | | 4.67 |
| **7** | 0.533 | 8 | | | | 5.33 |
| **8** | 0.6 | 9 | | | | 6 |
| **9** | 0.667 | 10 | | | | 6.67 |
| | | | | | | |
| **10** | 0.267 | 2 | 0.136 | 4 | 37 | 2.67 |
| **11** | 0.4 | 3 | | | | 4 |
| **12** | 0.533 | 4 | | | | 5.33 |
| **13** | 0.667 | 5 | | | | 6.67 |
| **14** | 0.8 | 6 | | | | 8 |
| **15** | 0.933 | 7 | | | | 9.33 |
| **16** | 1.067 | 8 | | | | 10.67 |
| **17** | 1.2 | 9 | | | | 12 |
| **18** | 1.333 | 10 | | | | 13.33 |
| | | | | | | |
| **19** | 0.267 | 4 | 0.068 | 2 | 7 | 2.67 |
| **20** | | | | 3 | 19 | |
| **21** | | | | 4 | 37 | |
| **22** | | | | 5 | 61 | |
| **23** | | | | 6 | 91 | |
| **24** | | | | 7 | 121 | |
| | | | | | | |
| **25** | 0.533 | 4 | 0.136 | 2 | 7 | 5.33 |
| **26** | | | | 3 | 19 | |
| **27** | | | | 4 | 37 | |
| **28** | | | | 5 | 61 | |
| **29** | | | | 6 | 91 | |
| **30** | | | | 7 | 121 | |

A typical SSC of a CNT bundle consists of a monotonic growth region up to a peak value and a post-peak evolution. The peak value of stress, which represents the uniaxial tensile strength of a bundle ($\sigma_{uts}$), is about $1$ GPa. As it can be seen in Fig. 16 (C) and (F) it depends on $M$ and $N$ only for short and thin specimens, but it is size-independent for those that are representatively long and thick. Other important parameters of the SSCs – the Young's modulus of a bundle $E$, the critical strain $\varepsilon_c$ (Table 7) at $\sigma_{uts}$, and the monotonic growth shape of the SCC curve, all exhibit the same trends. Interestingly, comparison of the convergence of tensile strength for the two different values of $L_{CNT}$, Fig. 16(C) and (F), suggest that the size of an RVE has a weak dependence on $L_{CNT}$.

We conclude that in the monotonic growth region, the size dependences of SSCs becomes negligible for specimens with $M \geq 4$ and $N \geq 4$. Such specimens can be considered as RVEs of a CNT bundle. One can also estimate the Young's modulus of hexagonal arrangement of non-interacting individually stretched CNTs as:

$$E_0 = E_{CNT}\frac{S_T}{S_C} \quad S_T = 2\pi t_0 R_{CNT} \quad S_C = \frac{3\sqrt{3}}{4} r_0^{\,2} \tag{3.8}$$

Based on the values for $(10,10)$ CNTs given above, one obtains $E_0 = 385$ GPa. As it can be seen in Table 7, the initial Young's modulus of a bundle is overall significantly smaller than $E_0$. This indicates that sliding of CNTs within a bundle significantly decreases the effective elastic modulus.

Table 7. Results of tensile tests on CNT bundles.

| **Spec.** | $E$ , GPa | $\sigma_{uts}$ , GPa | $\varepsilon_c$ ,% | **Spec.** | $E$ , GPa | $\sigma_{uts}$ , GPa | $\varepsilon_c$ ,% |
|---|---|---|---|---|---|---|---|
| **1** | 70.191 | 0.819 | 1.346 | **10** | 145.774 | 1.146 | 1.02 |
| **2** | 63.267 | 0.781 | 1.568 | **11** | 137.162 | 1.126 | 1.05 |
| **3** | 61.8 | 0.738 | 1.646 | **12** | 135.377 | 1.108 | 1.062 |
| **4** | 60.776 | 0.728 | 1.712 | **13** | 127.923 | 1.104 | 1.057 |
| **5** | 60.339 | 0.72 | 1.748 | **14** | 121.273 | 1.102 | 1.069 |
| **6** | 61.53 | 0.719 | 1.745 | **15** | 123.234 | 1.101 | 1.061 |
| **7** | 62.409 | 0.717 | 1.763 | **16** | 127.971 | 1.095 | 1.097 |
| **8** | 62.925 | 0.712 | 1.785 | **17** | 131.678 | 1.096 | 1.09 |
| **9** | 62.472 | 0.713 | 1.778 | **18** | 131.613 | 1.094 | 1.092 |
| | | | | | | | |
| **19** | 25.421 | 0.482 | 1.242 | **25** | 67.898 | 0.917 | 1.349 |
| **20** | 48.716 | 0.625 | 1.527 | **26** | 87.632 | 1.014 | 1.014 |
| **21** | 61.8 | 0.733 | 1.55 | **27** | 135.377 | 1.108 | 1.062 |
| **22** | 65.374 | 0.815 | 1.475 | **28** | 128.223 | 1.158 | 1.06 |
| **23** | 68.849 | 0.809 | 1.451 | **29** | 148.965 | 1.263 | 1.091 |
| **24** | 73.411 | 0.832 | 1.55 | **30** | 152.298 | 1.294 | 1.13 |

*3.2.3 Tensile tests - energy balance and kinematics*

The mechanical response of a CNT bundle presented in the previous section is by the result of the interplay among forces of potential, inertial, and dissipative nature. In order to identify the role of each, we track during simulations the different terms of potential energy, kinetic energy and dissipated energy. The energy balance during displacement control tension test is given by

$$A_{ext}(\Delta) = \int_0^{\Delta} F_{ext}(\Delta')d\Delta' = \Delta K(\Delta) + \Delta U_{str}(\Delta) + \Delta U_{vdw}(\Delta) + \Delta Q(\Delta) \tag{3.9}$$

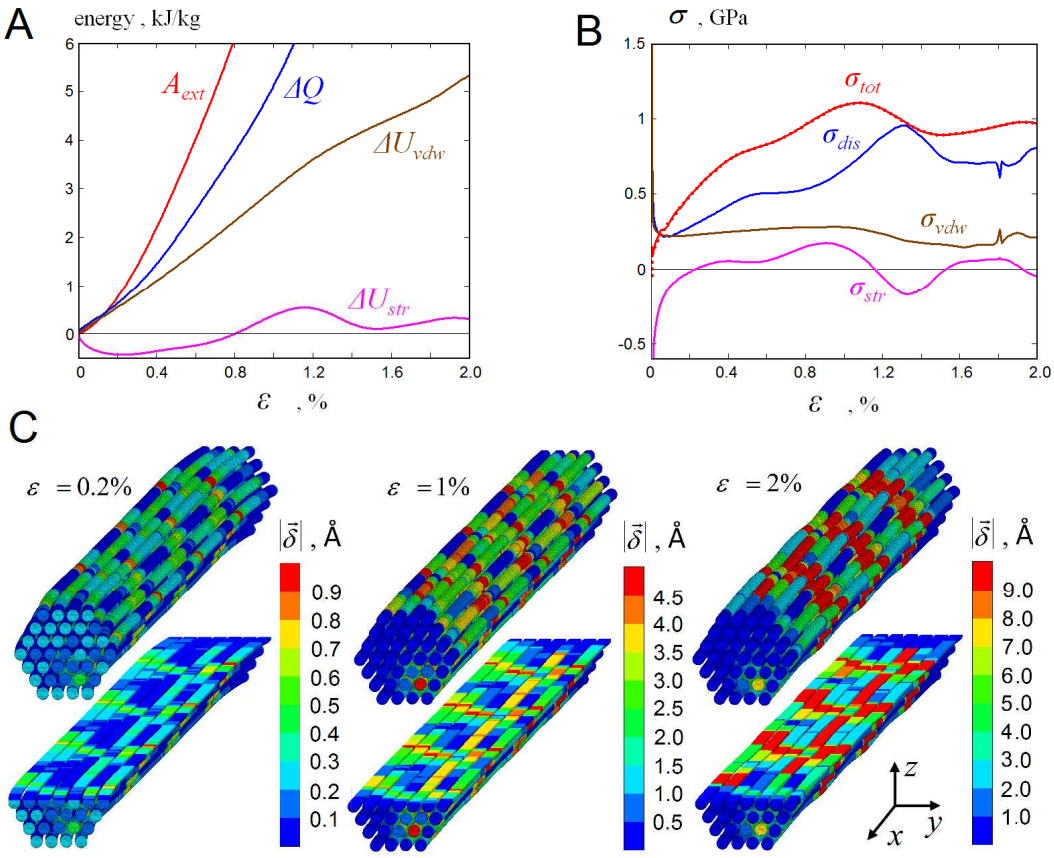


Figure 17. (A) Work of external force $A_{ext}$, as compared to changes in elastic strain energy $\Delta U_{str}$, vdW adhesion energy $\Delta U_{vdw}$, and dissipated energy $\Delta Q$ during the test. (B) Terms of decomposition (13) during the simulation. Total stress response $\sigma_{tot}$ is calculated as a sum of derivatives of traced energy terms (dashed line) and directly from force balance (solid line). (C) Development of a localized deformation in a CNT bundle. Visualization of CNT bundle geometry and magnitude of a slip vector (on the surface of a bundle and on a horizontal axial cross section of a bundle).

Here $\Delta$ ($\Delta'$) is the absolute elongation of a CNT bundle; $A_{ext}(\Delta)$ is the work done by external force $F_{ext}(\Delta)$ during the test; $\Delta K(\Delta)$ is the change in kinetic energy during the

simulation; $\Delta U_{str}(\Delta)$ is the change in total strain energy (sum of CNTs stretching, bending, shearing and torsion); $\Delta U_{vdw}(\Delta)$ is the change in vdW adhesion energy, associated with the formation of a new vdW surface; and $\Delta Q(\Delta)$ is the energy dissipated by local and viscous damping that represents heating of a CNT bundle. In a quasi-static test the changes in the kinetic energy appear to be negligible compared to other terms. By formal differentiation of (3.9) with respect to $\Delta$, and omitting the kinetic energy term one has:

$$F_{ext}(\Delta) = \frac{d(\Delta U_{str}(\Delta))}{d\Delta} + \frac{d(\Delta U_{vdw}(\Delta))}{d\Delta} + \frac{d(\Delta Q(\Delta))}{d\Delta} \tag{3.10}$$

Therefore, for the SSC of an RVE one can write:

$$\sigma_{tot}(\varepsilon) = \sigma_{str}(\varepsilon) + \sigma_{vdw}(\varepsilon) + \sigma_{dis}(\varepsilon) \tag{3.11}$$

Thus, total stress response $\sigma_{tot}(\varepsilon)$ in quasi-static test (neglecting inertial effects) can be formally decomposed into three terms, associated with elastic deformation of CNTs ($\sigma_{str}(\varepsilon)$), formation of a new vdW surface ($\sigma_{vdw}(\varepsilon)$) and dissipation ($\sigma_{dis}(\varepsilon)$). It is important to note that neither of these terms is rate- and path-independent: the presence of rate-dependent dissipation affects the whole mechanism of the deformation, *i.e.* the balance between stretching and sliding of CNTs.

Fig. 17(A,B) presents the decomposition (3.9, 3.11) for SSC of an RVE (specimen 12 in Table 6). Fig. 17(A) gives the variations in different energy terms that appear in (3.9), and Fig. 17(B) presents the decomposition (3.11).

Initial rapid changes of the decomposition terms given in Fig. 17(B) are likely associated with dynamic effects. Omitting this initial part, we can distinguish three regions of the SSC. The first region corresponds to strains between $0.05$ and $0.3$ % and is dominated by the elastic response of individual stretched tubes. An interesting feature is that initial elastic response is negative, because, as was noticed in section 3.2.1, CNTs in a bundle are slightly compressed by vdW adhesion forces, and at the initial stage of the test they are unstrained by external tensile load. We note that almost all strain energy in our small strain simulations is associated with tension/compression term in (2.23), with less than $10\%$ associated with bending, shear and twisting terms.

The second part of the response (strains between $0.3$ and $1$ %) is characterized by the changes in all energy terms; this signifies sliding of tubes within a bundle, accompanied by formation of new vdW surface and energy dissipation. Energy dissipation occurs without releasing the elastic strain energy accumulated in individual CNTs. These two processes dominate the pre-peak shape of the SSC. The post-peak region (strains more than $1\%$) is characterized by the release of the elastic strain energy of the CNTs. To visualize sliding of CNTs in a bundle we adopt the notion of a slip vector [93], defined as

$$\vec{\delta}^{i} = -\frac{1}{\lambda_i}\sum_{j}^{\lambda_i}\left(x^{(ij)} - X^{(ij)}\right) \tag{3.12}$$

where $x^{(ij)}$ and $X^{(ij)}$ are the vector differences between the coordinates of elements $i$ and $j$ in the current and reference states, respectively, and $\lambda_i$ is the number of nearest neighbors to element $i$ in the initial reference configuration.

In the case of small deformation, the slip direction is always parallel to the axis of a CNT bundle. We are interested mostly in the slip vector magnitude, which is displayed in Fig. 17(C) at three representative strain levels for specimen 12 in Table 6. One can see the development of localization of CNT sliding region. At the stage of initiation CNTs slipping interfaces are distributed nearly evenly along the bundle, showing, however, an initiation of periodic structure reflecting periodicity of the structure of a bundle. When approaching peak stress, deformation starts localizing, and this localization develops further in a post-peak regime. The development of localization is indicated by the magnitude of a slip vector that grows faster than the nominal strain.

*3.2.4 Tensile tests - role of dissipation*

The mechanical behavior of CNT bundles depends on the rate of energy dissipation. Fig. 18(A) gives SSCs, obtained in a tensile test identical to size convergence tests described above, but without viscous damping ($\psi = 0$) and with relatively small value of local damping.

Stress-strain curves obtained in such a test demonstrate size dependence. Analysis of CNT kinematics (Fig. 18(B)) indicates that specimens immediately develop localized failure. Fig. 18(C) demonstrates the effect of local and viscous damping on deformation localization.

The figure shows the distribution of slip vector magnitude, averaged over thin slices along the length of a specimen. The localization is controlled mostly by viscous damping. On one hand, if $\psi = 0$ slip is immediately localized close to the grips.

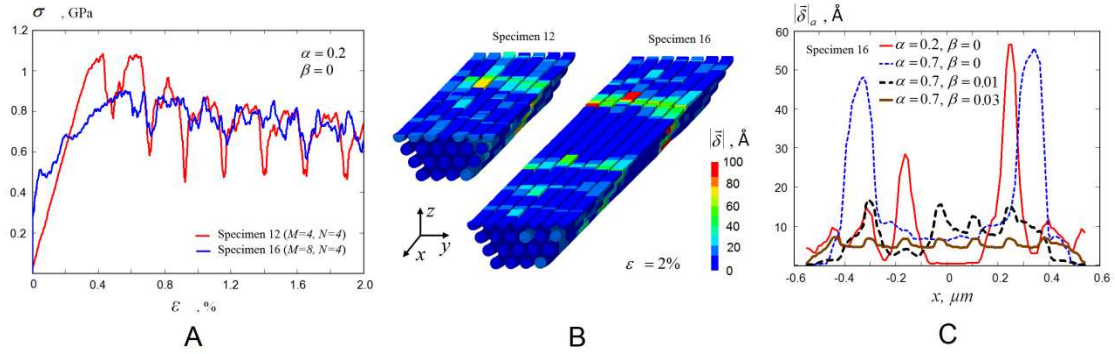


Figure 18. Low damping ( $\chi = 0.2, \quad \psi = 0.0$ ) mechanical tests on CNT bundles. (A) Stress-strain curves for specimen 12 and specimen 16 in Table 2 indicate the absence of an RVE (B) Magnitude of slip vector, visualized on a horizontal axial cross-section, indicates immediate localization of the deformation and brittle fracture of a specimen. (C) Magnitude of a slip vector, averaged over thin slices of a bundle (specimen 16) along the length for few different values of viscous and local damping.

On the other hand, $\psi = 0.03$ leads to a nearly uniform distribution of slip along the length and size-independent (material) response. As far as the localization phenomenon is controlled by the magnitude of viscous forces between CNTs, it equivalently depends on damping ratio and strain rate.

*3.2.5 Tensile tests - large strain deformation*

So far we have been considering small deformation of CNT bundles under tensile load. In this section we give a qualitative picture of a large strain deformation and breakage of a representatively large CNT bundle. Consider the specimen 2 from Table 6, subjected to a large strain test. Strain is applied at a fixed rate of $\dot{\varepsilon} = 2 \times 10^8$ $s^{-1}$ in a displacement

control mode until the specimen's breakage. Initial regime of post-peak deformation is

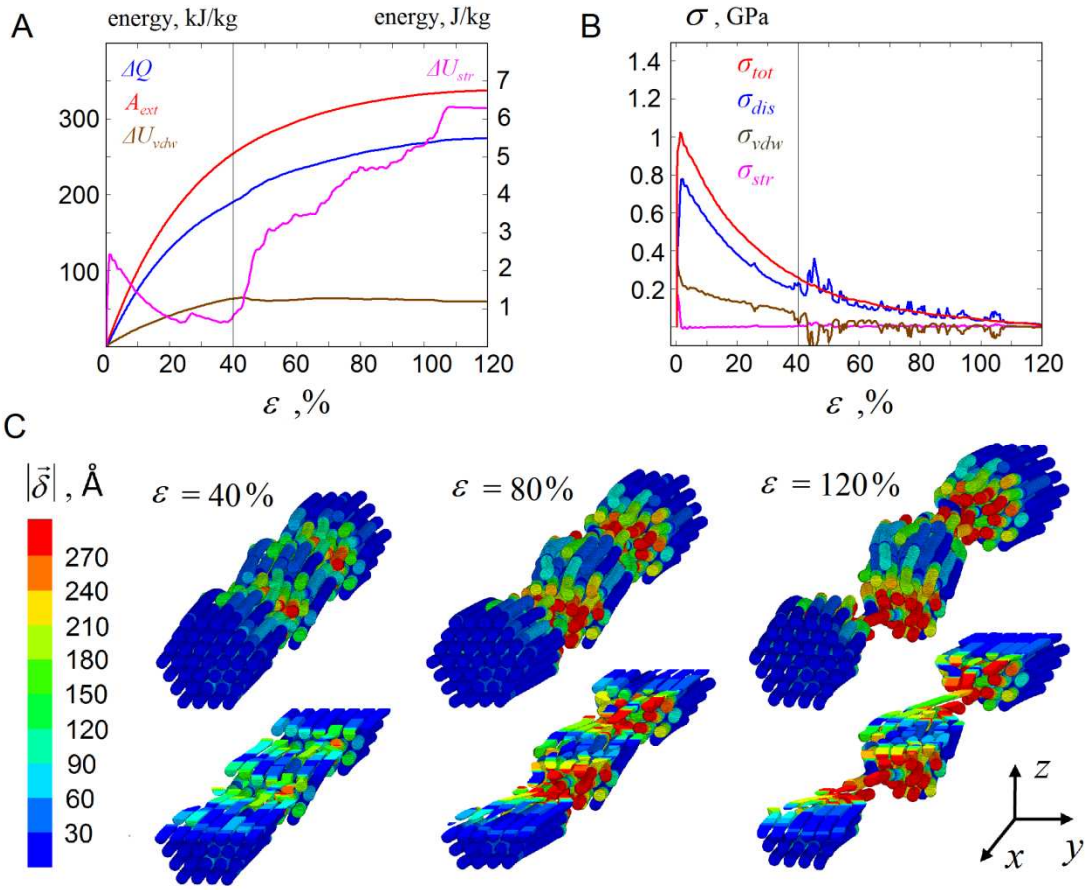


Figure 19. Large deformation of a CNT bundle. (A) Work of external force $A_{ext}$, as compared to changes in elastic strain energy $\Delta U_{str}$, vdW adhesion energy $\Delta U_{vdw}$, and dissipated energy $\Delta Q$ during the test. (B) Terms of decomposition (3.11) during the simulation. (C) CNT bundle geometry and magnitude of a slip vector, on the surface of a bundle and on a horizontal axial cross section of a bundle.

characterized by smooth sliding of CNTs along each other with slip direction parallel to an axis of the bundle. This regime of the deformation is characterized by nearly linear changes in vdW adhesion energy, and a gradual decrease in elastic energy (Fig. 19(A)).

The strain softening behavior (Fig. 19(B)) is conditioned by decrease of the averaged length and number of vdW contacts between CNTs, and corresponding decrease in viscous and potential forces, acting between CNT interfaces.

At the initial stage of post–peak deformation one can see the development of CNT sliding in periodically located slip zones presented in Fig. 19(C). They appear in certain longitudinal positions, equally spaced with period $L_{CNT}$ in the reference configuration. After the critical strain of 40% the specimen starts developing necks. Necking is characterized by the process of filling the vacancies developed in slip localization zones of a CNT crystal by local rearrangement of CNTs leading to formation of thinner close-packed regions (necks). Initiation of this process is accompanied by bending deformation of tubes, which leads to a jump in the strain energy (Fig. 19(A)). Necking is also characterized by a drop in (absolute) vdW adhesion energy and slight increase in the rate of energy dissipation (Fig. 19(A)). The decomposition (3.11) for the SSC is presented in Fig. 19(B). It appears that the elastic strain does not play any significant role in the energy balance of the breaking CNT bundle. The response is dominated by dissipative forces and vdW adhesion forces (Fig. 19(B)).

*3.2.6 Tensile tests - discussion*

The results presented in the previous sections demonstrate that in presence of significant dissipation during CNT sliding, crystalline CNT bundles exhibit nearly uniform deformation with the material mechanical response and representative SSCs. On the

other hand, without sufficient dissipation these structures develop localized slip zone at the initial stage of the deformation.

It is known that dense aligned CNT structures subjected to tensile tests in experiments [14,15] demonstrate the material mechanical response, with wide zone of plastic deformation, which is presumably associated with CNT slippage [14]. The SSCs, observed in tensile tests on fine CNT strands [15], are in good agreement with the representative SSCs obtained in our simulations. The comparison between the experiment and simulation in terms of critical strain, tensile strength and Young's modulus are presented in Table 8.

Table 8. Young's modulus $E$ , uniaxial tensile strength $\sigma_{uts}$ , and critical strain $\varepsilon_c$ , measured in experiment [15], as compared with the results of our DEM simulations.

| | $E$ , GPa | $\sigma_{uts}$ , GPa | $\varepsilon_c$ ,% |
|---|---|---|---|
| Experiment [15] | 100-150 | 0.9-1.2 | 2-3 |
| Simulation | 70-150 | 0.7-1.3 | 1-2 |

Therefore, one can suggest that forces of dissipative nature are responsible for material behavior in real aligned CNT structures [14,15]. This suggestion is supported by the results, presented in [81], where the magnitude and structure of the force acting at CNT-CNT interface in a pullout experiment were studied. It was concluded that this force is mostly conditioned by dissipation and formation of new vdW surfaces, whereas other effects, such as vdW registry, were found insignificant. The decomposition (3.11) of the

stress response observed in our RVE tensile test (Fig 4(B)), renormalized in terms of an averaged force acting at each CNT-CNT contact[2], is very close to the one presented in [81] (see Table 9). Therefore, the parameters of SSCs observed in tensile tests (Table 8), as well as the structure of the intertube forces (Table 9) demonstrate the importance of dissipation and justify the chosen calibration of viscous damping.

Table 9. Total CNT-CNT force and its decomposition into contributions from the formation of a new vdW surface, dissipation and other effects, according to experimental-numerical study [81] and our DEM simulations.

| | Total force | vdW surface | dissipation | other effects |
|---|---|---|---|---|
| Experiment [81], nN | $1.7 \pm 1.0$ | $<0.4$ | $>0.85$ | $<0.34$ |
| Simulation, nN | 1.4 | 0.35 | 0.94 | 0.11 |

Clearly, relatively high stiffness of CNTs and weak vdW adhesion determines small amount of elastic energy that can be stored in the system, which leads to the mechanical response dominated by dissipation. The more compliant bundle systems, such as collagen fibrils, with stronger adhesion (including not only vdW interaction but also hydrogen bonds) naturally store much larger amount of elastic energy "locked" by relatively strong adhesion. This leads to a negligible role of dissipation in the mechanical

[2] It was assumed that an average CNT in a bundle has 3 slipped nearest neighbors. Critical strain $\varepsilon_c$ is used to calculate stress and its terms in (3.11).

response, which allows effective mechanical modeling of such systems with simple energy-conserving bead-spring models [34]

Our results were obtained for a relatively simple model of a crystalline bundle consisting of close-packed CNTs with fixed length. The more realistic models with disordered CNTs, vacancies in the crystalline structure and random length of CNTs are expected to bring some new features, such as i) statistical effects on stiffness, strength and ductility, ii) initial densification and alignment of a bundle, with corresponding convex region of a SSC, similar to one observed in experiments [15], iii) larger size of an RVE for bundles with complex hierarchical morphologies, iv) more complex structure of elastic energy, including bending, twisting and shear terms, v) localization processes facilitated by variation in CNT length.

Presence of dissipative forces increases the strength of weakly bonded CNT structures by improving the load transfer between CNT interfaces. The bead and spring model that is widely used in mesoscopic modeling of CNT materials [34-39] provides the load transfer between CNTs due to artificial corrugation of vdW potential [30]. This property of the model leads to artifacts both in energy balance and kinematics of CNTs. In particular, it prohibits CNT sliding, rearrangements and self-assembly processes in CNT materials. CNT models based on potentials, allowing relative CNT sliding [40,47] are able to model self-assembly processes, but cannot provide sufficient load transfer between CNTs, and therefore, they are not suitable for modeling the mechanical properties of CNT materials. Our mesoscopic model, based on anisotropic vdW potential and dissipative mechanisms of load transfer between CNTs proves to be efficient in

modeling both self-assembly processes (this topic was explored in our previous work [47]) and representative mechanics of CNT structures.

### 3.3 Shear tests on crystalline assembly of CNTs

As has been demonstrated in previous sections, large CNT bundles behave as a material with the mechanical properties defined by stiffness of individual CNTs, strength of vdW adhesion between CNTs and rate of energy dissipation during CNT sliding.

However, the properties of this clearly anisotropic material with complex constitutive behavior have been studied for only one particular case of uniaxial tension. In this section we extend our discussion with consideration of another practically relevant case of a simple shear loading of a hexagonal CNT arrangement with shear load directed along the axes of CNTs.

Consider a close-packed crystal of aligned CNTs, subjected to a simple shear test (Fig. 20). The specimen consists of hexagonally arranged CNTs with distance $r_0$ between CNT axes, filling a cuboid of length $l$ , height $h$ and width $b$ (Fig. 20(A, B)). The geometry of a specimen is defined by three integer parameters: number of CNTs along the width $B$ , number of CNTs along the height $H$ (these parameters are illustrated with Fig. 7(B)) and CNT aspect ratio $D$ . Sizes of a specimen and number of CNTs in a cuboid are given by

$$h = r_0(H - 0.5), \quad b = \sqrt{3} r_0(B - 0.5), \quad l = TD, \quad N_{CNT} = 2BH \tag{3.13}$$

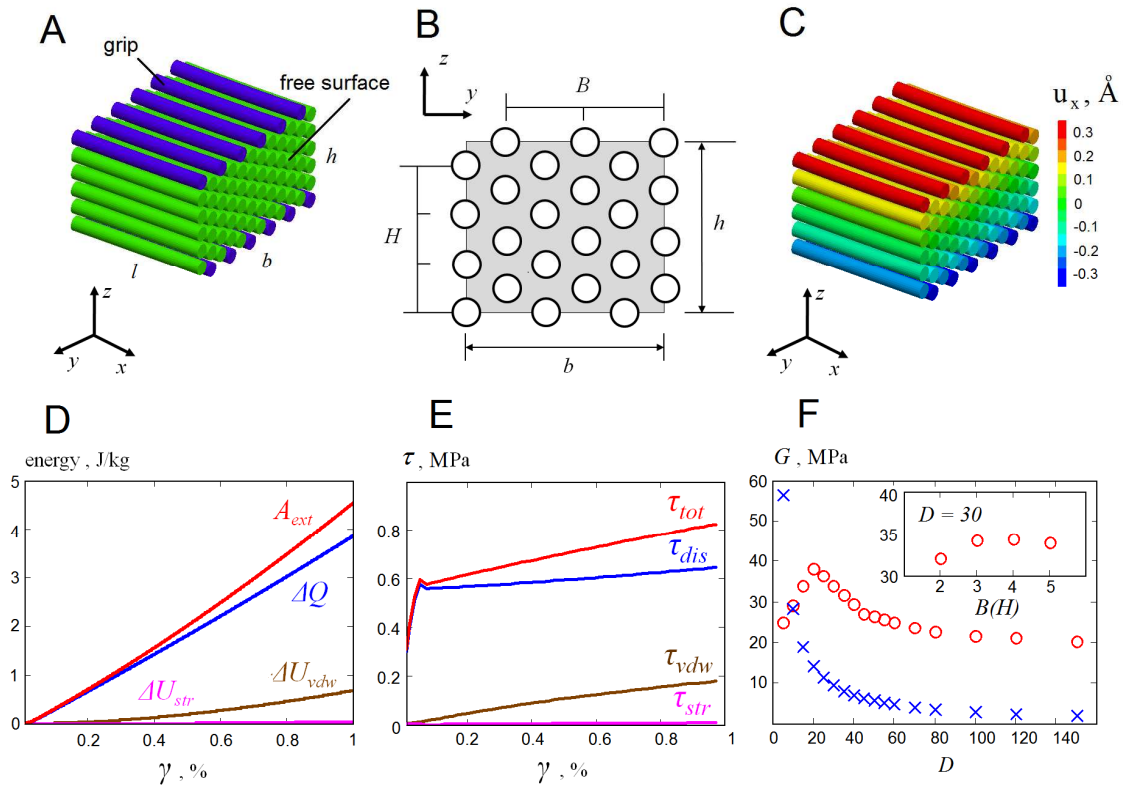


Figure 20. Shear test on a close-packed CNT assembly. (A) Problem geometry and boundary conditions. (B) Definition of the cross-sectional area of a specimen for given values of $B$ and $H$. (C) Displacement field ($x$ component of displacement) observed in a simple shear test. (D) external work as compared to potential energy terms and dissipation during the test. (E) Decomposition of stress into vdW adhesive, elastic and dissipative terms. (F) The influence of specimen length on its shear modulus. Circles are simulation results, crosses are theoretical predictions for the shear modulus due to surface tension. On the inset - the effect of cross section size ($B$ and $H$) on the shear modulus.

Periodic boundary conditions are applied along the $y$ direction. Two surfaces of the specimen parallel to the $yz$ plane are traction free. CNTs of two sides parallel to $xy$

plane are designated as grips (Fig. 20(A)). These grips are moving in a displacement control mode in opposite directions along the $x$ axis. The gradual acceleration on the first stage of the loading is followed by motion with fixed velocity, providing a constant rate simple shear loading of a crystal.

Consider the test on a specimen with $B=3,\quad H=3,\quad D=10$. The specimen is subjected to a shear strain $\gamma_{zx}=1$ % at the strain rate of $\dot{\gamma}_{zx}=2\times10^{7}$ s$^{-1}$. Nominal shear strain is defined as $\gamma_{zx}=2u_x^g/h$, where $u_x^g$ is the grip displacement. The shear stress is defined as $\tau_{zx}=F_x/bl$, $F_x$- force acting on the grip. The indexes of stress, strain (strain rate) and shear modulus are omitted below. Fig. 20(C) gives $x$ component of displacement during the test, indicating uniform shear deformation.

Similarly to the case of simple tension, one can establish the decomposition of the SSC of the specimen into vdW, elastic and dissipative terms. Fig. 20(D) gives the energy balance during the test, Fig. 20(E) - stress-strain curve and its decomposition. It appears that elastic deformations of CNTs are nearly absent, and almost all work of external force is dissipated, with small fraction stored in vdW adhesion energy. Quadratic variation of vdW energy during the test dictates linear elastic response of the specimen, with shear modulus of $G=29$ MPa.

The shear modulus of a cuboid specimen arising from the surface tension forces can be easily estimated analytically. It follows that $G=2\eta/l$, where $\eta$ is the vdW surface energy per unit area of an edge surface. The surface energy $\eta=0.026$ eV/Å$^2$ is

estimated from the simulation via splitting the specimen with formation of new vdW surface. The obtained value of surface energy yields $G = 31$ MPa.

Size convergence study of material response (Fig. 20(F)) demonstrates that the specimens demonstrate size dependence of the response that is clearly conditioned by surface tension forces. A representative response is achieved for $B = 3, \quad H = 3, \quad D = 100$. Shear modulus of representatively large specimens $G$ =18 MPa is likely conditioned by imperfect translational symmetry of vdW potential of parallel CNTs.

It is interesting to note that the crystals loaded in a direction perpendicular to CNT axes demonstrate linear elastic size-independent response with very high shear moduli of about 40 GPa, which is fully determined by the changes in vdW energy. This high shear modulus is conditioned by the interlock of CNTs in a hexagonal arrangement.

Very low values of shear modulus of CNT crystalline bundles (0.01-0.1 GPa) qualitatively agree with recent MD studies [94]. However, vdW registry features, as well as significant artificial corrugation are absent in our DEM model. Therefore we can expect that our model underestimates shear modulus and shear strength of a CNT crystalline arrangement. In order to mimic shear behavior of CNT crystals more precisely, one needs to incorporate fine features (vdW registry corrugation) into the mesoscopic vdW potential.

### 3.4 Twisting of a CNT bundle

So far we discussed the homogenized properties of representative volume elements of an arranged crystalline CNT material. In this section we consider the problem involving non-uniform deformation of a CNT assembly – CNT bundle twisting. This problem illustrates the ability of our method to deal with complex boundary value problems involving twisting of individual CNTs. Problems of twisting of CNT ropes and bundles are relevant for many applications in nanotechnology, including torsional springs in resonators [95] and rotational bearings in actuators [96]. The torsional stiffness and buckling limit of individual CNTs and small bundles were studied with MD simulations on nanometer scale [97]. It was found that the response of individual CNTs and CNT bundles are highly elastic. It was also demonstrated that the stiffness of a single carbon nanotube in a bundle is higher than that of the individual nanotube alone. This effect was attributed to stabilizing role of vdW interactions. The focus of the research [96] was on very large deformations of CNTs in a pre-buckling and buckling regime. In the following we apply our mesoscopic model to study the behavior of long and thick CNT bundles in a linear regime of torsion. Two basic examples are considered: i) twisting of a regular hexagon close-packed bundle of long CNTs, extending from one grip to another, and ii) twisting of a CNT bundle specimen, consisting of short CNTs, described in section 3.2.1. In both cases the deformation is applied in a similar way – the bundle is created, relaxed, fixed at grips and relaxed again, as was described in section 3.2.1. After that the grips are rotated in opposite directions at a given rate (after short initial acceleration), until the given relative angle of twisting is reached. Both translations and rotations of grip

elements are prescribed, providing rigid rotation of a grip as a whole. The rate of rotation is chosen slow enough to exclude dynamic effects, providing nearly uniform twist along the bundle.

Consider first the deformation of a regular hexagonal CNT bundle, in which every CNT is fixed at both grips (long CNTs bundle). The tested specimen consists of 37 close-packed CNTs with aspect ratio of 100. The test is performed at a rate of rotation $\Delta\dot{\varphi} = 0.05$ *Rad/ns*, until the relative rotation of grips $\Delta\varphi = 0.5 Rad$.

The kinematics of the deformation is presented in Fig. 21. For slow enough rate of rotation the twist is nearly uniform (Fig. 21 (A, B)). Both magnitudes of displacement vector and slip vector grow linearly with distance from the axis of rotation (Fig. 21 (B, C)). These figures indicate that the deformation of a twisted bundle approximately follows the deformation of an isotropic elastic twisted rod.

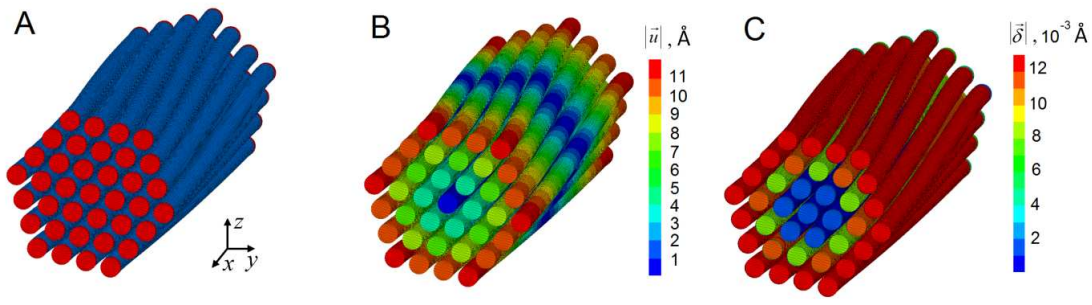


Fig. 21: (A) Twisted CNT bundle, long CNTs (free elements in blue, grip elements in red). (B, C) Color maps presenting the magnitude of displacements (B) and the magnitude of slip vector (C).

The prescribed twisting deformation induces torques acting on the grips. The magnitude of the torque is given as

$$M = M_I + M_{II} = \left|\sum (M_i)_x\right| + \left|\sum (\vec{r}_i \times \vec{F}_i)_x\right| \tag{3.14}$$

where $(M_i)_x$ are $x$ projections of moments acting on $i$-th grip element, and $(\vec{r}_i \times \vec{F}_i)_x$ are $x$ projections of moments created by forces $\vec{F}_i$, acting on $i$-th grip element, positioned at the point $\vec{r}_i$ relative to the center of a grip. Fig. 22 (A) gives the ratio between these two components during the test. As can be seen, the torque response is dominated by moments, acting at each individual element of a grip, clearly associated with torque response of individual CNTs to twisting.

Re-writing expressions (3.9, 3.11) for the case of twisting deformation, one can study the energy balance during the deformation and analyze the structure of the torque response. The work done by external moment can be written as:

$$A_{ext}(\Delta\varphi) = \int_0^{\Delta\varphi} M(\Delta\varphi')d\Delta\varphi' = \Delta U_{str}(\Delta\varphi) + \Delta U_{vdw}(\Delta\varphi) + \Delta Q(\Delta\varphi)$$
$$\Delta U_{str}(\Delta\varphi) = \Delta U_{ten}(\Delta\varphi) + \Delta U_{ben}(\Delta\varphi) + \Delta U_{she}(\Delta\varphi) + \Delta U_{twi}(\Delta\varphi) \tag{3.15-3.16}$$

The right hand side of the expression (3.15) gives the decomposition of the total change in strain energy into changes in strain energy due to tension, bending, twisting and torsion of CNTs. Formal differentiation gives the decomposition of the total torque

response into moments due to energy dissipation, and variations in different forms of the potential energy.

$$M(\Delta\varphi)=\frac{d(\Delta U_{ten}(\Delta\varphi))}{\Delta\varphi}+\frac{d(\Delta U_{ben}(\Delta\varphi))}{\Delta\varphi}+\frac{d(\Delta U_{she}(\Delta\varphi))}{\Delta\varphi}+\frac{d(\Delta U_{twi}(\Delta\varphi))}{\Delta\varphi}+\frac{d(\Delta U_{vdw}(\Delta\varphi))}{\Delta\varphi}+\frac{d(\Delta Q(\Delta\varphi))}{\Delta\varphi}= \\ M_{ten}(\Delta\varphi)+M_{ben}(\Delta\varphi)+M_{she}(\Delta\varphi)+M_{twi}(\Delta\varphi)+M_{vdw}(\Delta\varphi)+M_{dis}(\Delta\varphi) \tag{3.17}$$

Fig. 22 (B, C) present the structure of the response. Consistently with Fig. 22 (A) it appears that almost all work (93.3%) done by external forces is converted in twisting energy of individual CNTs; the remaining energy is distributed between vdW adhesion (4.1%), bending (1.4%), heating dissipation (0.7%), tension (0.4%) and shearing (0.1%) . This result agrees qualitatively with [96].

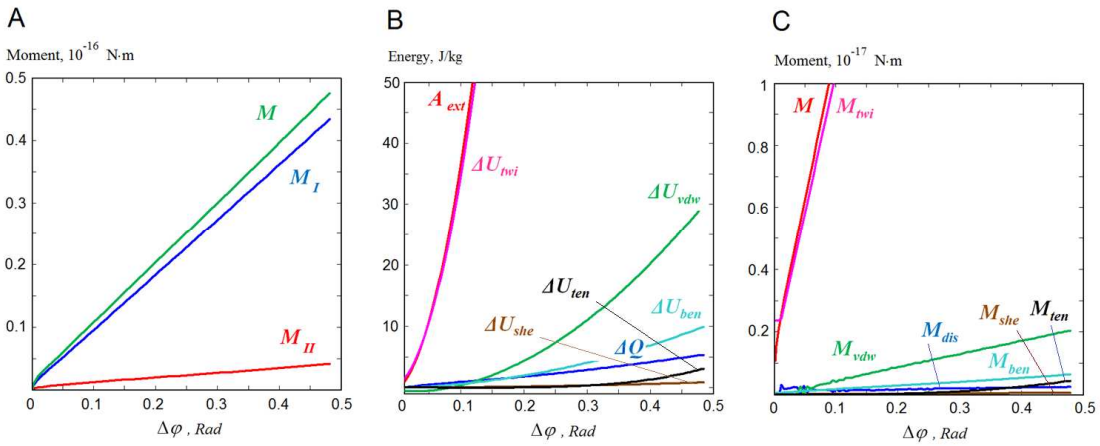


Figure. 22: Twisting of a CNT bundle, long CNTs. (A) Decomposition (3.14) for the moment acting on the grip, (B) Energy decomposition (3.15-3.16), (C) Decomposition (3.17) for the moment acting on a grip.

Fig. 22 gives torsional stiffness of a crystal of $10^{-16}$ N×m. This corresponds to a torsional stiffness of an isotropic elastic cylindrical rod with radius $r = 3r_0$ and shear modulus G= 12.3 GPa.

Consider now the case of composite CNT crystal consisting of CNTs that are shorter than the distance between the grips (specimen # 1 in Table 6). In this case CNTs have kinematical possibility to relax individual twisting deformation. During the test the CNT segments show translations nearly identical to ones presented in Fig. 21.

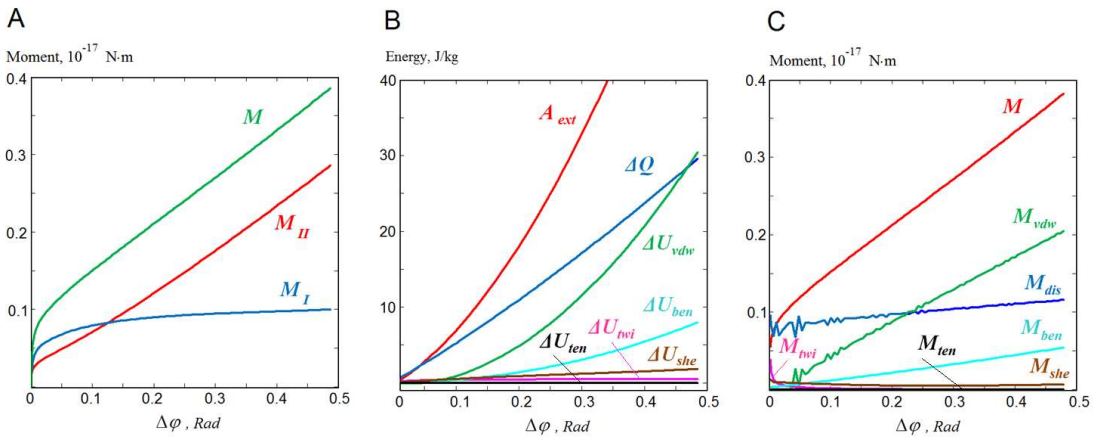


Fig. 23: Twisting of a CNT bundle, short CNTs. (A) Decomposition (9) for the moment acting on the grip, (B) Energy decomposition (10.1-10.2), (C) Decomposition (11) for the moment acting on a grip.

However, the dynamics and energy balance give a picture that is significantly different from the one obtained for long CNTs specimen. The decomposition (3.14) (Fig. 23, (A)) demonstrates that the torque acting on a grip is mostly created by forces acting at grip elements. This indicates absence of twisting deformation of CNTs. This observation is

justified by decompositions (3.15-3.17). Energy balance is characterized by the distribution of work done by external forces between vdW adhesion energy, bending energy of CNTs and heat. The moment decomposition (3.17) demonstrated that the observed feedback is mostly driven by changes in vdW adhesion energy. It worth noting here that the changes in vdW adhesion energy for long CNT specimen (Fig. 22) and short CNT specimen (Fig. 23) are caused by different mechanisms. In first case the energy is increasing solely due to decrease of separation distance. In the second case, the vdW adhesion energy is increasing mostly due to CNT slippage, causing formation of the new vdW surface.

Fig. 23 (C) also clearly indicates immediate relaxation of twisting deformation. This phenomenon is an artifact of our model of mesoscopic vdW interaction that does not provide any potential barriers to relative axial rotation of two parallel CNT segments. Atomic level consideration indicates the existence of such barriers. Therefore, one can suggest the significance of the vdW cohesion between CNTs in storing twisting deformation and the existence of critical length of vdW contact needed to build up to store twisting deformation of individual CNTs in a twisted bundle. These questions are beyond the framework of this section.

A torsional stiffness of a crystal, estimated from Fig. 23, gives the value of $0.6\times10^{-17}\ \mathrm{N\times m}$, 17 times more compliant that the long CNTs specimen. Corresponding shear modulus of an isotropic elastic cylindrical rod with radius $r = 3r_0$ is $G = 0.74\ \mathrm{GPa}$. This value is significantly larger than one obtained in simple shear test , considered in section 3.3,

which is explained by much higher rate of formation of a new vdW surface in torsion experiment.

It is clear that the role of bending term in energy balance depends on the average curvature of CNTs in a bundle. It will be significant for highly twisted thin CNT bundles and negligible for thick CNT ropes, subjected to moderate twists. In the latter case the feedback is caused by energy dissipation and changes in vdW adhesion energy, similar to simple shear experiment given in section 3.2.7.

## 3.5 Mechanics of cross-linked CNT bundles

One of the ultimate goals of CNT material design is to utilize the molecular strength of CNT in macroscopic structures and materials. As we demonstrated in two previous sections, CNT bundles in which CNTs are weakly bonded by vdW interactions are not suitable for this purpose – weak shear interactions between CNTs lead to CNT slippage and failure at the critical stress on the order of $1$ GPa, which is inferior not only to individual CNTs, but also all types of conventional carbon fibers [98]. The most promising approach to overcome this problem is chemical cross-linking [99].

### *3.5.1 Modeling cross-linked CNTs within a DEM framework*

Different strategies and approaches are used to cross-link CNTs with chemical bonds to prohibit CNT sliding and improve the mechanics of CNT materials [99]. In this work we will consider the behavior of short covalent links, *e.g.* ones formed by introducing interstitial C atoms that form covalent bonds with C atoms belonging two CNT surfaces [100]. This kind of bonds, formed as a result of irradiation of CNTs with high-energy

particles, has been observed experimentally [101,102]. The interstitial atoms form different bond configurations with varying effective strengths and stiffnesses. From the mechanical point of view a cross-link molecule can be viewed as a breakable spring with significant normal stiffness, but negligible shear, bending and torsional stiffnesses.

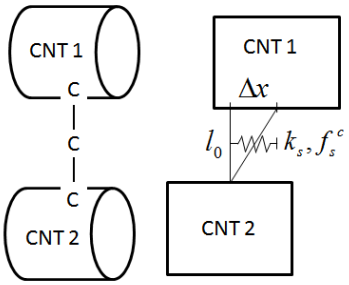


Fig 24. Schematic representation of a cross-link in a DEM model

Consider a simple mechanical model for a cross-link molecule that is used in our simulations. The model is based on the formalism of a contact bond [63], which can be viewed as a particular case of parallel bond with vanishingly small interface area, moment of inertia and polar moment of inertia. This kind of bond resists to normal and shear displacements of bonded segments while it's bending and torsional stiffnesses are zero. In our model these bonds are formed between face-to-face CNT segments. Considering that kinematic of the problem resolves only sliding of CNTs which cause shear relative motion of bonded face-to-face segments, the shear stiffness of the bond is calibrated to represent the elasticity of a cross-link (Fig. 24)

The strength and stiffness of the bonds in our model are chosen in a phenomenological way. The bond strength and stiffness are characterized by dimensionless parameters $\alpha_c$ and $\beta_c$, which give ratios of the strength and stiffness of the bond to the strength and stiffness of a reference bond formed by the interstitial C atom with two CNT surface atoms via two single covalent bonds (Fig. 24).

An initial calibration of the stiffness and strength of a reference bond is based on the effective radial potential for a single covalent bond. Based on two-body potential energy term of conventional potentials describing bonding in carbon [27, 28], it is assumed that the cross-link can sustain strain $e_c = 0.5$ before break. We also assume the linear spring–like behavior of the bond. Although the length of two single covalent bonds is somewhat shorter than the equilibrium vdW separation ($3.08$ Å vs $3.35$ Å), for simplicity we assume that the bond is formed as unstrained, *i.e.* bond length $l_0 = 3.35$ Å. As described above, the elastic behavior of a cross-link is represented with shear force-displacement law of a contact bond (Fig. 24). The critical elongation of the shear spring is found as

$$\Delta x = \sqrt{(1+e_c)^2 l_0^{\,2} - l_0^{\,2}} = 3.75 \text{ Å} \tag{3.18}$$

The contact bond shear stiffness is found by equating the strain energy of the spring with the energy of two single covalent bonds $2E_c$ ($E_c = 3.6$ eV)

$$\frac{k_s \Delta x^2}{2} = 2E_c \Rightarrow k_s = \frac{4E_c}{\Delta x^2} = 1.02 \text{ eV/ Å}^2 \tag{3.19}$$

Strength of the spring is found as:

$$f_c = k_s \Delta x = 1.02 \cdot 3.75 = 3.82 \text{ eV/ Å} \tag{3.20}$$

The bonds are randomly populated between neighboring CNTs until reaching the prescribed number of cross-links $N_c$. The bond is introduced by the replacement of a near-neighbor face-to-face vdW contact with the contact bond force-displacement law. The number of near-neighbor face-to-face vdW contacts between distinct elements is given as:

$$N_{vdw} = MP\left[3 + 9(\mathrm{N}-1)^2\right] \tag{3.21}$$

The density of cross-links in a specimen is characterized by the parameter $\gamma_c = N_c / N_{vdw}$.

*3.5.2 Parametric study of the mechanics of cross-linked fibers*

Consider now the results of mechanical tests performed on CNT bundle specimens, as described above. Fig. 25 and Table 10 summarize our parametric studies for SSCs of CNT bundles. SSCs of random realizations of specimens vary significantly (Fig. 25 (A)), therefore each test result presented in Table 10 and Fig. 25 (B-H) is an average of four independent realizations. All the tests were carried out in a displacement control mode at $\dot{\varepsilon} = 10^8 \text{s}^{-1}$.

Each SSC starts with linear regime of loading (characterized by the Young's modulus $E$ ), followed by specimen breakage that occurs at certain peak value of stress $\sigma_{uts}$ and

corresponding strain $\varepsilon_c$. The values of $E$, $\sigma_{uts}$ and $\varepsilon_c$ are presented in Table 10 for each test.

As we can see from Table 10, the observed elastic moduli are always less than $E_0 = 385$ GPa, defined by the expression (3.8), because compliance of bonds allows certain relative slip of CNTs.

Tests 1-12 (Fig. 25 (B-D)) present the dependence of stress-strain curves on the cross-links strength $\alpha_c$, stiffness $\beta_c$ and density $\gamma_c$. Expectedly, the Young's modulus of a bundle $E$ depends on $\beta_c$ and $\gamma_c$ but is insensitive to $\alpha_c$. High tensile strength $\sigma_{uts}$ and critical strain $\varepsilon_c$ is facilitated by strong, densely populated and compliant cross-links. Another immediate observation is that the specimens with strong, stiff and densely populated bonds facilitate brittle response, whereas specimens with low cross–link density, weak and compliant bonds demonstrate ductile failure.

Tests 13-22 give a size convergence study for SSCs. It appears that in the pre-peak regime SSCs are insensitive to the length of the specimen; therefore even relatively small ones $M \geq 3$ can be viewed as representative volume elements (RVEs). Convergence of SSCs with increasing thickness is similar to that observed in Fig. 16 for CNT bundles without cross-links. Specimens with thickness factor of $N \geq 5$ can be viewed as RVEs.

Tests 23-25 give the dependence of SSCs on the aspect ratio of CNTs that constitute a bundle. It appears that increasing the aspect ratio of CNTs increases Young's modulus

of a bundle $E$ its strength $\sigma_{uts}$ and critical strain $\varepsilon_c$, while the post peak behavior remains relatively ductile.

Tests 26, 27 demonstrate that the energy dissipation does not play significant role in stress-strain response, showing nearly the same response for absent viscous dissipation ($\psi = 0$) and nominal level of dissipation ($\psi = 0.03$).

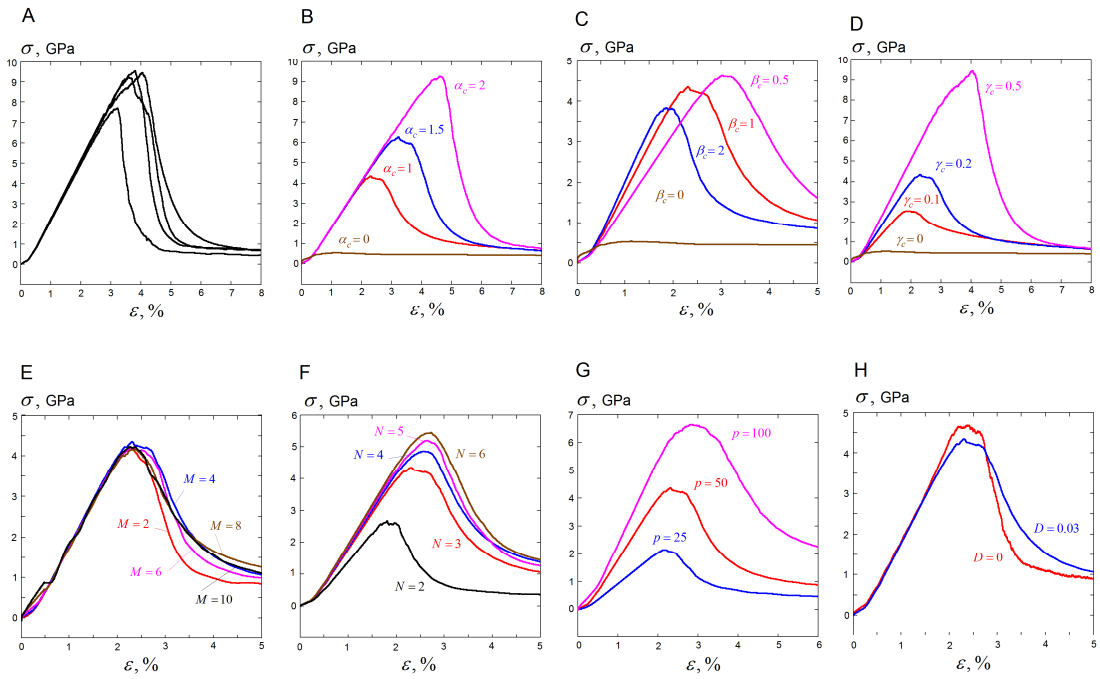


Figure 25. Parametric studies of SSCs. (A) Four independent realizations (Test #12) demonstrating the scatter of SSCs. (B) Dependence on bond strength $\alpha_c$ (tests 1-4 in Table 10). (C) Dependence on bond stiffness $\beta_c$ (tests 5-8 in Table 10). (D) Dependence on cross-link density $\gamma_c$ (tests 9-12 in Table 10). (E) Dependence on length factor $M$ (tests 13-17 in Table 10). (F) Dependence on thickness factor $N$ (tests 18-22 in Table 10). (G) Dependence on CNT aspect ratio $p$ (tests 23-25 in Table 10). (H) Dependence on damping ratio $\psi$ (tests 26, 27 in Table 10).

Table 10. Parametric study of the mechanics of cross-linked fibers. Each line represents an average over 4 random realizations.

| # | $\alpha_c$ | $\beta_c$ | $\gamma_c$ | $M$ | $N$ | $p$ | $\psi$ | $E$ | $\varepsilon_c$ | $\sigma_{uts}$ |
|---|---|---|---|---|---|---|---|---|---|---|
| Dependence on cross-link strength $\alpha_c$ | | | | | | | | | | |
| 1 | 0 | 1 | 0.2 | 4 | 3 | 50 | 0.03 | 49.29 | 1.116 | 0.537 |
| 2 | 1 | | | | | | | 169.26 | 2.293 | 4.349 |
| 3 | 1.5 | | | | | | | 169.20 | 3.227 | 6.267 |
| 4 | 2 | | | | | | | 171.21 | 4.603 | 9.239 |
| Dependence on cross-link stiffness $\beta_c$ | | | | | | | | | | |
| 5 | 1 | 0 | 0.2 | 4 | 3 | 50 | 0.03 | 49.29 | 1.116 | 0.537 |
| 6 | | 0.5 | | | | | | 137.22 | 3.014 | 4.634 |
| 7 | | 1 | | | | | | 169.26 | 2.293 | 4.349 |
| 8 | | 2 | | | | | | 192.22 | 1.846 | 3.832 |
| Dependence on cross-link density $\gamma_c$ | | | | | | | | | | |
| 9 | 1 | 1 | 0.0 | 4 | 3 | 50 | 0.03 | 49.29 | 1.116 | 0.537 |
| 10 | | | 0.1 | | | | | 129.48 | 1.836 | 2.552 |
| 11 | | | 0.2 | | | | | 169.26 | 2.293 | 4.349 |
| 12 | | | 0.5 | | | | | 210.80 | 4.029 | 9.452 |
| Dependence on length factor $M$ | | | | | | | | | | |
| 13 | 1 | 1 | 0.2 | 2 | 3 | 50 | 0.03 | 171.82 | 2.242 | 4.203 |
| 14 | | | | 4 | | | | 169.26 | 2.293 | 4.349 |
| 15 | | | | 6 | | | | 162.98 | 2.332 | 4.201 |
| 16 | | | | 8 | | | | 155.76 | 2.372 | 4.166 |
| 17 | | | | 10 | | | | 156.04 | 2.352 | 4.231 |
| Dependence on thickness factor $N$ | | | | | | | | | | |
| 18 | 1 | 1 | 0.2 | 4 | 2 | 50 | 0.03 | 130.33 | 1.801 | 2.680 |
| 19 | | | | | 3 | | | 169.26 | 2.293 | 4.349 |
| 20 | | | | | 4 | | | 175.85 | 2.549 | 4.865 |
| 21 | | | | | 5 | | | 180.85 | 2.641 | 5.202 |
| 22 | | | | | 6 | | | 185.33 | 2.713 | 5.442 |
| Dependence on CNT aspect ratio $p$ | | | | | | | | | | |
| 23 | 1 | 1 | 0.2 | 4 | 3 | 25 | 0.03 | 88.97 | 2.135 | 2.147 |
| 24 | | | | | | 50 | | 169.26 | 2.293 | 4.349 |
| 25 | | | | | | 100 | | 212.05 | 2.827 | 6.632 |
| Dependence on damping ratio $\psi$ | | | | | | | | | | |
| 26 | 1 | 1 | 0.2 | 4 | 3 | 50 | 0.00 | 171.39 | 2.371 | 4.695 |

| | | | | | | | | | | |
|---|---|---|---|---|---|---|---|---|---|---|
| 27 | | | | | | | 0.03 | 169.26 | 2.293 | 4.349 |

*3.5.3 Energy balance and kinematics.*

The evolution of potential energy terms and kinematics of a specimen tested with the parameters corresponding to test #2 is shown in Table 10. Figure 26(A) visualizes relative slip of CNTs within a bundle. It is clearly seen that the massive and localized slip occurs at the damage zone in a post-peak regime of the deformation. Fig. 26(B) illustrates what the slip localization of conditioned by localized failure of cross-links that start breaking slightly before reaching peak stress.

Fig. 26(C) presents the energy balance during the simulation. The energy balance during displacement control quasi-static tension test is given by

$$A_{ext}(\Delta) = \int_0^{\Delta} F_{ext}(\Delta')d\Delta' = \Delta U_{str}(\Delta) + \Delta U_{bonds}(\Delta) + \Delta U_{vdw}(\Delta) + \Delta Q(\Delta) \quad (3.22)$$

Here $\Delta U_{bonds}(\Delta)$ is the energy stored in the cross-links, other terms correspond to (3.9)

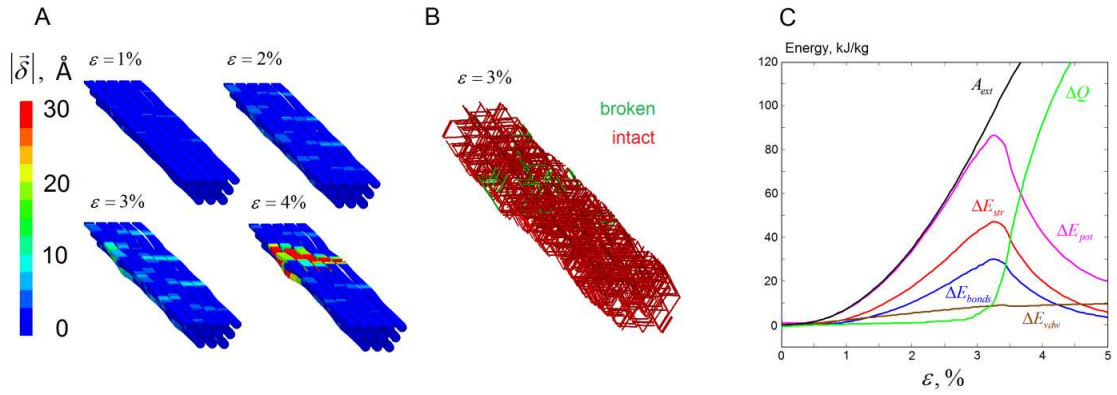


Figure 26. (A) Slip vector magnitude snapshots at four strain levels. (B) Visualization of broken and intact cross-links for 3% strain. (C) Energy balance (8) during the test #2 in Table 10.

It appears that in pre-peak regime deformation of the specimen almost fully elastic. The total strain energy is stored in the energy of elastic deformation of individual CNTs and the strain energy of cross-links, with small fraction stored in vdW adhesion energy. Post peak deformation is associated with massive energy dissipation. Accepting the value of CNT heat capacity $710\ \mathrm{J/(kg \cdot K)}$, we conclude that the dissipation of all stored potential energy leads to increase of bundle temperature on $120\ \mathrm{K}$.

*3.5.4 Mechanics of cross-linked CNT bundles – discussion*

As we could see from the previous section, cross-linked CNT bundles can achieve extremely high values of Young's moduli and strength, approaching those dictated by the stiffness and strength of individual CNTs. This result agrees with previous work on full molecular dynamic simulation of CNT fibers [100].

The results of the parametric study presented in the previous section suggest strategies for improving mechanical properties of cross-linked CNT fibers. The Young's modulus of

CNT bundles can be increased by populating stiff bonds with high density over long intertube contacts. High tensile strength $\sigma_{uts}$ and critical strain $\varepsilon_c$ can be achieved by improving bond strength, length of CNTs in a bundle and density of cross-links. Interestingly, certain improvement of these parameters is facilitated by more compliant bonds (Fig. 25(C)). The latter observation can be explained with the fact that compliant cross-links resolve significant relative slip of CNTs within the bundle, which leads to formation of new vdW surface and participation of vdW surface tension forces in the response.

The bundles without cross-links demonstrated significant dependence of SSC on the length of a bundle. Those effects were associated with inhomogeneous distribution of slip of CNTs within a bundle (Fig. 18 (C)). CNTs in cross-linked bundles exhibit negligible amount of slip in pre-peak regime of deformation, and therefore the effect of specimen length onto SSC is negligible.

The effect of specimen thickness is conditioned by changing the ratio between the number of “surface” CNTs $N_s$, having 2-3 neighbors, and “volume” CNTs $N_v$, having $6$ neighbors in a bundle. “Volume” CNTs play the dominant role in load transfer, and therefore the response becomes representative when $N_s / N_v << 1$, i.e. $N \geq 5$.

In contrast with volatile CNT bundles, the sliding dissipation appears to be insignificant in cross-linked systems. Fig. 26(C) demonstrates that the role of energy dissipation is negligible in pre-peak regime.

### 3.6 Self-assembly and mechanics of CNT films

Previous sections addressed the mechanics of one-dimensional CNT assemblies. Those structures are particularly interesting object for mesoscopic modeling, because DEM methodology allows studying collections of CNTs of representative sizes. Modeling two-dimensional CNT structures remains a lot more challenging topic due to computational limitations that do not allow studying large ensembles of representatively large CNT collections. However, our current modeling capabilities allowed us to obtain numerous interesting results related to self-assembly and mechanics of CNT structures.

#### *3.6.1 Self-assembly of CNTs into a network of bundles*

The phenomenon of CNT self-assembly is well known and is directly observed in experiment [9, 10]. It is known that the CNT paper obtained by filtering CNT suspension tends to form complex morphologies that can be described as entangled networks of bundles. CNTs within each bundle form hexagonal close-packed structure. In our work [47] we presented the approach allowing to study self-assembled CNT structures.

Consider the procedure of self-assembly of a free standing CNT film (Fig. 27). In this particular example $800$ $(10,10)$ CNTs with length $L_{CNT} = 0.3\ \mu\mathrm{m}$ (aspect ratio of $220$) are deposited onto $H \times H$ square, $H = 0.6\ \mu\mathrm{m}$. Periodic boundary conditions are applied in in-plane ($xy$) directions. The final configuration of a CNT film specimen after $8\times10^4$ time steps ($2.4$ ns) of relaxation is given in Fig. 27(A). CNTs are deposited in $xy$ plane without initial separation in out-of-plane ($z$) direction. Considering very large persistence lengths of CNTs ($86\ \mu\mathrm{m}$ for $(10,10)$ CNTs, see section 2.1) we do not presume thermal-induced

bending and self-folding, CNTs are deposited as initially straight. On the first stage of self-assembly process CNTs separate in $z$-dimension due to repulsive forces, associated with vdW potential, forming a certain distribution in $z$-direction. The thickness of an assembly of $N$ distinct elements with $z$ (out of plane) position $z_i$ is defined as follows:

$$h_f = \sqrt{12} s_z, \quad s_z = \sqrt{\frac{1}{N}\sum_{i=1}^{N}(z - z_0)^2}, \quad z_0 = \frac{1}{N}\sum_{i=1}^{N} z_i . \tag{3.23}$$

This definition implies uniform distribution of elements in $z$ direction. We also define porosity of the specimen $\varphi$. Our definition is based on the assumption that equilibrated bundle consisting of parallel identical tubes with hexagonal packing has zero porosity:

$$\varphi = \frac{1}{V_0}\left(V_0 - N V_s\right), \quad V_0 = H^2 h_f, \quad V_s = \frac{3\sqrt{3}}{4} r_0^2 T. \tag{3.24}$$

Here $V_0$ is a volume occupied by a specimen, $V_s$ is a volume occupied by a CNT segment in a hexagonal bundle.

On the second stage of self-assembly process, CNTs are bent by vdW adhesion forces, reaching certain equilibrium state. Self-assembly process is carried out without viscous forces, in order to reach equilibrium in a reasonable computational time. Equilibrated configuration (Fig. 27(A)) is characterized by the balance between adhesive energy and elastic strain energy (Fig. 27(B)), somewhat similar to CNT ring example, considered in section 3.1.

Fig. 27(C) gives equilibrium thickness and porosity of a CNT film. The equilibrium thickness of $11.3$ Å and porosity of $77\%$ are reached in $2$ ns. Fig 27(D) gives the evolution

of the components of elastic energy terms. It appears that the strain energy of an equilibrated CNT film is dominated by bending energy.

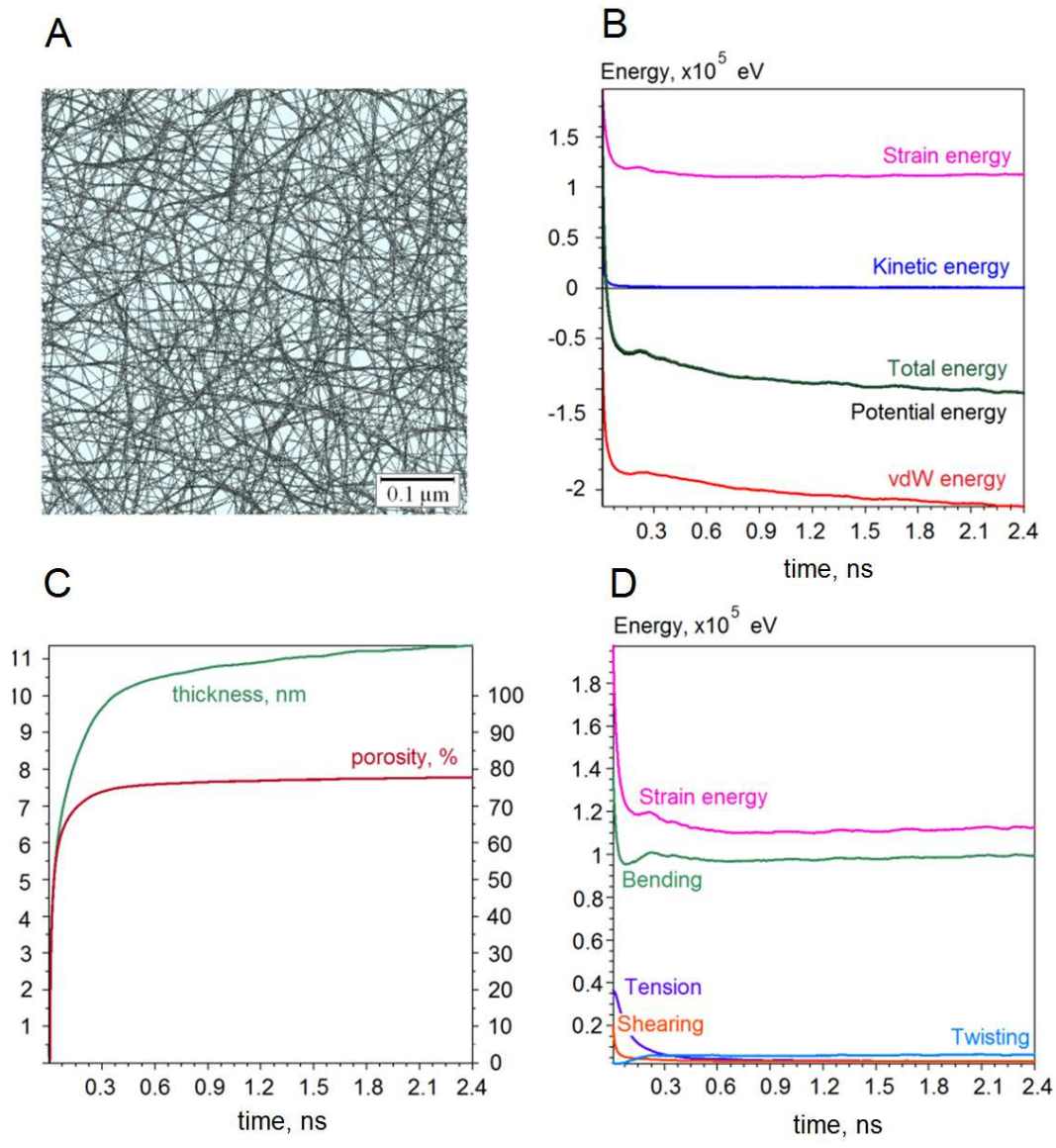


Figure 27. Relaxation of a CNT film specimen. (A) Structure of a self-assembled CNT film. (B) Evolution of kinetic, potential and total energy of the film during the relaxation. (C) Thickness and porosity of the film during the relaxation. (D) Evolution of different terms of elastic energy.

*3.6.2 Statistical properties of a CNT film morphology*

The equilibrated CNT film has certain morphology that weakly depends on further equilibration. It can be characterized by levels of elastic energy and vdW adhesion energy, by the distributions of number of nearest neighbors $\phi_N(N)$ and slip vector magnitude $\phi_\delta(|\vec{\delta}|)$ for CNT segments, distribution of curvature radii $\phi_r(r)$ (strain $\phi_\varepsilon(\varepsilon)$) of CNTs.

Consider a set of 4 CNT film specimens, assembled in a way described in the previous section. Fig. 28(A) gives the distribution of the magnitude of slip vector that indicated the amount of relative slip during the relaxation. It appears that just like in case of CNT ring the relaxation process is closely related to relative slip of CNTs. Therefore, simple bead and spring models [34-39] that prohibit relative slip cannot be used to model representative structure of a representative CNT material. Fig 28(B) gives the distribution for the number of nearest neighbors of a CNT segment. We can clearly identify peaks associated with isolated CNTs (2 neighbors), bundles of 2 CNTs (5 nearest neighbors) etc. The distributions given in Fig. 28(A) and Fig. 28(B) are given for three different sample sizes - $0.6\times0.6\ \mu m$, $0.3\times0.3\ \mu m$, $0.15\times0.15\ \mu m$ It appears that the smallest sample ( $H / L_{CNT} = 0.5$ ) is already representative in terms of distributions $\phi_\delta(|\vec{\delta}|)$ and $\phi_N(N)$ .

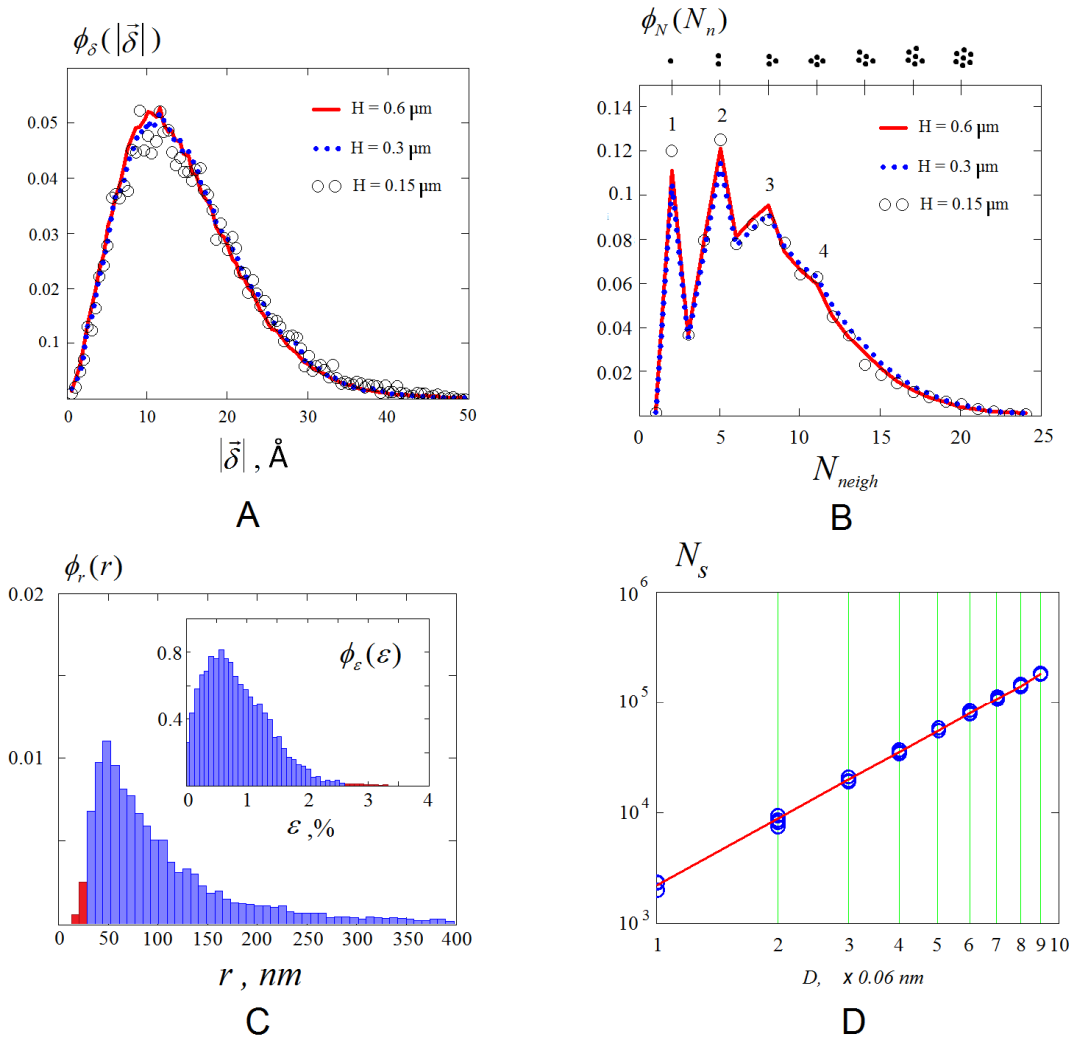


Fig. 28. Statistical properties of the CNT film morphology. (A) Distribution of the slip vector magnitude after 0.8 *ns* of self-assembly and (B) distribution of the number of element's nearest neighbors in a self-assembled structure for three samples of the specimen of different sizes. (C) Distributions of local radius of curvature (maximum local strain). Red bars indicate CNTs that approach nonlinear elastic regime of deformation. (D) Number of elements in a square sample of a CNT film $N_s$ as the function of its side $D$.

Figure 28 (C) gives distributions of curvature radii $\phi_r(r)$ and strain $\phi_\varepsilon(\varepsilon)$ of CNTs in a self-assembled structure. An important question arising here is if a self-assembled structure develops nonlinear regimes of bending. Accepting the critical curvature radius for $(10, 10)$ CNTs $r_c = 25$ nm [44] ($\varepsilon_c = 2.7\%$), we can see that less than $1\%$ of CNTs in a self-assembled CNT film approach critical (bucking) radii of curvature. This means linear model (2.20) employed in our simulations is sufficient for quantitatively correct analysis of CNT morphologies.

Size effects of mechanical responses of nanostructured materials often conditioned by their fractal morphology (e.g. [103,104]). In this context it is interesting to know if the structure presented in Fig 28(A) has features of a fractal domain. One of the fundamental property of fractal domain is size dependence of its density. In other words, if the hierarchical structure on Fig. 28(A) displays properties of a fractal domain, the number of distinct elements in a specimen characterized by a size $H$ is scaled as $H^a$, where $a < 2$. The analysis of the number of distinct element $N_s$ as a function of a sample size (Fig. 28(D)) demonstrates that the number of distinct elements in a square sample $H \times H$ scales precisely as a second power of $H$. This means the structure presented in Fig 28(A) does not demonstrate fractal features on the micrometer scale.

Real CNT self-assembly processes involve sliding dissipation, vdW registry effects, Brownian motion, influence of substrate etc. However, our simple model predicts realistic structure of CNT film, consistent with scanning electron microscopy observations (Fig. 29).

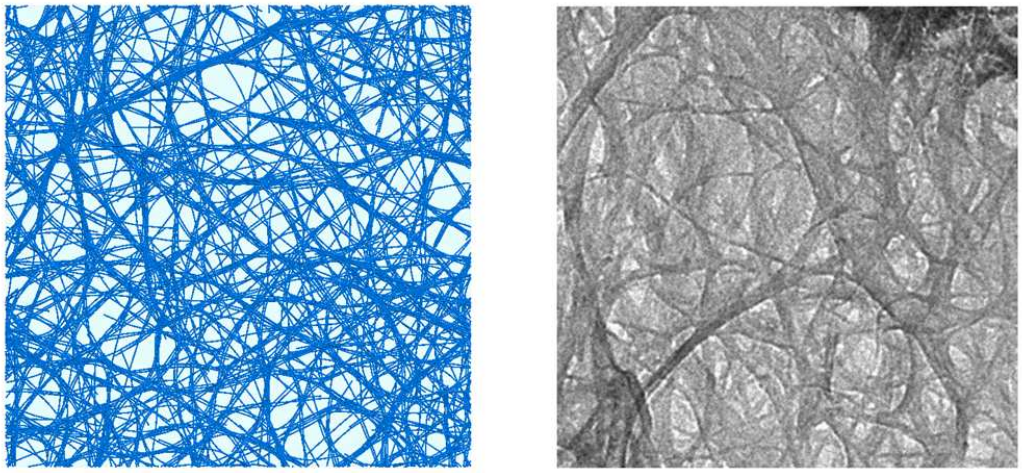


Figure 29. Comparison of the structure of a CNT film observed in (A) DEM simulation and (B) and SEM microscopy ( Image courtesy E. Hobbie). The size of both samples $0.4\times0.4\,\mu\mathrm{m}$, length of CNTs, thickness and porosity are comparable.

*3.6.3 Mechanical response of CNT films*

As we mentioned above, computational limitations do not allow us to present rigorous Monte-Carlo simulations of the mechanics of CNT films, as well as detailed parametric studies. In this section we outline the most important features of the CNT film mechanical response observed in DEM simulations.

Consider the mechanical test on a CNT film specimens described in a previous section, which is schematically shown in Fig. 30. A square specimen is subjected to a displacement controlled confined tension test. The boundary conditions are presented in Fig. 30(A) Square CNT film specimen is separated onto a gage (free elements) and grip

elements (constraints applied). The thickness of a grip is 15 Å, or approximately one distinct element. The elements of grip 1 and grip 2 are moving in opposite directions with the prescribed motion law in $x$ direction (no constraints applied on motion of the elements in $x$ and $y$ directions). Grip 3 and grip 4 constrain the motion of elements in $y$ direction. Both constraints are imposed on corner elements belonging to two grips.

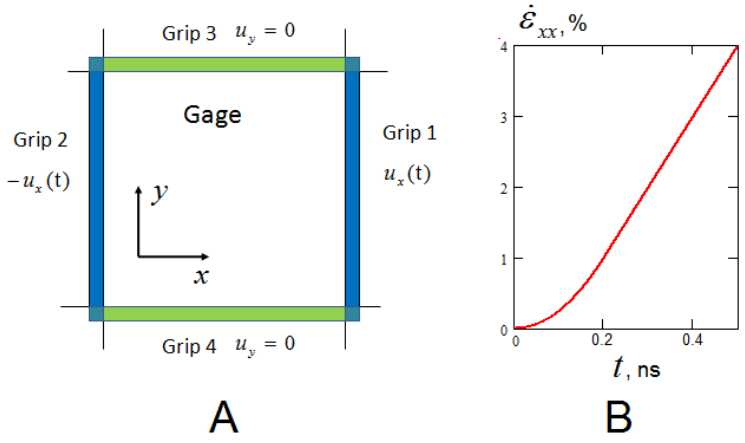


Figure 30. Mechanical test on a CNT film specimen.

The specimen is subjected to a constant strain rate tension test with the strain rate of $0.1$ $ns^{-1}$. In order to avoid dynamic response, a gradual acceleration period of $0.1$ ns is used (Fig. 30(B)).

The test results are presented in Fig. 31. Four specimens were tested: $0.3\times0.3$ μm, $0.4\times0.4$ μm, $0.5\times0.5$ μm, $0.6\times0.6$ μm , in order to assess size dependence of the response. It appears that specimens display size dependent stress-strain curves with initial linear region, followed by gradual softening. Initial slope of the stress-strain curve corresponds to elastic modulus of 16 GPa, the yield strength of CNT paper is approximately 200-250 MPa.

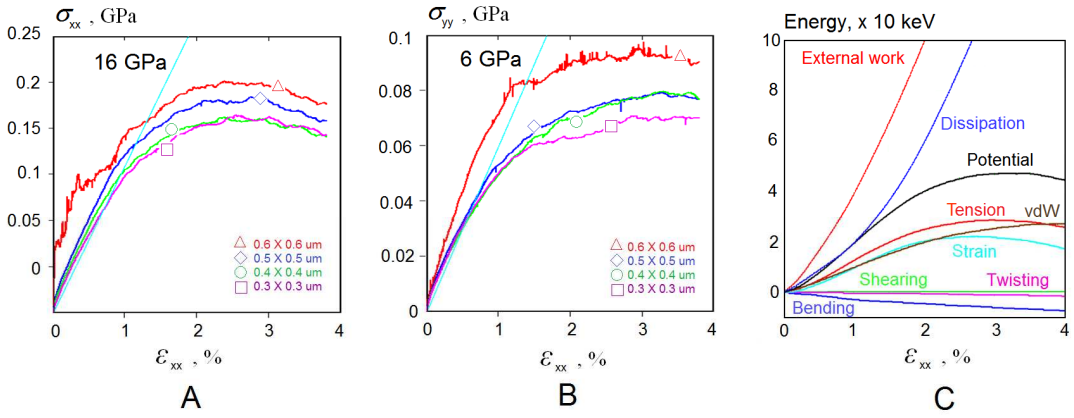


Figure 31. Tensile tests on CNT film specimens of different size. (A) $\sigma_{xx}(\varepsilon_{xx})$ curve. (B) $\sigma_{yy}(\varepsilon_{xx})$ curve. (C) Energy balance during the test.

Figure 31 (B) gives transverse stresses in confined CNT film. Assuming linear elastic behavior, we can estimate film's Poisson's ratio as $\sigma_{xx}/\sigma_{yy} = 0.375$, and Young's modulus of the film as $(\sigma_{xx}/\varepsilon_{yy})(1-\nu^2) = 13.75$ GPa. These values are consistent with available experimental data for CNT papers and unsupported CNT films [9].

Energy balance curves presented in Fig 31(C) indicate inelastic response, similar to one studied in section 3.2. Non-dissipative part of the response is conditioned by the changes in the elastic energy of CNTs and vdW adhesion energy. The elastic energy is stored mostly in tension of CNTs, whereas bending energy drops down due to straightening of CNTs.

Figure 32 present kinematics of CNTs in a specimen. It appears that although the deformation observed in the test is nearly uniform (Fig. 32(A)), the distribution of slip is

non-uniform, because grips prohibit relative slip of CNTs at the edges, therefore slip is localized in the center of the specimen (Fig. 32(B)). Therefore, specimens exhibit the behavior similar to 1D CNT structures described in section 3.2. Therefore, we can conclude that the size dependence of stress-strain curves is associated with uneven distribution of slip within a specimen. Fig. 32(C) demonstrates that the load transfer in tensile tests occurs mostly through bundles parallel to the load direction.

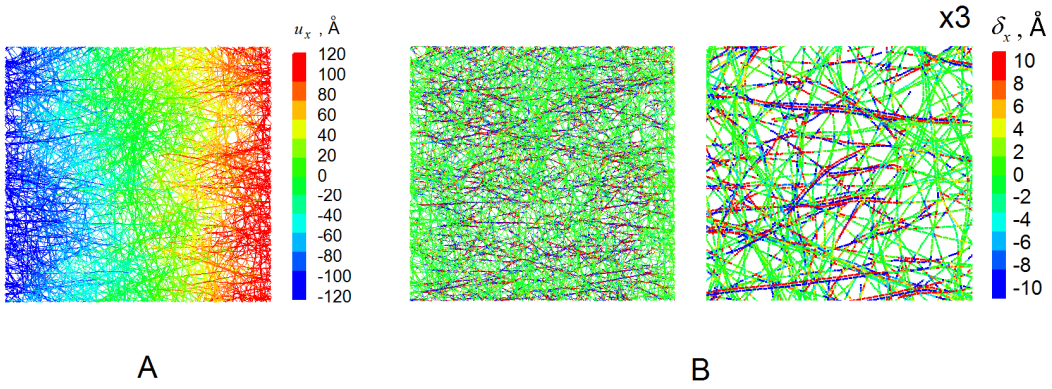


Figure 32. Kinematics of CNT deformation in CNT film specimen. (A) Displacement field. (B) $x$-component of slip vector. Right picture gives $3x$ enlarged sample part of a specimen.

It worth noting here that the mechanics of CNT films under compression and in shear are significantly different, due to difference in mechanisms of the load transfer and deformation. However, the derivation of nonlinear constitutive laws describing deformation mechanisms of CNT film faces insurmountable computational limitations and therefore remains beyond the scope of this work.

# Chapter 4

# Concluding remarks

Increasing interest in nanostructures in general and carbon nanotubes in particular facilitates the development of new theoretical approaches and numerical modeling tools that help explain complex mechanical behaviors of nanostructured materials. This thesis is devoted to the development of a robust tool of mesoscopic modeling of large assemblies of carbon nanotubes. The established macroscopic modeling concept of distinct elements has been employed as a foundation for our mesoscale model. The important interactions present on the mesoscale were encapsulated into two types of contact models. Mechanics of intratube bonds was incorporated into parallel bond contact model. Intertube interactions were captured with anisotropic vdW contact model. Energy dissipation was accounted for in a top-down manner, based on the macroscopic mechanical properties of carbon nanotube materials. Combination of numerous successful solutions (basic formalism of distinct element method, advanced algorithms of contact search, modern architectural solutions including multi-threading and memory handling, efficient contact models, time integration schemes based on quaternion representation of rotations) resulted in a very efficient tool, that have already gained recognition as one of the most robust models in the field of mesoscopic modeling of CNTs.

The developed model has been applied to the analysis of various mesoscopic structures and materials - self-folded nanotube configurations, nanotube bundles and ropes, nanotube papers and films. The results of mesoscopic simulations fully agree with experimental observations. It was demonstrated that the CNT sliding is an important mechanism of formation of self-folded structures and self-assembly of CNT material nanostructure. It was shown that energy dissipation plays an important role in the material response of weakly bonded CNT structures. Various strategies of improving the mechanical performance of cross-linked CNT materials were explored. Mechanisms of load transfer and deformation in CNT films were qualitatively studied. Many simulations, such as modeling tensile and torsional tests on CNT bundles with intertube sliding and dissipation, analysis of representative volume element in aligned CNT structures, modeling multiple-coil CNT rings – were performed with our model for the first time.

However, as any coarse-grained model, our DEM model has certain natural limitations. Certain restrictions of the used formalism are related to parallel bond model. Incremental decoupled formulation of constitutive laws is suitable only for small deformations and leads to significant errors when applied to modeling of CNT large deformations and failure. Therefore, further improvement of the model implies the replacement of the parallel bond model with one of the more advanced bonding models that have been developed during the last 6 years [72, 84].

Another issue that remains unresolved within the suggested approach is the quantitatively correct description of rate effects. The challenges here are related to both

complex underlying physics and natural limitations of the approach based on the dynamics of coarse-grained rigid particles.

Simple shear and twisting examples reveal another important deficiency of the model - it does not capture load transfer mechanisms that originate from atomistic discreteness of CNT surfaces [92]. These mechanisms are important for certain class of problems, and therefore the results of the DEM analysis of these problems should be treated with caution. In particular, shear stiffness and strength of rectangular specimen considered in section 3.3, as well as torsional stiffness obtained for a volatile bundle in section 3.4 should be considered as lower bound estimates.

However, in many other aspects our model remains the most advanced model in the field and can be employed as an efficient tool in numerous research problems related to modeling mechanics of CNT nanostructures (devices) and nanostructured materials.

# References

[1] Iijima, S., 1991. Helical microtubules of graphitic carbon. Nature 354, 56-58.

[2] Ando, Y., Zhao, X., 2006. Synthesis of carbon nanotubes by arc discharge method. New diamond and frontier carbon technology 16(3), 123-137.

[3] Musaddique, M. et al., 2011. Production of carbon nanotubes by different routes - a review. Journal of encapsulation and adsorption sciences 1, 29-34.

[4] Kumar, M., Ando, Y., 2010. Chemical vapor deposition of carbon nanotubes: a review on growth mechanism and mass production. Journal of nanoscience and nanotechnology 10, 3739-3758.

[5] Arsecularatne, J., Zhang, L.-C., 2007. Carbon nanotube reinforced ceramic composites and their performance. Recent patents on nanotechnology 1, 176-185.

[6] Kaur, S. et al., 2006. Design and characterization of three-dimensional carbon nanotube foams. Journal of physical chemistry B 110(42), 21377-21380.

[7] Martel, R., Shea, H., Avouris, P., 1999. Rings of single-walled carbon nanotubes. Nature 398, 299.

[8] K. Lao et al., 2003. Superhydrophobic carbon nanotube forests. Nano letters 3(12), 1701-1705.

[9] Hobbie, E.K. et al., 2010. Wrinkling and strain softening in single-wall carbon nanotube membranes. Physical review letters 104, 125505.

[10] N. Kouklin, 2005. Self-assembled network of carbon nanotubes synthesized by chemical vapor deposition in alumina porous template. Applied physics letters 87, 203105.

[11] Tahhan, M., et al., 2003. Carbon nanotube and polyaniline composite actuators. Smart materials and structures 12, 626-632.

[12] Foroughi, J. et al, 2011. Torsional carbon nanotube artificial muscles. Science 28, 334(6055), 494-497.

[13] Yu, M.-F. et al., 2000. Tensile loading of ropes of single wall carbon nanotubes and their mechanical properties. Physical review letters 84(24), 5552-5555.

[14] Vigolo, B. et al., 2000. Macroscopic fibers and ribbons of oriented carbon nanotubes. Science 290, 1331-1334.

[15] Zhu, H. et al., 2002. Direct synthesis of long single-walled carbon nanotube strands. Science 296, 884-886.

[16] Beese, A.M. et al., 2013. Bio-inspired carbon nanotube polymer composite yarns with hydrogen bond-mediated lateral interactions. ACS Nano 7(4), 3434-3446.

[17] Mylvaganam, K., Zhang, L-C., 2007. Ballistic resistance capacity of carbon nanotubes. Nanotechnology 18, 475701.

[18] Suhr, J. et al., 2005. Viscoelasticity in carbon nanotube composites. Nature Materials 4, 134-137.

[19] Xu, M. et al, 2010. Carbon nanotubes with temperature-invariant viscoelasticity from –196° to 1000℃. Science 330, 1364-1368.

[20] Che, J. et al., 2000. Thermal conductivity of carbon nanotubes. Nanotechnology 11, 65-69.

[21] Zhao, Y. et al., 2011. Characterizing the viscoelastic properties of layer-by-layer carbon nanotube-polyelectrolyte thin films. Smart materials and structures 20, 075020.

[22] Zhang, Q. et al., 2010. Viscoelastic creep of vertically aligned carbon nanotubes. Journal of physics D: applied physics 43, 315401.

[23] Hall et al., 2008. Sign change of Poisson's ratio for carbon nanotube sheets. Science 320, 504.

[24] Ma, Y.-J. et al., 2010. Carbon nanotube films change Poisson's ratios from negative to positive. Applied physics letters 97, 061909.

[25] H. Eschrig, 1996. Fundamentals of density functional theory. Teubner-Verlagsgesellscaft, Stuttgart-Leipzig.

[26] Slater, J. C., Koster, G. F., 1954. Simplified LCAO method for the periodic potential problem. Physical review 94(6), 1498-1524.

[27] Tersoff, J., 1988. New empirical approach for the structure and energy of covalent systems. Physical review B 37(12), 632-635.

[28] Stillinger, F., Weber, T.A., 1985. Computer simulation of local order in condensed phases in silicon. Physical review B 31, 5262.

[29] Lennard-Jones, J. E., 1924. On the determination of molecular fields. Proceedings of the royal society of London 106 (738), 463-477.

[30] Verlet, L., 1967. Computer "experiments" on classical fluids. I. Thermodynamical properties of Lennard−Jones molecules. Physical review 159, 98-103.

[31] Zhang, D.-B., Dumitrica, T., 2008. Elasticity of ideal single-walled carbon nanotubes via symmetry-adapted tight-binding objective modeling. Applied physics letters 93(3), 031919.

[32] Dumitrica, T. et al., 2006. Symmetry-, time-, and temperature-dependent strength of carbon nanotubes. Proceedings of the national academy of science USA 103(16), 6105-6109.

[33] Nikiforov, I. et al., 2010. Wavelike rippling in multiwalled carbon nanotubes under pure bending. Applied physics letters 96, 123107.

[34] Buehler, M.J., 2006. Mesoscale modeling of mechanics of carbon nanotubes: Self-assembly, self-folding, and fracture. Journal of materials research 21(11), 2855-2869.

[35] Cranford, S.W., Buehler, M.J., 2010. In silico assembly and nanomechanical characterization of carbon nanotube buckypapers. Nanotechnology 21, 265706.

[36] Hahm, M.G., 2012. Bundling dynamics regulates the active mechanics and transport in carbon nanotube networks and their nanocomposites. Nanoscale 4, 3584-3590.

[37] Xie, B., et al., 2011. Mechanics of carbon nanotube networks: microstructural evolution and optimal design. Soft matter 7, 10039-10047.

[38] Li, Y., Kroger, M., 2012. A theoretical evaluation of the effects of carbon nanotube entanglement and bundling on the structural and mechanical properties of buckypaper. Carbon 50, 1793-1806.

[39] Li, Y., Kroger, M., 2012. Viscoelasticity of carbon nanotube buckypaper: zipping-unzipping mechanism and entanglement effects. Soft matter 8, 7822.

[40] Zhigilei, L.V. et al., 2005. Mesoscopic model for dynamic simulations of carbon nanotubes. Physical review B 71, 165417.

[41] Volkov, A.N., et al., 2008. Mesoscopic model for simulation of CNT-based materials. In: Proceedings of the ASME International Mechanical Engineering Congress and Exposition, Boston, MA, October 31 - November 6, 2008: 1-11.

[42] Volkov, A.N., Zhigilei L.V., 2010. Mesoscopic interaction potential of carbon nanotubes of arbitrary length and orientation, Journal of physical chemistry C 114, 5513-5531.

[43] Volkov, A.N., Zhigilei, L.V., 2010. Scaling laws and mesoscopic modeling of thermal conductivity in carbon nanotube materials. Physical review letters 104, 215902.

[44] Volkov, A.N., Zhigilei, L.V., 2010. Structural stability of carbon nanotube films: The role of bending buckling. ACS Nano 4(10), 6187-6195.

[45] Jacobs, W.M., et al., 2012. Acoustic energy dissipation and thermalization in carbon nanotubes: Atomistic modeling and mesoscopic description. Physical review B 86, 165414.

[46] Anderson, T., et al., 2010. Toward distinct element method simulations of carbon nanotube systems. Journal of nanotechnology in engineering and medicine 1, 0410009.

[47] Ostanin, I., Ballarini, R., Potyondy, D., and Dumitrică, T., 2013. A distinct element method for large scale simulations of carbon nanotube assemblies. Journal of the mechanics and physics of solids 61(3), pp. 762-782.

[48] Wang, Y., Gaidău, C., Ostanin, I., Dumitrică, T., 2013, Ring windings from single-wall carbon nanotubes: A distinct element method study. Applied physics letters 103(18), 183902.

[49] Ostanin, I., Ballarini, R., and Dumitrică, T., 2014. Distinct element method modeling of carbon nanotube bundles with intertube sliding and dissipation. Journal of applied mechanics 81(6), 061004.

[50] Ostanin, I., Ballarini, R., and Dumitrică, T., 2014, A distinct element modeling of cross-linked carbon nanotube bundles with distinct element method. Unpublished manuscript.

[51] Rouse, P.E., 1953. A theory of the linear viscoelastic properties of dilute solutions of coiling polymers. Journal of chemical physics 21(7), 1272-1280.

[52] Zimm, B.H., 1956. Dynamics of polymer molecules in dilute Solution: viscoelasticity, Flow Birefringence and Dielectric Loss. Journal of chemical physics 24(2), 269-278.

[53] Underhill, P.T., Doyle, P.S., 2003. On the coarse-graining of polymers into bead-spring chains. Journal of non-newtonian fluid mechanics 122, 3-31.

[54] Ensing, B., Nielsen, S., 2010. Multiscale molecular dynamic and the reverse mapping problem. In: Dumitrica, T. (Ed.), Trends in computational nanomechanics.

Springer Inc., Dordrecht Heidelberg London New York, 25-59.

[55] Cranford, S., Buehler, M., 2010. Coarse-graining parameterization and multiscale simulation of hierarchical systems. In: Derosa, P., (Ed.), Cagin, T., (Ed.), Multiscale modeling: from atoms to devices. CRC Press, 13-34.

[56] Belytschko, T., Song, J.-H., 2010. Coarse-graining of multiscale crack propagation. International journal for numerical methods in engineering 81, 537-563.

[57] Jeong, B.-W., Sinott, S.B., 2009. Atomic scale simulations of the mechanical behavior of carbon nanotube systems. In: Dumitrica, T. (Ed.), Trends in computational nanomechanics.Springer Inc., Dordrecht Heidelberg London New York, 25-59.

[58] Flory, P.J., 1969. Statistical mechanics of chain molecules. New York: Interscience Publishers.

[59] Cundall, P.A., Strack, O., 1979. A discrete numerical model for granular assemblies. Geotechnique 29, 47-65.

[60] Cundall, P.A., Strack, O., 1988. Formulation of a three-dimensional distinct element model. part i: A scheme to detect and represent contacts in a system composed of many polyhedral blocks. International journal of rock mechanics and mining sciences & Geomechanics abstracts 25, 107-116.

[61] Hart, R., Cundall, P., Lemos, J., 1988. Formulation of a three-dimensional distinct element model. part ii: Mechanical calculations for motion and interaction of a system composed of many polyhedral blocks. International journal of rock mechanics and mining sciences & Geomechanics abstracts 25: 117-126.

[62] Pande, G., Beer, G., Williams, J.R., 1990. Numerical modeling in rock mechanics. John Wiley and Sons.

[63] Itasca Consulting Group Inc. PFC3D (Particle Flow Code in 3 Dimensions). Version 4.0. Minneapolis 2008.

[64] Potyondy, D., Cundall, P., 2004. A bonded-particle model for rock. International journal of rock mechanics and mining sciences 41(8), 1329-1364.

[65] Munjiza, A. et al., 2003. 3D dynamics of discrete element systems comprising irregular discrete elements – integration solution for finite rotations in 3D. International journal for numerical methods in engineering 56, 35-55.

[66] Johnson, S.M. et al, 2008. Quaternion-based rigid body rotation integration algorithms for use in particle methods. International journal for numerical methods in engineering 74, 1303-1313.

[67] Johnson, S.M. et al, 2009. On the application of quaternion-based approaches in discrete element methods. Engineering computations: international journal for computer-aided engineering and software 26(6), 610-620.

[68] Evans, D.J. 1977. On the representation of orientation space. Molecular physics 34, 317-25.

[69] Shoemake, K., 1985. Animating rotation using quaternions. ACM SIGGRAPH85, San Francisco, CA.

[70] Zhang, D, Dumitrica, T., 2008. Elasticity of ideal single-walled carbon nanotubes via symmetry-adapted tight-binding objective modeling. Applied physics letters 93, 031919-031921.

[71] Levente Tapasztó et al., 2012. Breakdown of continuum mechanics for nanometre-wavelength rippling of graphene. Nature physics 8, 739-742.

[72] Wang, Y., 2009. A new algorithm to model the dynamics of 3-D bonded rigid bodies with rotations. Acta geotechnica 4:117-127.

[73] London, F.,1930. Zur theorie und systematik der molekularkrafte. Zeitschrift für physik 63, 245-279 (in German).

[74] Hamaker, H.C.,1937. The London-van der Waals attraction between spherical particles. Physica 4, 1058-1072.

[75] Dzyaloshinskii, I.E., Lifshitz, E.M., Pitaevskii, L., 1961. General theory of van der Waals' forces. Soviet physics uspekhi 4, 153.

[76] Rajter, R.F. et al., 2007. Van der Waals–London dispersion interactions for optically anisotropic cylinders: metallic and semiconducting single-wall carbon nanotubes. Physical Review B 76, 045417.

[77] Hobbie, E. et al., 2012. Empirical evaluation of attractive van der Waals potentials for type-purified single-walled carbon nanotubes. Physical review B 85, 245439.

[78] Gay, J. G., Berne B. J.,1981. Modification of the overlap potential to mimic a linear site–site potential. Journal of chemical physics 74, 3316.

[79] Akatyeva, E, 2010. Van der Waals interactions between two identical parallel tubes. Unpublished manuscript.

[80] Carlson, A., Dumitrica, T., 2007. Extended tight-binding potential for modeling intertube interactions in carbon nanotubes. Nanotechnology 18, 065706.

[81] Filleter, T. et al, 2012. Experimental-computational study of shear interactions within double-walled carbon nanotube bundles. Nano letters 12, 732-742.

[82] Popov, V.L. Contact mechanics and friction. Springer Heidelberg Dordrecht London New York, 2010.

[83] Zhang, Q., et al., 2010. Viscoelastic creep of vertically aligned carbon nanotubes. Journal of physics D: Applied physics 43(31), 315401.

[84] Itasca Consulting Group Inc. FLAC3D – Fast Lagrangian Analysis of Continua in 3 Dimensions. Version 5.0. Minneapolis 2006.

[85] Kuzkin, V.A., Asonov, I.E., 2012. Vector-based model of elastic bonds for simulation of granular solids. Physical review E 86, 051301.

[86] Rurali, R., Hernandez, E., 2003. Trocadero: a multiple-algorithm multiple-mode atomistic simulation program. Computational material science 28, 85-106.

[87] Humphrey, W. et al., 1996. VMD—visual molecular dynamics. Journal of molecular graphics 14, 33-38.

[88] Lu, W, Chou, T.-W., 2011, Analysis of the entanglements in carbon nanotube fibers using a self-folded nanotube model. Journal of the mechanics and physics of solids 59, 511–524.

[89] Wang, Y., Semler, M., Ostanin, I., Hobbie, E., Dumitrica, T., 2014. Rings and rackets from single-wall carbon nanotubes: manifestations of mesoscale mechanics. Submitted manuscript.

[90] Thess, A. et al., 1996. Crystalline ropes of metallic carbon nanotubes. Science 273, 483-487.

[91] Dalton, A.B., 2003. Super-tough carbon-nanotube fibers. Nature 423, 703.

[92] Behabtu, N. et al., 2013. Strong, light, multifunctional fibers of carbon nanotubes with ultrahigh conductivity. Science 339(6116), 182-186.

[93] Tang, Y. et al., 2010. Deformation micromechanisms of collagen fibrils under uniaxial tension. Journal of the Royal Society Interface 7, 839–850.

[94] Li, C. et al., 2010. Interfacial shear strengths between carbon nanotubes.

Nanotechnology 21(11), 115704.

[95] Papadakis, S.J. et. al., 2004. Resonant oscillators with carbon-nanotube torsion springs. Physical review letters 93(14), 146101.

[96] Fennimore, A.M. et. al, 2003. Rotational actuators based on carbon nanotubes. Nature 424, 408.

[97] Jeong, B.-W. et al., 2007. Elastic torsional responses of carbon nanotube systems. Journal of applied physics 101, 084309.

[98] Jean-Baptiste Donnet (ed), Carbon fibers. Third edition, revised and expanded. Marcel Dekker New York Basel 1998.

[99] S Acquah et al., In: J. M. Marulanda (Ed.) Electronic properties of carbon nanotubes, in Tech 2011.

[100] C. F. Cornwell and C. R. Welch, 2011. Very-high-strength (60-GPa) carbon nanotube fiber design based on molecular dynamics simulations. Journal of chemical physics 134, 204708.

[101] H. Stahl et al, 2000. Intertube coupling in ropes of single-wall carbon nanotubes. Physical review letters 85: 5186-5189.

[102] A. Kis et al., 2004. Reinforcement of single-walled carbon nanotube bundles by intertube bridging. Nature materials 3: 153-157.

[103] Ostoja-Starzewski, M., 2009. Continuum mechanics models of fractal porous media: integral relations and extremum principles. Journal of mechanics of materials and structures 4(5), 901-912.

[104] Kulak, M., 2002. Fraktalnaya mekhanica materialov. Minsk, Visheyshaya shkola (in Russian).

# APPENDIX A

**Small deflections of parallel bonded model of the beam**

Consider a parallel bonded model of a beam. The chain of rigid balls (distinct elements), connected via flat interfaces – parallel bonds (Fig 33).

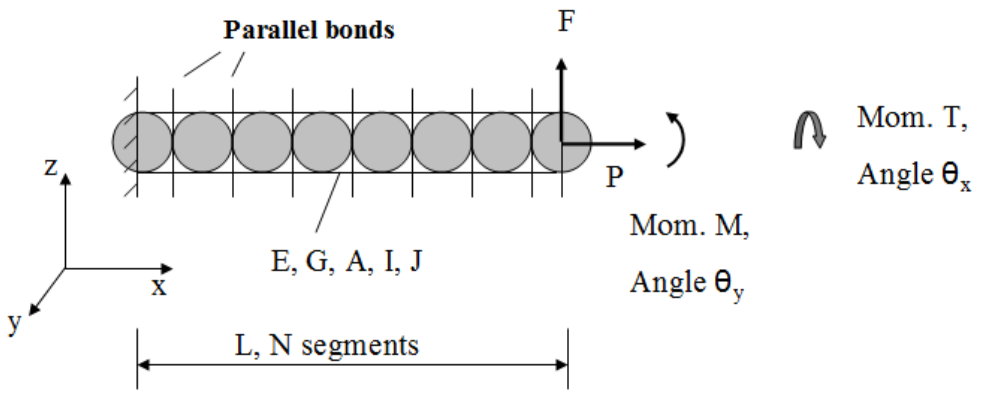


Figure 33. The parallel bonded model of a tip-loaded cantilever beam. The cantilever beam made of material with Young's modulus $E$ and shear modulus $G$ that have a cross-section with area $A$, moment of inertia $I$ and polar moment of inertia $J$, is loaded at the tip with axial force $P$, transverse force $F$, bending moment $M$, twisting moment $T$.

The chain consists of $N$ parallel bonds and $N+1$ distinct elements. Coordinates of element centers are:

$$x_b(i) = \frac{L}{N} i, \quad i = 0..N \tag{A.1}$$

Coordinates of parallel bond interfaces are:

$$x_{pb}(i) = -\frac{L}{2N} + \frac{L}{N} i, \quad i = 1..N \tag{A.2}$$

Parallel bond provides the following constitutive relations at nodal cross sections (scalar form):

$$\begin{aligned} P(i) &= -k_n A \cdot \Delta u_x(i) \\ F(i) &= -k_s A \cdot \Delta u_z(i) \\ M(i) &= -k_n I \cdot \Delta \theta_y(i) \\ T(i) &= -k_s J \cdot \Delta \theta_x(i) \end{aligned} \tag{A.3.1-A.3.4}$$

where $k_n = E / \Delta L$ , $k_s = G / \Delta L$ , $\Delta L = L / N$ ; $P_i$, $F_i$, $M_i$, $T_i$ are restoring forces (moments) that are developed at $i$-th parallel bond contact. These constitutive laws reproduce the behavior of a flat interface with distributed springs of normal and shear stiffness $k_n$ and $k_s$ . The analytical solution for an Euler-Bernoulli (no shear deformation/energy) beam is as follows:

$$u_z(x) = \frac{Fx^2}{2EI}\left(L - \frac{x}{3}\right) + \frac{Mx^2}{2EI}$$
$$u_x(x) = \frac{Px}{EA}$$
$$\theta_y(x) = \frac{Fx}{EI}\left(L - \frac{x}{2}\right) + \frac{Mx}{EI} \qquad \text{(A.4.1-A.4.4)}$$
$$\theta_x(x) = \frac{Tx}{GJ}$$

Substituting the coordinates (A.1) into solution (A.4), we obtain the following expressions for angles and displacements at nodal points due to different types of loading, applied at a tip of the beam.

Longitudinal displacement due to axial force:

$$u_x^{\,a}(n) = \frac{PL}{EA}\frac{n}{N} \qquad \text{(A.5)}$$

Torsion angle due to twisting moment:

$$\theta_x^{\,a}(n) = \frac{TL}{GJ}\frac{n}{N} \qquad \text{(A.6)}$$

Local slope (angle) due to bending moment:

$$\theta_y^{\,a}(n) = \frac{ML}{EI}\frac{n}{N} \qquad \text{(A.7)}$$

Deflection due to bending moment:

$$u_z^{\,a}(n) = \frac{ML^2}{2EI}\frac{n^2}{N^2} \tag{A.8}$$

Local slope (angle) due to applied force:

$$\theta_y^{\,a}(n) = \frac{FL^2}{EI}\left(\frac{n}{N}\left(1-\frac{n}{2N}\right)\right) = \frac{FL^2}{EI}\left(\frac{n}{N}-\frac{n^2}{2N^2}\right) \tag{A.9}$$

Transverse displacement due to applied force:

$$u_z^{\,a}(n) = \frac{FL^3}{2EI}\left(\frac{n^2}{N^2}\left(1-\frac{n}{3N}\right)\right) = \frac{FL^3}{2EI}\left(\frac{n^2}{N^2}-\frac{n^3}{3N^3}\right) \tag{A.10}$$

Consider now the nodal displacements predicted by parallel bond constitutive laws (A.3). Constitutive laws (A.1) may be presented in the following form:

$$\Delta u_x(i) = \frac{P(i)L}{EAN} \tag{A.11.1-A.11.4}$$
$$\Delta u_z(i) = \frac{F(i)L}{GAN}$$
$$\Delta \theta_y(i) = \frac{M(i)L}{EIN}$$
$$\Delta \theta_z(i) = \frac{T(i)L}{GJN}$$

Here we do not consider transverse displacements due to shear deformation, and replace equation (A.11.2) with $\Delta u_z(i) = 0$.

Equations (A.5), (A.6) are reproduced by direct summation of deflections/angles at each parallel bond interface. We utilize the facts that in case of these two types of deformations the loads ($P$, $T$) are distributed uniformly over the length of the beam:

$P(i) = P$ , $T(i) = T$ ; displacements (angles) $u_x$ , $\theta_x$ at each parallel bond interface are equal, and

$$u_x(x_{pb}(i)) = u_x(x_b(i)) = u(i)$$
$$\theta_x(x_{pb}(i)) = \theta_x(x_b(i)) = \theta_x(i) \qquad \text{(A.12.1-A.12.2)}$$

Longitudinal displacement due to axial force:

$$u_x(n) = \sum_{i=1}^{n} \Delta u_x(i) = \sum_{i=1}^{n} \frac{P(i)L}{EAN} = \frac{PL}{EA}\frac{n}{N} \qquad \text{(A.13)}$$

Torsion angle due to twisting moment:

$$\theta_x(n) = \sum_{i=1}^{n} \Delta \theta_x(i) = \sum_{i=1}^{n} \frac{T(i)L}{GJN} = \frac{TL}{GJ}\frac{n}{N} \qquad \text{(A.14)}$$

Therefore, for these two types of deformations parallel bonded model exactly reproduces the behavior of the beam.

Flexural deformations (A.7), (A.8), (A.9), (A.10) require more detailed consideration.

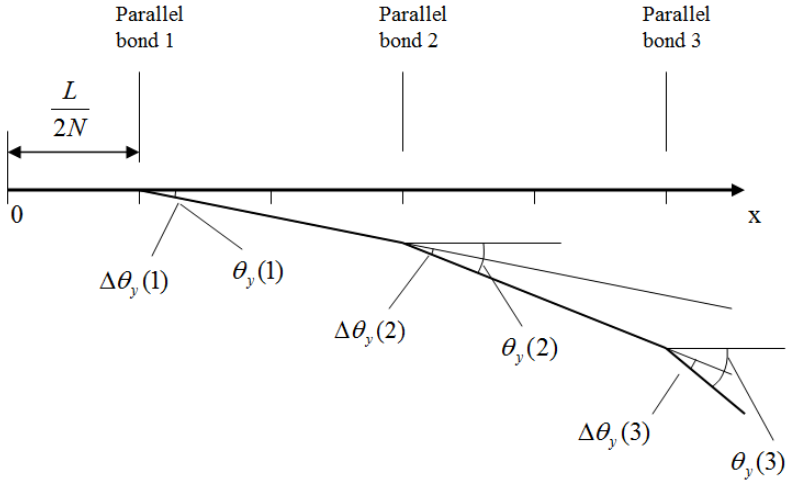


Figure 34. Geometric illustration of a flexure of a parallel bonded chain.

Fig. 34 illustrates the transverse deformation of a chain of parallel bonded distinct elements. Assuming small bending angles $\theta_y(i)$, one can obtain the following relations:

$$\theta_y(n) = \sum_{i=1}^{n} \Delta\theta_y(i)$$
$$u_z(n) = \sum_{i=1}^{n} \frac{(2i-1)L}{2N} \Delta\theta_y(n+1-i) \qquad \text{(A.15)}$$

In the case of bending of the beam by a constant moment we have:

$$\theta_y(n) = \sum_{i=1}^{n} \Delta\theta_y(i) = \sum_{i=1}^{n} \frac{M(i)L}{EIN} = \frac{ML}{EI}\frac{n}{N} \qquad \text{(A.16)}$$

$$u_z(n) = \sum_{i=1}^{n} \frac{(2i-1)L}{2N} \Delta\theta_y(n+1-i) = \sum_{i=1}^{N} \frac{(2i-1)L^2}{2N^2}\frac{M}{EI} = \frac{ML^2}{2EI}\frac{n^2}{N^2} \qquad \text{(A.17)}$$

which exactly reproduces solutions (A.7), (A.8). Therefore, parallel bonded model exactly reproduces small deflections of a beam in pure bending state.

Consider the case of transverse force applied at a tip. It creates the following bending moment at cross sections of parallel bonds:

$$M(i) = F(L - x_{pb}(i)) = FL\left(1 + \frac{1}{2N} - \frac{i}{N}\right) \tag{A.18}$$

Substituting these moments into relation (A.11.3) and using relations (A.15), one has the following slope angles and deflections for a tip-loaded cantilever beam:

$$\theta_y(n) = \sum_{i=1}^{n} \Delta\theta_y(i) = \sum_{i=1}^{n} \frac{M(i)L}{EIN} = \sum_{i=1}^{n} \frac{FL^2}{EIN^2}\left(N + \frac{1}{2} - i\right) = \frac{FL^2}{EI}\left(\frac{n}{N} - \frac{n^2}{2N^2}\right) \tag{A.19}$$

$$\begin{aligned}
&u_z(n) = \sum_{i=1}^{n} \frac{(2i-1)L}{2N} \Delta\theta_y(n+1-i) = \sum_{i=1}^{n} \frac{(2i-1)L}{2N} \frac{M(N+1-i)L}{EIN} = \\
&\sum_{i=1}^{n} \frac{L}{2N}(2i-1)\frac{L}{EIN^2} FL\left(N + \frac{1}{2} - n - 1 + i\right) = \\
&\sum_{i=1}^{n} \frac{FL^3}{2EIN^3}\left(2Ni - N - i + \frac{1}{2} - 2ni + n + 2i^2 - i\right) = \\
&\frac{FL^3}{2EIN^3}\left[\left(n - N + \frac{1}{2}\right)\sum_{i=1}^{n} 1 + 2(N - n - 1)\sum_{i=1}^{n} i + 2\sum_{i=1}^{n} i^2\right] = \\
&\frac{FL^3}{2EIN^3}\left[\left(n - N + \frac{1}{2}\right)n + 2(N - n - 1)\frac{n}{2}(n+1) + 2\left(\frac{n^3}{3} + \frac{n^2}{2} + \frac{n}{6}\right)\right] = \\
&\frac{FL^3}{2EI}\left(\frac{n^2}{N^2} - \frac{n^3}{3N^3}\right) - \frac{FL^3}{2EI}\frac{n}{6N^3}
\end{aligned} \tag{A.20}$$

Therefore, the numerical solution does not coincide with expression (A.10). Rewrite (A.20) for convenience of error estimation:

$$u_z(n) = u_z^a(n)\left(1 - \frac{1}{6Nn - 2n^2}\right) \tag{A.21}$$

At the tip:

$$u_z(N) = u_z^a(N)\left(1 - \frac{1}{4N^2}\right) \tag{A.22}$$

The error does not depend on the geometry of the beam, but only on the number of segments.

As we can see on this small slope cantilever beam example, the chain of parallel bonded distinct elements does reproduce elastic solutions for an Euler-Bernoulli beam with good precision, the error does not exceed $O(\mathrm{N}^{-2})$.

# APPENDIX B

**Contact forces and contact stiffnesses of anisotropic vdW contact model**

Anisotropic contact model for vdW interactions is given by the potential:

$$U(R,\theta,\gamma)=\Gamma(R,\gamma)\,f_c(R)V^k(R,\theta) \tag{B.1}$$

The normal and shear forces and aligning moments (applied at the center of elements in contact) are:

$$\begin{aligned}
F_R &= -\frac{dU}{dR} = -\frac{\partial\Gamma(R,\gamma)}{\partial R}\,f_c(R)V^k(R,\theta) - \Gamma(R,\gamma)\frac{df_c(R)}{dR}V^k(R,\theta) - \Gamma(R,\gamma)\,f_c(R)\frac{\partial V^k(R,\theta)}{\partial R}\\
F_\theta &= -\frac{1}{R}\frac{\partial U}{\partial\theta} = -\frac{1}{R}\Gamma(R,\gamma)\,f_c(R)\frac{\partial V^k(R,\theta)}{\partial\theta}\\
M_\gamma &= -\frac{dU}{d\gamma} = -\frac{\partial\Gamma(R,\gamma)}{\partial\gamma}\,f_c(R)V^k(R,\theta)
\end{aligned} \tag{B.2}$$

The corresponding stiffnesses are

$$\begin{aligned}
k_R &= \left|\frac{d^2U}{dR^2}\right| = \left|\left(\frac{\partial^2\Gamma(R,\gamma)}{\partial R^2}\,f_c(R) + \frac{\partial\Gamma(R,\gamma)}{\partial R}\frac{df_c(R)}{dR}\right)V^k(R,\theta) + \frac{\partial\Gamma(R,\gamma)}{\partial R}\,f_c(R)\frac{\partial V^k(R,\theta)}{\partial R}\right.\\
&+\left(\frac{\partial\Gamma(R,\gamma)}{\partial R}\frac{df_c(R)}{dR} + \Gamma(R,\gamma)\frac{d^2f_c(R)}{dR^2}\right)V^k(R,\theta) + \Gamma(R,\gamma)\frac{df_c(R)}{dR}\frac{\partial V^k(R,\theta)}{\partial R}\\
&\left.+\left(\frac{\partial\Gamma(R,\gamma)}{\partial R}\,f_c(R) + \Gamma(R,\gamma)\frac{df_c(R)}{dR}\right)\frac{\partial V^k(R,\theta)}{\partial R} + \Gamma(R,\gamma)\,f_c(R)\frac{\partial^2V^k(R,\theta)}{\partial R^2}\right|\\
k_\theta &= \left|\frac{1}{R^2}\frac{d^2U}{d\theta^2}\right| = \left|\frac{1}{R^2}\Gamma(R,\gamma)\,f_c(R)\frac{\partial^2V^k(R,\theta)}{\partial\theta^2}\right|\\
k_\gamma &= \left|\frac{1}{R^2}\frac{d^2U}{d\gamma^2}\right| = \left|\frac{1}{R^2}\frac{\partial^2\Gamma(R,\gamma)}{\partial R^2}\,f_c(R)V^k(R,\theta)\right|
\end{aligned} \tag{B.3}$$

Here

$$
\begin{aligned}
V^k(R,\theta) &= 4\varepsilon''\left(\frac{A'}{(D^k(R,\theta))^{\alpha'}} - \frac{B'}{(D^k(R,\theta))^{\beta'}}\right) \\
\frac{\partial V^k(R,\theta)}{\partial R} &= 4\varepsilon''\left(-\frac{\alpha' A'}{(D^k(R,\theta))^{\alpha'+1}} + \frac{\beta' B'}{(D^k(R,\theta))^{\beta'+1}}\right)\frac{\partial D^k(R,\theta)}{\partial R} \\
\frac{\partial V^k(R,\theta)}{\partial \theta} &= 4\varepsilon''\left(-\frac{\alpha' A'}{(D^k(R,\theta))^{\alpha'+1}} + \frac{\beta' B'}{(D^k(R,\theta))^{\beta'+1}}\right)\frac{\partial D^k(R,\theta)}{\partial \theta} \\
\frac{\partial^2 V^k(R,\theta)}{\partial^2 R} &= 4\varepsilon''\left(\frac{\alpha'(\alpha'+1)A'}{(D^k(R,\theta))^{\alpha'+2}} - \frac{\beta'(\beta'+1)B'}{(D^k(R,\theta))^{\beta'+2}}\right)\frac{\partial D^k(R,\theta)}{\partial R} \\
&+ 4\varepsilon''\left(-\frac{\alpha' A'}{(D^k(R,\theta))^{\alpha'+1}} + \frac{\beta' B'}{(D^k(R,\theta))^{\beta'+1}}\right)\frac{\partial^2 D^k(R,\theta)}{\partial R^2} \\
\frac{\partial^2 V^k(R,\theta)}{\partial^2 \theta} &= 4\varepsilon''\left(\frac{\alpha'(\alpha'+1)A'}{(D^k(R,\theta))^{\alpha'+2}} - \frac{\beta'(\beta'+1)B'}{(D^k(R,\theta))^{\beta'+2}}\right)\frac{\partial D^k(R,\theta)}{\partial \theta} \\
&+ 4\varepsilon''\left(-\frac{\alpha' A'}{(D^k(R,\theta))^{\alpha'+1}} + \frac{\beta' B'}{(D^k(R,\theta))^{\beta'+1}}\right)\frac{\partial^2 D^k(R,\theta)}{\partial \theta^2}
\end{aligned}
\tag{B.4}
$$

$$
\begin{aligned}
D^k(R,\theta) &= \frac{R}{R_{CNT}\Theta^k(\theta)} - 2 \\
\frac{\partial D^k(R,\theta)}{\partial R} &= \frac{1}{R_{CNT}\Theta^k(\theta)} \\
\frac{\partial D^k(R,\theta)}{\partial \theta} &= -\frac{R}{R_{CNT}\Theta^k(\theta)^2}\frac{d^2\Theta^k(\theta)'}{d\theta^2} \\
\frac{\partial^2 D^k(R,\theta)}{\partial R^2} &= 0 \\
\frac{\partial^2 D^k(R,\theta)}{\partial \theta^2} &= -\frac{R}{R_{CNT}\Theta^k(\theta)^2}\frac{\partial^2\Theta^k(\theta)}{\partial^2\theta} + \frac{2R}{R_{CNT}\Theta^k(\theta)^3}\left(\frac{\partial\Theta^k(\theta)'_\theta}{\partial\theta}\right)^2
\end{aligned}
\tag{B.5}
$$

$$\Theta^k(\theta) = 1 + \sum_{i=1}^{k} C_i((-1)^{i-1} + \cos(2i\theta))$$
$$\frac{d\Theta^k(\theta)}{d\theta} = -\sum_{i=1}^{k} 2iC_i \sin(2i\theta) \quad \text{(B.6)}$$
$$\frac{d^2\Theta^k(\theta)}{d\theta^2} = -\sum_{i=1}^{k} 4i^2 C_i \cos(2i\theta)$$

$$\Gamma(R,\gamma) = 1 + W_\gamma(R)(1-\cos(2\gamma))$$
$$\frac{\partial\Gamma(R,\gamma)}{\partial\gamma} = 2W_\gamma(R)\sin(2\gamma)$$
$$\frac{\partial^2\Gamma(R,\gamma)}{\partial\gamma^2} = 4W_\gamma(R)\cos(2\gamma) \quad \text{(B.7)}$$
$$\frac{\partial\Gamma(R,\gamma)}{\partial R} = \frac{dW_\gamma(R)}{dR}(1-\cos(2\gamma))$$
$$\frac{\partial^2\Gamma(R,\gamma)}{\partial^2 R} = \frac{d^2W_\gamma(R)}{dR^2}(1-\cos(2\gamma))$$

$$W_\gamma(R) = C_\gamma(R/R_{CNT})^\delta$$
$$\frac{dW_\gamma(R)}{dR} = \frac{\delta C_\gamma}{R_{CNT}}(R/R_{CNT})^{\delta-1} \quad \text{(B.8)}$$
$$\frac{d^2W_\gamma(R)}{dR^2} = \frac{\delta(\delta-1)C_\gamma}{R_{CNT}^{\ 2}}(R/R_{CNT})^{\delta-1}$$

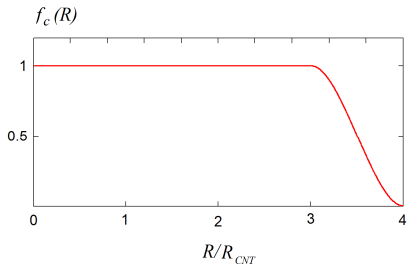


Fig. 35. Cutoff function $f_c(\mathrm{R})$.

The coefficients of smooth cutoff function $f_c(\mathrm{R})$ (Fig. 35), given in Table 3, are found from:

$$\begin{pmatrix} Q_0 \\ Q_1 \\ Q_2 \\ Q_3 \end{pmatrix} = \begin{pmatrix} 1 & R_{beg} & R_{beg}^{\ 2} & R_{beg}^{\ 3} \\ 1 & R_{end} & R_{end}^{\ 2} & R_{end}^{\ 3} \\ 0 & 1 & 2R_{beg} & 3R_{beg}^{\ 2} \\ 0 & 1 & 2R_{end} & 3R_{end}^{\ 2} \end{pmatrix} \begin{pmatrix} f_c(R_{beg}) \\ f_c(R_{end}) \\ \left.\dfrac{df_c(R)}{dR}\right|_{R_{beg}} \\ \left.\dfrac{df_c(R)}{dR}\right|_{R_{end}} \end{pmatrix} \tag{B.9}$$

with parameters $R_{beg}$ =0.75, $R_{end}$ =1.